

UC Berkeley

UC Berkeley Electronic Theses and Dissertations

Title

Siderophore-mediated Competition for Iron Between Humans and Pathogenic Bacteria

Permalink

<https://escholarship.org/uc/item/2mt6d2zq>

Author

Sia, Allyson Kawile

Publication Date

2013

Peer reviewed|Thesis/dissertation

Siderophore-mediated Competition for Iron Between Humans and Pathogenic Bacteria

By

Allyson Kawile Sia

A dissertation submitted in partial satisfaction of the

requirements for the degree of

Doctor of Philosophy

in

Chemistry

in the

GRADUATE DIVISION

of the

UNIVERSITY OF CALIFORNIA, BERKELEY

Committee in charge:

Professor Kenneth N. Raymond, Chair

Professor Chris Chang

Professor Richard Calendar

Fall 2013

Siderophore-mediated Competition for Iron Between Humans and Pathogenic Bacteria

Copyright © 2013

Allyson Kawile Sia

Abstract

Siderophore-mediated Competition for Iron Between Humans and Pathogenic Bacteria

by

Allyson Kawile Sia

Doctor of Philosophy in Chemistry

University of California, Berkeley

Professor Kenneth N. Raymond, Chair

Iron is the most abundant and essential transition metal used by many living organisms. To understand the means by which organisms acquire, transport and use iron expands the understanding we humans have of life. Organisms evolved multiple strategies to solubilize iron hydroxides from the environment and to increase iron bioavailability. Most bacteria, fungi and plants solubilize iron from the environment by synthesis and secretion of siderophores, or small molecules that have a high affinity for ferric iron. Alternative iron acquisition strategies are often employed simultaneously which include piracy of iron stores from other organisms and exploitative uptake of nonnative siderophores and hemes.

Generally this work is meant to provide detailed information for mechanisms and strategies involved in iron competition between pathogenic bacteria and human hosts. Detailed structural and kinetic investigations of iron acquisition pathways in the *Bacillus cereus* group of bacteria are discussed in Chapters 1-4. The *B. cereus* group of bacteria includes threatening pathogens such as the anthrax pathogen (*B. anthracis*) and enterotoxigenic bacteria (*B. cereus*). Iron complexes of molecules as small as citrate and as large as a polymeric bacterial capsule are probed for structural and kinetic data related to iron acquisition and transport. Studies of the iron binding ability and subsequent transport of synthetic analogs of the *B. anthracis* stealth siderophore petrobactin are also included. Taken together, these studies shed light on multiple mechanisms and structure-function relationships necessary for the pathogenic bacteria to obtain an adequate iron supply and regulate virulence.

Bacillus bacteria can infect humans and compete with the host iron supply. The consequences of iron piracy by *Bacillus anthracis* are especially likely to be fatal. Crucial to the human defense against bacterial infections is the immune protein siderocalin. Siderocalin is antibacterial and limits bacterial growth by intercepting bacterial siderophores. Chapter 5 highlights siderocalin and its recently established alternative role as an iron transport protein. For siderocalin to transport iron, an endogenous siderophore

equivalent is required. A putative endogenous, or 'mammalian' siderophore, is evaluated by solution thermodynamic analyses, inorganic spectroscopy and biochemical assays. The multipurpose role of siderocalin could have important clinical impact, and it is important that the foundation of these studies are clear and consistent at the chemical level. The elucidated roles of siderocalin in humans convey key iron-restricting strategies by humans to compete with invading pathogens for iron. The collection of chapters in this work portrays the competition for iron as dynamic, aggressive and evolving by both humans and invading bacterial pathogens and is meant to provide a snapshot of the competition in current times.

Table of Contents

Chapter 1: The Significance of Iron to Life, from Humans to Bacteria

The presence of iron on earth.....	1
Chemistry of iron, chemistry of life.....	2
Iron transport and storage in humans.....	8
Iron and bacterial virulence.....	10
The arms race for iron is a dynamic competition	11
Microbial iron acquisition by <i>B. cereus</i> group of bacteria.....	16
Siderocalin-mediated mammalian iron transport.....	19
Conclusions.....	19
References.....	14-21

Chapter 2: Petrobactin-mediated Iron Uptake in B. cereus Group of Bacteria

Introduction.....	22
Results.....	24-31
Synthesis of petrobactin models.....	24
Sulfonation of 3,4-catechols.....	25
Binding and growth studies with YclQ of <i>B. subtilis</i>	25
Binding and growth studies with FatB of <i>B. cereus</i>	29
Discussion.....	31-34
Sulfonation of 3,4-catechols by concentrated sulfuric acid.....	31
Selectivity of YclQ, the PB-binding protein of <i>B. subtilis</i>	32
Selectivity of FatB, the PB-binding protein of <i>B. cereus</i>	34
Conclusions.....	34
Experimental.....	35-40
References.....	41-43
Chapter 2 Appendix.....	44

Chapter 3: Solution Thermodynamics, Structure and Transport of a Ferric Citrate Trimer in Bacillus cereus

Introduction.....	45
Results.....	47-50
Speciation diagrams of ferric citrate.....	47
K_d actual and upper limit calculations for FctC:Fe ₃ cit ₃ interaction.....	53
A molecular scheme of Fe ₃ cit ₃	53
Discussion.....	51-54
Fe ₃ cit ₃ is selected for by FctC.....	51
K_d for FctC:Fe ₃ cit ₃ is the lowest reported for all known siderophore-binding protein systems...52	
The molecular scheme for Fe ₃ cit ₃ involves direct coordination by protein residues.....	52
Comparing Fe ₃ cit ₃ with an aluminum citrate trimer.....	53
Conclusions.....	54
Experimental.....	55-56
References.....	57-58
Chapter 3 Appendix.....	59-60

Chapter 4: Structure and Function of Poly- γ -(D)-glutamic Acid Capsule, a B. anthracis Virulence Factor and Potential Siderophore

Introduction.....	61
Results.....	63-78
PA-siderophore interactions.....	63
Structural investigations of Fe-PGA.....	64
Kinetic ability of PGA to remove iron from human transferrin.....	71
Discussion.....	78-80
PA has no measurable affinity for bacterial siderophores.....	79
EXAFS studies reveal iron conglomerates within PGA polymer.....	79
PGA polymers remove iron from human transferrin as fast as natural siderophores.....	79
Experimental.....	81-82
References.....	83-85
Chapter 4 Appendix.....	86

Chapter 5: Siderocalin-mediated Iron Transport through use of Mammalian Siderophores

Introduction.....	87
Results.....	88-95
Investigation of Fe-GA complexes.....	88
Synthesis of a hexadentate iron chelator based on GA.....	94
Discussion.....	95-99
Solution thermodynamics analyses show that GA does not bind iron.....	95
Siderocalin fluorescence is not quenched by salicylate siderophores.....	96
Purported siderocalin-iron-salicylate complexes do not induce apoptosis.....	98
Conclusions.....	99-100
Experimental.....	100-104
References.....	105-106

To my family, friends, and science fans everywhere.

List of Figures

Chapter 1: The Significance of Iron to Life, from Humans to Bacteria

Figure 1.1. Examples of iron catalysis.....	2
Figure 1.2. Iron active sites found in nature's proteins.....	3
Figure 1.3. Endonuclease III of <i>E. coli</i> binding double-stranded DNA.....	5
Figure 1.4. Typical iron-binding moieties of siderophores.....	7
Figure 1.5. Siderophores from bacterial pathogens.....	8
Figure 1.6. Siderocalin ribbon structure and space-filling diagram.....	9
Figure 1.7. Iron transport in Gram-positive and Gram-negative bacteria.....	11

Chapter 2: Petrobactin-mediated Iron Uptake in B. cereus Group of Bacteria

Figure 2.1. Siderophores of <i>Bacillus</i> bacteria.....	22
Figure 2.2. Ribbon structure and space-filling structure for YclQ	23
Figure 2.3. Depiction and explanation of protein-ligand dissociation constant, K_d	26
Figure 2.4. YclQ fluorescence binding assay results	26
Figure 2.5. Disc-diffusion assay results for <i>B. subtilis</i>	28
Figure 2.6. OD ₆₀₀ growth assays for <i>B. subtilis</i>	29
Figure 2.7. FatB fluorescence binding assay results.....	30
Figure 2.8 OD ₆₀₀ growth assays for <i>B. cereus</i>	31

Chapter 3: Solution Thermodynamics, Structure and Transport of a Ferric Citrate Trimer in Bacillus cereus

Figure 3.1. Ribbon diagram of FecA and bound Fe ₂ cit ₂	45
Figure 3.2. Fluorescence quenching assay of FctC.....	46
Figure 3.3. Nano-ESI MS results for FctC with iron citrate solutions.....	46
Figure 3.4. Various iron citrate species in aqueous solution.....	47
Figure 3.5. Ferric citrate speciation diagrams for Fe: cit = 1:50 and 1:100.....	48
Figure 3.6. Ferric citrate speciation diagrams for Fe: cit = 1:1 and 1:10.....	49
Figure 3.7. Fluorescence quenching assay results and speciation for FctC and Fe: cit 1:50.....	49
Figure 3.8 Molecular models of Fe ₃ cit ₃ H ₂ O.....	51
Figure 3.9 Comparison of Fe ₃ cit ₃ L ₃ and Al ₃ cit ₃ OH(H ₂ O) structures.....	53
Figure 3.10 Speciation diagrams of aluminum citrate for Al: cit = 1:1 and 1:10.....	54

Chapter 4: Structure and Function of Poly-γ-(D)-glutamic Acid Capsule, a B. anthracis Virulence Factor and Potential Siderophore

Figure 4.1. Anthrax toxin assembly.....	61
Figure 4.2. Bond-line drawings of polyglutamic acid polymers.....	62
Figure 4.3. Fluorescence quenching assay of PA with siderophores.....	63
Figure 4.4. Pre-edge XANES data for PGA samples.....	65
Figure 4.5. EXAFS of native LDPGA from <i>B. licheniformis</i>	67
Figure 4.6. EXAFS of native DPGA from <i>B. licheniformis</i>	68
Figure 4.7. EXAFS of iron-supplemented DPGA from <i>B. licheniformis</i>	69
Figure 4.8 EXAFS of Fe-free DPGA from <i>B. licheniformis</i>	70
Figure 4.9 Background UV-vis spectra for Fe ₂ Tf-PGA iron transfer experiments.....	71

Figure 4.10 UV-vis spectra and analysis of iron binding by DPGA	74
Figure 4.11 Saturation kinetics plot for DPGA based on UV-vis experiments.....	75
Figure 4.12 UV-vis spectra and analysis of iron binding by LDPGA.....	76
Figure 4.13 Saturation kinetics plot for LDPGA based on UV-vis experiments.....	77
Figure 4.14 Fluorescence spectra and analysis of iron binding by DPGA.....	77
Figure 4.15 Fluorescence spectra and analysis of iron binding by LDPGA.....	78

Chapter 5: Siderocalin-mediated Iron Transport through use of Mammalian Siderophores

Figure 5.1. Mammalian siderophore candidates.....	87
Figure 5.2. Speciation diagram for Fe(GA).....	90
Figure 5.3. Speciation diagrams for Fe(23DHB0 and Fe(SA) and solution equilibria.....	91
Figure 5.4. UV-vis spectra for Fe(GA) and Scn:Fe(GA).....	92
Figure 5.5. Siderocalin fluorescence binding assays with iron bidentate ligand complexes.....	92
Figure 5.6. Siderocalin fluorescence binding assays with TRENGEN.....	95
Figure 5.7. Crystallographic modeling of siderocalin calyx with iron complexes.....	95
Figure 5.8 Crystallographic modeling of Fe(GA) with siderocalin binding pocket 1.....	96
Figure 5.9 Scn emissions versus volumes of iron-siderophores added.....	97
Figure 5.10 Results showing Scn and salicylate siderophores do not induce apoptosis.....	99

Appendix figures

Figure A2.1 Solutions of Fe(34DHB) ₂ and Fe(34DHBS) ₂	44
Figure A2.2 UV-visible spectra of Fe(34DHB) ₂ and Fe(34DHBS) ₂	44
Figure A3.1 Iron-citrate speciation using only M ₂ L ₂ multimer formation constant.....	59
Figure A3.2 Iron-citrate speciation using only M ₃ L ₃ multimer formation constant.....	59
Figure A4.1 Background fluorescence spectrum of DPGA.....	86
Figure A4.2 Background fluorescence emissions from Fe ₂ Tf.....	86
Figure A4.3 Background fluorescence spectrum of LDPGA.....	86

List of Schemes

Scheme 1.1. Intestinal Iron Absorption in Humans.....	6
Scheme 2.1 Synthesis of 34thiaz.....	24
Scheme 2.2 Conversion of 34thiaz to petrobactin mimics.....	25
Scheme 2.3 Sulfonation of 34catechol derivatives.....	25
Scheme 2.4 Depiction of iron-PB mimic compound shape versus Fe-PB.....	33
Scheme 5.1 Catecholate to salicylate iron coordination modes.....	88
Scheme 5.2 Synthesis of TRENGEN, a hexadentate GA-based iron chelator.....	94
Scheme 5.3 Iron complex diameters in a schematic siderocalin binding calyx.....	98

List of Tables

Table 2.1 Dissociation constants for various ligands with YclQ.....	27
Table 2.2 Dissociation constants for various ligands with FatB.....	30
Table A3.1 Calculated bond distances and angles for Fe ₃ cit ₃ L ₃	60
Table 4.1 Key atom-atom distances for Fe-PGA systems determined by EXAFS.....	71
Table 4.2 Ligand saturation rate constants for various iron chelators.....	72
Table 4.3 Experimentally determined rate constants for iron acquisition by PGA.....	80
Table 5.1 Relevant solution equilibria for Fe-GA complexation.....	89
Table 5.2 Proposed binding mechanisms of Fe-siderophore complexes to Scn.....	97

List of Symbols and Abbreviations

OD ₆₀₀	optical density measured at 600 nm
K_d	protein-ligand dissociation constant
PA	anthrax protective antigen
PGA	poly- γ -glutamic acid capsule, also referred to as PGA polymer
DPGA	poly- γ -(D)-glutamic acid, where D refers to the optical activity at the chiral center
LDPGA	poly- γ -(L/D)-glutamic acid, where the optical activity at the chiral center is both L and D due to both R and S stereoisomers present in the polymer
Tf-Fe ₂	diferric human transferrin
k_{obs}	observed rate constant
Scn	siderocalin, an antibacterial human immune protein also known as uterocalin, NGAL, Lcn2 and HNL
K_{MLH}	stepwise association constants for given equilibria of M metals, L ligands, H protons
B_{MLH}	cumulative association constants for given equilibria of M metals, L ligands, H protons
GA	gentisic acid, also known as 2,5-dihydroxybenzoic acid (25DHB)
23DHB	2,3-dihydroxybenzoic acid
34DHB	3,4-dihydroxybenzoic acid
SA	salicylic acid
TRENGEN	synthetic hexadentate ligand based on three GA binding units

List of Equations

Eq. 4.1 Stepwise removal of iron from diferric human transferrin.....	72
Eq. 4.2 Rate constant expression for pseudo-first order reactions.....	72
Eq. 4.3 Expression for pseudo-first order saturation kinetics.....	72
Eq. 5.1 Generic equilibrium for metal complex formation.....	90
Eq 5.2 Cumulative equilibrium constant for generic metal complex formation.....	90

Acknowledgments

My chemistry career started rather late, but I am happy it developed late than never. I am forever indebted to Professor Alan F. Heyduk for teaching chemistry in an inspiring way and for introducing me to the world of chemistry research. Prof. Heyduk generously welcomed me to his research group where his group developed redox-active ligands for use in early transition metal catalysis. It was there that I observed the potentially volatile yet promising life of graduate school and also how possible it was to pursue the fascinating world of cutting edge research with my own two hands. Dr. Mason Haneline was also a strong influence in my chemistry career and I owe a great many thanks to him for expanding my knowledge both in chemistry and in music. I want to thank the UCI chemistry professors who have been influential to me for their passion for chemistry combined with their admirable personalities: Prof. Gregory Weiss and Prof. Andy Borovik. They are fan favorites amongst many students, scientists, and colleagues and I am honored and lucky to have learned directly from them.

I took my inorganic chemistry background from Prof. Heyduk's lab and wanted to apply it to the daunting world of biology. I joined Prof. Kenneth N. Raymond's lab at Cal where I studied the transport of iron between pathogenic bacteria and humans through use of siderophores and also through the human immune protein siderocalin. Fruitful results with collaborators Dr. Collin Correnti and Dr. Roland Strong at the Fred Hutchinson Cancer Research Center in Seattle, WA resulted from their dedicated teamwork, which has been enjoyable over the years. I owe a special thanks to the iron group members Ben, Tatsuya, Anna and Trisha, who have been my colleagues, mentors, teachers, friends, and lab family in 511 Latimer. Ben has been my teammate through all of graduate school and I couldn't have asked for a better person to experience graduate school with. Both Ben and Tatsuya have been a great source of conversation and enlightenment in topics ranging from soccer and babies to metal lability and bacterial growth curves. Thank you both for your companionship and for teaching me new things. I also want to thank the other group members, past and present, for making lab life fun and enjoyable. I give my best to Billy, Tiffany, Tatum and Jenna, that the remainder of their graduate careers be filled with joys and success.

Some special projects I pursued at Cal were possible with intellectuals like Dr. Alexander Kintzer and Prof. Bryan Krantz, who introduced perplexing problems about anthrax toxin virulence to inorganic chemists. Dr. David Shuh organized a wonderful collaboration with Dr. Tsuyoshi Yaita and his team at the Japan Atomic Energy Agency. I owe many thanks to both David and Tsuyoshi for the fantastic experience I had in Japan working with EXAFS experts and beamline scientists at the SPring8 lab in Japan. Together we arrived one step closer to understanding how an iron-capsule modulates anthrax pathogenicity. I was also very lucky to learn some computational chemistry from Dr. Kathy Durkin, one of the top scientists in her field. Kathy demonstrated that one could be both a top level scientist and avid baseball fan at the same time (go SF Giants!).

Closing this chapter in my life would be impossible without the support of my friends. Firstly, to my friends Lam and Olivia who stuck with me the whole way despite the time and distance that separated us. There are some wonderful friends I've made in my years at Berkeley who know the true, multifaceted me: Miriam, Kiki, Mike, Margarita, John, Joe, Ga-Lai, Pete. Friends like you constantly reminded me how to value life outside of work while still pursuing

greatness. This was probably most important skill for me to learn at this time in my life. I also want to thank my friends who have known me since childhood and who have given me a social outlet and support: Van, Dan, Andrea, Kavi who grew up near me, and my cousins who had some idea of what I was doing in Berkeley, Mae, Jomar, Alvin, Roma.

There are a few people whose optimistic dispositions in life and love have inspired me to lead my life beyond graduate school in the same way. Coach Holloway, I am glad fate introduced us through Rancho basketball even though (admittedly) I learned more from you about family, life and love than basketball. You, Amy, Chey and Brenna all have a special place in my heart. Greta and Ray, you have both redefined the meanings of generosity, kindness and selflessness in my book. I am happy to have you both in my life.

Tyler Brooks has been a source of endless support, and the last few years of graduate school have been easier with him to love and support me (and vice versa, of course). His cat Yadi doesn't do too bad a job of this either. In many ways, these two make up my better half and have helped me finish strong.

I want to especially thank my own family for sticking with me and always reminding me of where I came from. Jaimee, thank you for talking me out of dumb ideas and encouraging me to pursue the great ones. Charlotte, Mom and Dad, thank you for your endless pride in me, especially when I do not always have pride in myself. I know that if I wanted to do anything you would support me, and for that I am truly grateful.

Success in Ken's lab would have been very difficult without the help of Dr. Jide Xu and Susan Meux. Xu, thank you for your help in the laboratory and also for sharing amazing stories with me. Susan, thank you for all that you do. Our manuscripts would never become published papers without you, nor would our lab be able to function smoothly without you.

Professor Ken Raymond, I give my endless thanks for the many opportunities to learn and grow in graduate school. Thank you for your advice and guidance, and for giving me the freedom to pursue projects I was interested in. Thank you for the opportunities to collaborate with experts around the globe and for the once in a lifetime opportunity to travel to communicate these results to the scientific community. I consider myself very lucky to have had you as a mentor. I thank you for your confidence in me and for conditioning me to become a Cal-quality scientist.

Chapter 1

The Significance of Iron to Life, from Humans to Bacteria

The presence of iron on earth

Over 13 billion years ago the Big Bang initiated the expansion of the universe and the generation of various subatomic particles. Thousands of years would pass before light elements such as helium and hydrogen came into existence. Eventually, nucleosynthetic fusion of light elements to form heavier ones in dying stars ultimately generated the elements such as carbon, oxygen, and eventually, one of the most important heavier elements, iron. To this day, some of the iron that was created from stardust many billion years ago is present in the earth, making up 80% of the core and 6.3% of the crust (1). In fact, iron constitutes about 32% of the Earth by weight (2).

Iron is commonly found in the Earth's crust as an oxide or carbonate compound, such as hematite (Fe_2O_3), magnetite (Fe_3O_4), limonite ($2\text{Fe}_2\text{O}_3$ trihydrate) or siderite (FeCO_3), to list a few (3). The Earth's magnetic field is generated by flowing molten iron and other metals in the Earth's core. Magnetite is a peculiar compound, found in the beaks of homing pigeons and within bacteria as a tool used to navigate the Earth (4–6). Magnetite is ferromagnetic and aligns itself with the magnetic field of the Earth, giving organisms an internal global positioning system. The ability of organisms to sense the Earth's magnetic field via internalized iron compounds may be even more widespread, as suggested by navigation studies in various marine inhabitants such as salmon, spiny lobsters, sea slugs and sea turtles (7–9).

The abundance of iron on and within the Earth is likely one reason for its extensive use by terrestrial organisms. At the macroscopic level, humans have used iron for tools, weapons and other materials. Such exploitation of iron emerged during the so-called Iron Ages (c. 1200 BC-500AD) across various geographical regions (10, 11). More importantly, the microscopic use of iron in biochemical processes within living systems had been in tact several thousands of centuries before, at the very beginning of life on Earth. Much of these same iron-dependent biochemical processes are present in living organisms today and are a result of iterative optimizations by evolution.

Iron in oceanic waters is important for global nutrient cycling as well as supporting marine life. The concentrations of iron are quite low in oxic ocean environments and vary depending on depth and geographical location (12). The bioavailability of iron in the ocean is much lower than on land. Nevertheless, marine organisms at the very bottom of the food chain, phytoplankton, depend on iron for survival and growth. Many marine inhabitants that depend on iron for survival have developed clever mechanisms to solubilize and obtain iron, thus demonstrating the sheer importance of the trace element.

Iron can access eight different oxidation states (Fe^{2-} to Fe^{6+}) that allow it to have vastly different properties and chemistry. Ferrate ions such as $[\text{Fe}^{\text{VI}}\text{O}_4]^{2-}$ are especially powerful oxidants used in applications such as batteries, soil and wastewater treatment and disinfectants (13–16). In these processes, Fe^{6+} is reduced to colloidal, nontoxic Fe^{3+} products.

Iron chemistry can be exploited for homogeneous catalysis, contrary to what was thought more than two decades ago. Typically, synthetic iron catalysts face severe limitations based on the fact that only one-electron redox chemistry is accessible at the iron center. Catalysts with precious metal centers such as platinum, palladium and rhodium can perform two electron redox reactions and thus have more predictable reactivities and stable intermediates (17–19). However, studies of iron catalysts with redox-active, noninnocent ligands have suggested that precious metal chemistry is

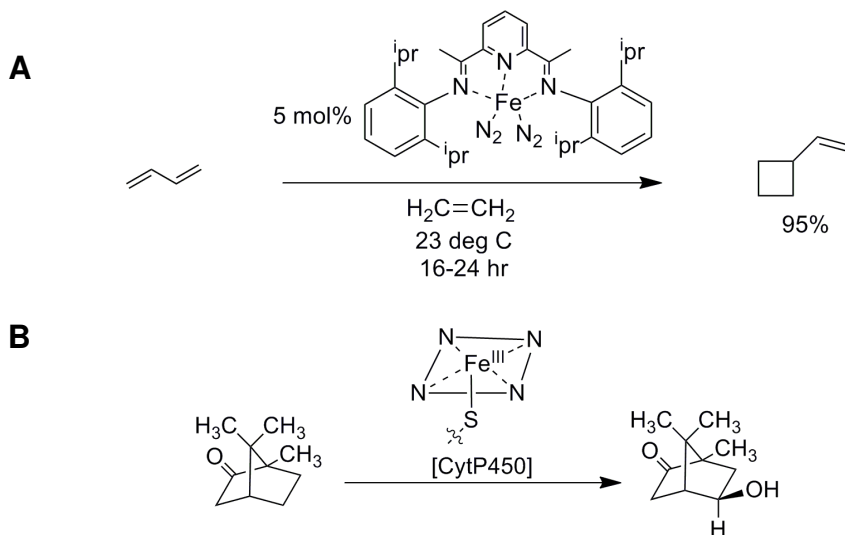


Figure 1.1. Examples of iron catalysis. Net chemical transformations attainable with synthetic iron catalysts (A) (11-14) and Nature's catalysts (B). Cytochrome P450 is abbreviated CytP450 and the porphyrin structure is symbolized by a four iron-chelating nitrogen donors.

attainable with a non-precious metal such as iron (20). Iron as an alternative metal for catalysis may be more cost-effective and readily available due to its abundance on earth. No longer confined to its roles as a Lewis acid or stoichiometric reagent, iron catalysts can be used to activate C-H bonds with concomitant C-C bond formation, in intermolecular [2+2] cycloadditions or enyne cyclizations, all chemistry previously thought inaccessible by iron compounds (Figure 1.1) (21–23).

In Nature, iron chemistry often occurs with iron in the +2 to +5 oxidation states where iron partakes in reduction-oxidation reactions vital to detoxification, metabolism, gene expression, and DNA replication in living systems (24–27). Under aerobic, aqueous conditions, iron often exists as rust, or other highly insoluble Fe(III) oxides. The first pK_a of Fe^{III}(H₂O)₆ is about 3, which favors the stepwise hydrolysis of hexaaquo iron to iron hydroxo species (28). Furthermore, the solubility of such Fe(III) species in water at neutral pH is quite low (about 10⁻³⁸) (28). Nevertheless, organisms have evolved several strategies to combat the insolubility of iron. The use of iron by living organisms will be a central theme to this manuscript.

The chemistry that iron performs within living systems is heavily dependent on the ligand environment and both first and secondary coordination spheres. Iron atoms chelated by macrocyclic chelates such as porphyrins or hemes are found within many of

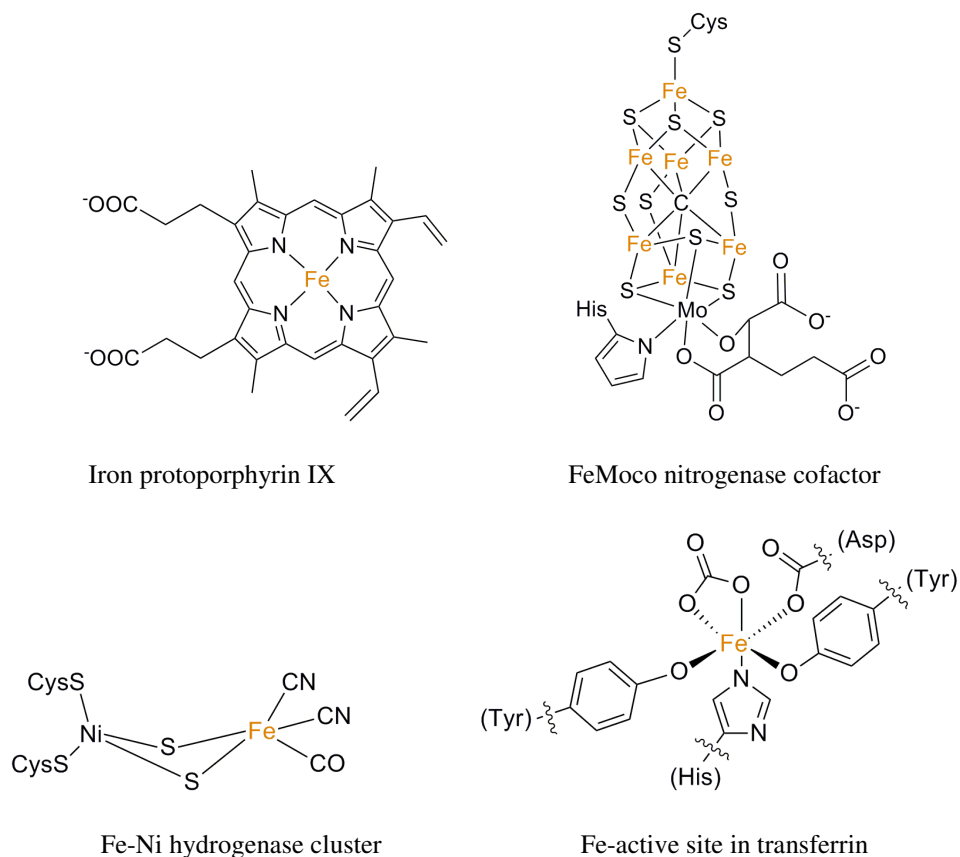


Figure 1.2. Iron active sites found in Nature’s proteins. Examples of iron-containing protein active sites found in living systems: Iron protoporphyrin IX (top left) is the active site in hemoglobin, FeMoco is the cofactor for nitrogen-fixing enzymes in living systems (top right). The Fe-Ni cluster (bottom left) is found in hydrogenase enzymes, and transferrin (bottom right) has an active site in which iron is bound by protein residues and a carbonate ion.

Nature's proteins. Hemoglobin is an example of an iron-heme containing protein and is widely known as the oxygen carrying protein in humans. The active site is specifically called iron protoporphyrin IX (Figure 1.2). Iron protoporphyrin IX in the resting state contains Fe^{2+} , which binds small molecules such as dioxygen. Oxygen binding results in an oxidation of iron to Fe^{3+} which has a smaller ionic radius than Fe^{2+} allowing the metal to achieve coplanarity with the heme. The porphyrin substituents, axial ligands and overall protein structure fine tune the reduction potential at the iron center to make it ideal for small molecule transport (O_2 , CO).

In general, the porphyrin has a highly delocalized electronic structure that allows compatible metals such as iron the ability to delocalize both spin and electrons into the ring (29, 30). A result is that, depending on the axial ligands and porphyrin substituents, iron can access more than one oxidations state and perform different functions. While the iron-heme unit in hemoglobin serves the purpose of small molecule delivery, another iron-heme in cytochrome P450s performs much different chemistry.

The cytochrome enzymes are some of Nature's versatile iron catalysts. Bacteria, plants and mammals possess cytochromes that are potent oxidants in solubilization and detoxification processes for example (31, 32). The cytochrome enzymes function at ambient pressure and temperatures in living systems, which is not so trivial for synthetic iron catalysts. In cytochrome P450, the active detoxification catalyst in humans, the axial ligand at the iron-heme centers are not histidines as in hemoglobin but are cysteine thiolates (26, 27, 33). While the iron center of cytochrome P450 is in the +3 oxidation state when at rest, it is believed that an oxoferryl (Fe^{4+}) π -cation radical complex is the active oxidizing compound. Such a compound is transient and has been a source of scientific dispute for several years. Extensive investigations toward the characterization of the actual oxidizing species have convinced most that the oxoferryl center with an extra oxidizing equivalent delocalized in the porphyrin is the active oxidizing agent (27, 33).

Even more interesting are catalytic iron centers of iron-sulfur clusters. These prosthetic groups are thought to have evolved from inorganic iron-sulfur clusters that were present in hydrothermal vents of ancient earth and to have been incorporated into the metabolism of primitive organisms (34). Increasing concentrations of oxygen on earth generated by photosynthetic organisms during and after the Great Oxidation eventually left these iron-sulfur clusters less protected and prone to oxidation, which likely explains why iron sulfur clusters of proteins today are buried deep in protein pockets (35, 36). An example of the complexity of these structures is the cofactor for nitrogen-fixing enzymes, known as FeMoco (Figure 1.2). The $[\text{7Fe:9S}]$ cluster is structurally interesting because it is tethered to a molybdenum center (37, 38). Several transition metals in a mixed-metal catalytic system can be synthetically difficult for scientists to mimic and mostly are left for Nature to synthesize and us to admire. Nitrogenase enzymes that contain FeMoco fix atmospheric dinitrogen into biologically useful ammonia under ambient conditions. The type of electron transport necessary for nitrogen fixation is facile in iron-sulfur clusters because of the electronic and magnetic properties of the iron-sulfur clusters. The smaller iron-sulfur cluster in hydrogenase enzymes can activate hydrogen, albeit sometimes with heterobinuclear active sites and unusual iron ligands (Figure 1.2) (39–41). Furthermore,

some iron sulfur clusters have functions other than redox chemistry involving electron shuttling such as enzyme stabilization (42), binding and activation of substrates (43, 44), and small molecule sensors (45–48). Endonuclease III is a DNA repair enzyme that is conserved from bacteria to humans. A [4Fe:4S] cluster stabilizes the structure of the endonuclease such that excision repair can occur when bound to DNA (Figure 1.3) (42).

A majority of living organisms depend on iron to carry out important biochemical processes that are required for life. However, too much iron present in living systems poses a direct threat to biomacromolecules it comes in contact with. Unregulated iron can catalyze Fenton chemistry and Haber-Weiss reactions, generating an excessive concentration of destructive free radicals harmful to the internal environment of an organism (49, 50). Thus organisms that rely on iron have evolved several regulatory mechanisms to keep iron either stored in proteins such as ferritins or immediately put to use.

Iron transport and storage in humans

Humans obtain most of their internal iron supply (3-5 grams on average) from dietary absorption, with about 1-2 mg of iron loss and intake occurring per day (51, 52). A generalized scheme of iron transport in the mammalian small intestine is depicted in Scheme 1. Several key proteins direct the heavily regulated process of dietary iron absorption. Dietary non-heme iron first comes into contact with divalent metal transporter 1 on the lumen side of enterocytes (53). Divalent metal transporter 1 is embedded in the intestinal brush border of duodenal enterocytes and is responsible for transporting ferrous iron from non-heme sources to the intracellular iron pool. A demand for iron results in the passage of iron through the basolateral membrane via a protein called ferroportin where the iron can be transferred into circulation via iron trafficking proteins such as transferrin (51, 54, 55). Transferrin residues and a carbonate ion are responsible for keeping iron in the protein active site (Figure 1.2) until the intended iron deposit site is met (56).

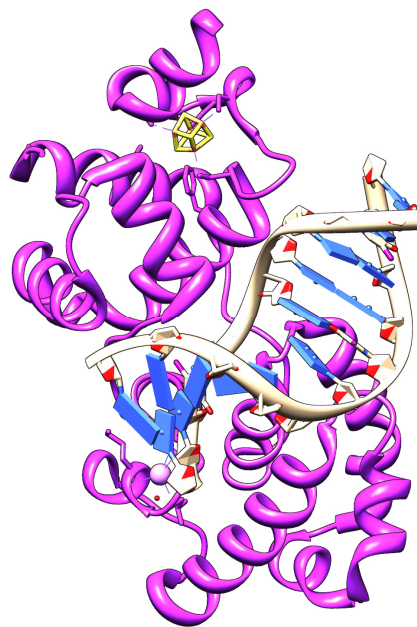
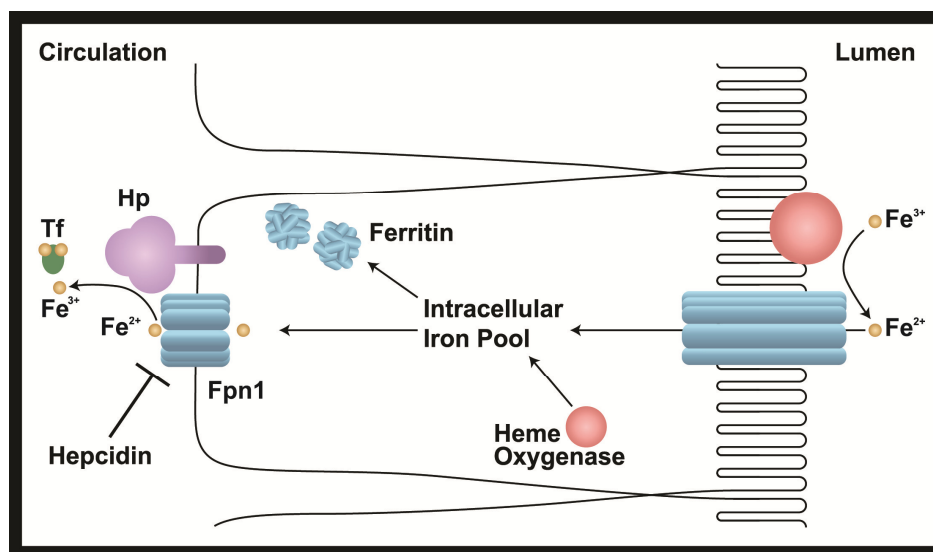


Figure 1.3. Endonuclease III (purple ribbon drawing) of *E. coli* binding double stranded DNA. A [4Fe:4S] cluster (yellow cube structure) stabilizes the structure and thus function of the endonuclease.



Scheme 1.1. Intestinal iron absorption in humans. Reduced iron from non-heme sources is imported by divalent metal transporter. Iron is either stored intracellularly in ferritins or proceeds to ferroportin 1 (Fpn1) which transports ferrous iron through enterocytes to circulation. Transferrin can pick up iron for delivery to other proteins. Hepcidin, a peptide hormone, and hephaestin, a ferrioxidase, have been shown to influence Fpn1 activity.

Small amounts of excess iron, up to a nontoxic concentration, are stored in intracellular ferritin in the form of ferrihydrite nanoparticles, which can also be thought of as mini aggregates of rust. Iron stored in ferritin can be mobilized via the unfolding of ferritin pores and concomitant reduction by reductants such as NADH, FMN or iron chelators once the demand for iron exceeds the supply in circulation (Scheme 1) (56, 57). Overstocked ferritins within the extracellular space, or an excess of intracellular iron, prompts the synthesis and release of the peptide hormone hepcidin, which can bind ferroportin and induce lysosomal degradation (51, 55). Together these proteins and the peptide hormone hepcidin and the ferrioxidase hephaestin work in concert to maintain the concentration of iron at life-sustaining, nontoxic levels (51, 54, 58). The system of iron proteins which control iron absorption and regulation of iron concentrations in circulation keep the concentrations of iron down to 10^{-24} M (56, 59), which is especially important for both controlling unwanted iron-induced free radical chemistry as well as suppressing iron available for invading microbes.

Iron and bacterial virulence

The link between excess iron and bacterial virulence is well established (60, 61). Individuals at risk for excessive internal iron overload, such as hemochromatosis or β -thalassemia patients and chronic alcoholics, are more susceptible to bacterial infections

that individuals with normal iron levels are able to ward off. For example, systemic infections and enterocolitis caused by *Yersenia enterocolitica* are enhanced in iron-overload patients but are commonly prevented in normal subjects (62). For medical conditions in which blood transfusions are required regularly, such as diabetes or sickle cell anemia bacteremia is increased (63–65) significantly and poses an additional complication to one's health.

In the course of evolution and coexistence with humans, mammals and other hosts, pathogenic bacteria have evolved multiple strategies to circumvent harsh environments low in

iron. Even in hosts and environments with non-excess amounts of iron, the element is still a scarce commodity due to low solubility of and consequently, low bioavailability of ferric ion. Thus conditions of excess

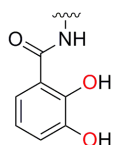


Figure 1.4. Typical iron-binding moieties built into siderophore scaffolds. From left to right: catechol, α -hydroxycarboxyl, and hydroxamic acid chelate units. Iron-binding atoms are shown in red, and hydroxyl groups are deprotonated before the chelate can bind iron.

iron facilitate and accelerate iron acquisition processes in microbes. Bacteria, fungi and plants all synthesize and secrete high affinity iron chelators called siderophores which sequester and solubilize ferric ion (56, 61, 66). Iron-siderophore complexes are then actively imported back to the organism. Siderophores can have up affinities for iron up to $K_f = 10^{49}$ (67, 68). While there are hundreds of siderophores known, all use some combination of catecholate, hydroxamate or α -hydroxycarboxylate chelating moieties tethered to a backbone scaffold (Figure 4). The chelates form 5- or 6-membered rings with iron, which are thermodynamically more stable than monodentate ligands. Furthermore, hard oxygen atoms have a high affinity for Fe^{3+} which is a hard acid. According to the Hard-Soft Acid-Base generalization by Pearson, atoms which have similar ionic radii and opposing charges will likely have optimal orbital overlap to form strong bonds (56, 69). Of course, while other factors contribute to the overall Gibbs free energy associated with a bonding event, Pearson's Hard-Soft Acid-Base concept is a good general model to follow for predicting affinities and describing siderophore oxygen affinities for ferric iron.

The arms race for iron is a dynamic competition

Pathogenic bacteria can synthesize multiple siderophores that have different iron affinities and chemical properties as a strategy to sequester iron under various environments. For example, strains of *Escherichia coli* synthesize both enterobactin and aerobactin. Enterobactin is a tris-catecholate siderophore tethered to a trilactone backbone ring and has the highest iron complex formation constant known (Figure 1.5). Aerobactin is a hybrid siderophore which binds iron with two hydroxamates and one α -

hydroxycarboxylate. The two siderophores have different lipophilicities and may be advantageous at different times in the initial stages of *E. coli* growth. Several siderophores may steal iron directly from host iron proteins (70–72).

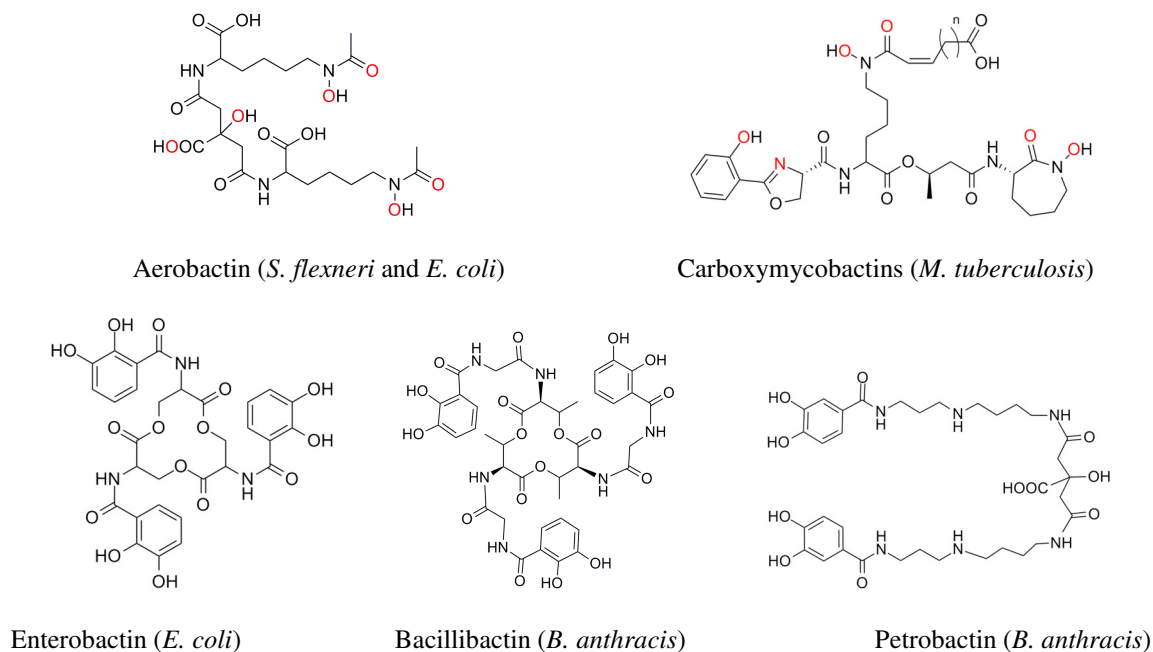


Figure 1.5. Examples of siderophores and respective bacterial pathogen in parentheses. Iron coordinating atoms are shown in red for the top two siderophores.

Beyond dependence on siderophores, pathogenic bacteria also employ alternative methods to circumvent host iron withholding. In the unique case of *Borrelia burgdorferi*, the causative agent of Lyme disease, metal dependent enzymes utilize manganese instead of iron, thus avoiding the energy expenditure needed to compete in the cutthroat competition for iron (73). Some bacteria express multiple iron-uptake proteins, including proteins that can bind exogenous siderophores that are nonnative to the bacterium. In more extreme cases, some bacteria such as *Neisseria* spp. and *Haemophilus influenzae*, do not synthesize siderophores but produce receptors for human iron-containing proteins such as transferrins (74–77).

Human hosts have developed multiple defense mechanisms to protect iron stores. Typically, an upregulation of ferritin storage and decrease in ‘free’ iron concentration is the initial response to bacterial stimuli. Bacterial sensing of iron-limited environment stimulates the biosynthesis and secretion of siderophores and upregulated expression of iron-related receptors such as hemophore receptors or iron channels (61, 72, 78). A direct

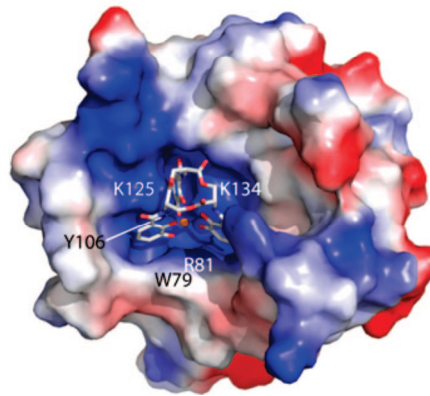
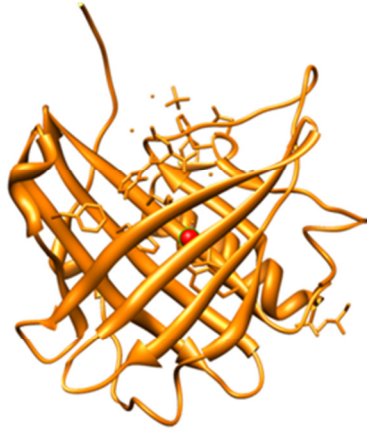


Figure 1.6. Siderocalin ribbon structure diagram (top), and space-filling diagram with ferric enterobactin ligand (bottom).

response to bacterial siderophores is the secretion of the immunoprotein Siderocalin in neutrophils. Found in the neutrophilic granules of white blood cells, Siderocalin is a type of lipocalin that has garnered interest for its specific role in binding and inactivating ferric enterobactin. For several decades Siderocalin was known but its function was not elucidated until 2002 when Goetz et al reported a crystal structure of Siderocalin with ferric enterobactin in the pocket (79).

Siderocalin binds triscatecholate siderophores such as bacillibactin and enterobactin within its trilobate calyx. The set of three binding pockets found within the calyx are lined with positive amino acid residues (Figure 1.6). The catecholate moieties of siderophores intercalate the positively charged, rigid pockets of the calyx (lined by residues Arg81, Lys125, Lys134) (80–82). A combination of cation-pi and electrostatic interactions are responsible for the binding affinity of Siderocalin for siderophores (83). Both apo-siderophores and ferric-siderophores are bound by Siderocalin, but iron alone is not, since the Coulombic forces are much too weak between ferric iron and the basic Siderocalin residues. The binding of siderophores by

Siderocalin has been shown to slow bacterial growth (79, 84–86).

It is believed that iron sequestered by Siderocalin is either recycled via hydrolysis of the siderophore or excreted as the ternary complex (78, 80). However, the fate of Siderocalin-mediated iron is still a matter of current discussion and research.

In the so called arms-race for iron, bacterial synthesis of multiple siderophores can be advantageous to many pathogenic bacteria. *Bacillus anthracis*, for example, the causative agent of anthrax, synthesizes both bacillibactin and petrobactin (Figure 1.5) at different stages of its life cycle (87, 88). Bacillibactin is similar to enterobactin from *Escherichia coli* in that both bind iron with three 2,3-catecholate moieties. While their

backbones are different in molecular composition, sterics and handedness, the binding affinities for iron are both quite high ($K_f = 10^{48}$ for bacillibactin). Petrobactin binds iron with a lower affinity (K_f estimated at 10^{23}) and uses two 3,4-catecholates and an α -hydroxycarboxylate unit to sequester iron (89).

Why do bacteria bother spending energy on synthesizing a weaker iron chelator under stress conditions when resources are already scarce? Studies by Abergel et al answered this conundrum in 2006 (88). Through protein fluorescence binding assays of Siderocalin with both petrobactin and bacillibactin as well as structural modeling, the authors were able to show that petrobactin is not bound by Siderocalin due to its 3,4-catecholate units which are incompatible with the rigid Scn pocket. Furthermore, these steric clashes with the calyx wall led the authors to term petrobactin a 'stealth-siderophore' since this siderophore passes under the radar of the Siderocalin, unbound and able to deliver iron back to the pathogenic bacterium, albeit with lower iron affinity. Furthermore, the biosynthesis and secretion of petrobactin and bacillibactin occur at different stages of infection perhaps to the advantage of the bacterium. Petrobactin is made several hours before bacillibactin. The difference in production is exacerbated at 37 degrees Celsius, suggesting different roles for petrobactin and bacillibactin in the anthrax infection cycle (90).

The arms race for iron was the inspiration for many studies in this manuscript, including fundamental studies of petrobactin-mediated iron uptake pathways and Siderocalin-mediated iron transport, topics which will be discussed in the next several paragraphs and chapters.

Microbial iron acquisition by B.cereus group of bacteria

Iron uptake in Gram-negative bacteria has been studied extensively, especially with *Escherichia coli* organisms that are relatively easy to study. The outer membrane of Gram-positive bacteria provides increased defense against host defense proteins, digestive enzymes and antibiotics. However, Gram-negative bacteria must still acquire nutrients through the outer membrane while discriminating against unwanted substances. To transport iron, a set of proteins are involved in the process to keep iron soluble and to ensure its delivery into the organism. Once a hemophore or siderophore delivers iron to the siderophore-binding proteins at the exterior of the outer cell membrane, iron exchange may occur in which the iron is actively transported across the outer membrane to a chaperone protein in the intermembrane space (91, 92) (Figure 1.7). The energy required for the transfer of a nutrient from the outer membrane into the cytoplasmic space is supplied by a collection of proteins belonging to the TonB system. The TonB proteins, energized by a protonmotive force across the cytoplasmic membrane, induce a conformational change in the outer membrane protein which results in the formation of a channel for nutrients (61, 93–95). Chaperone proteins then shuttle iron to proteins embedded in the inner membrane, where once again iron is actively transported and is available for intracellular delivery (61, 92).

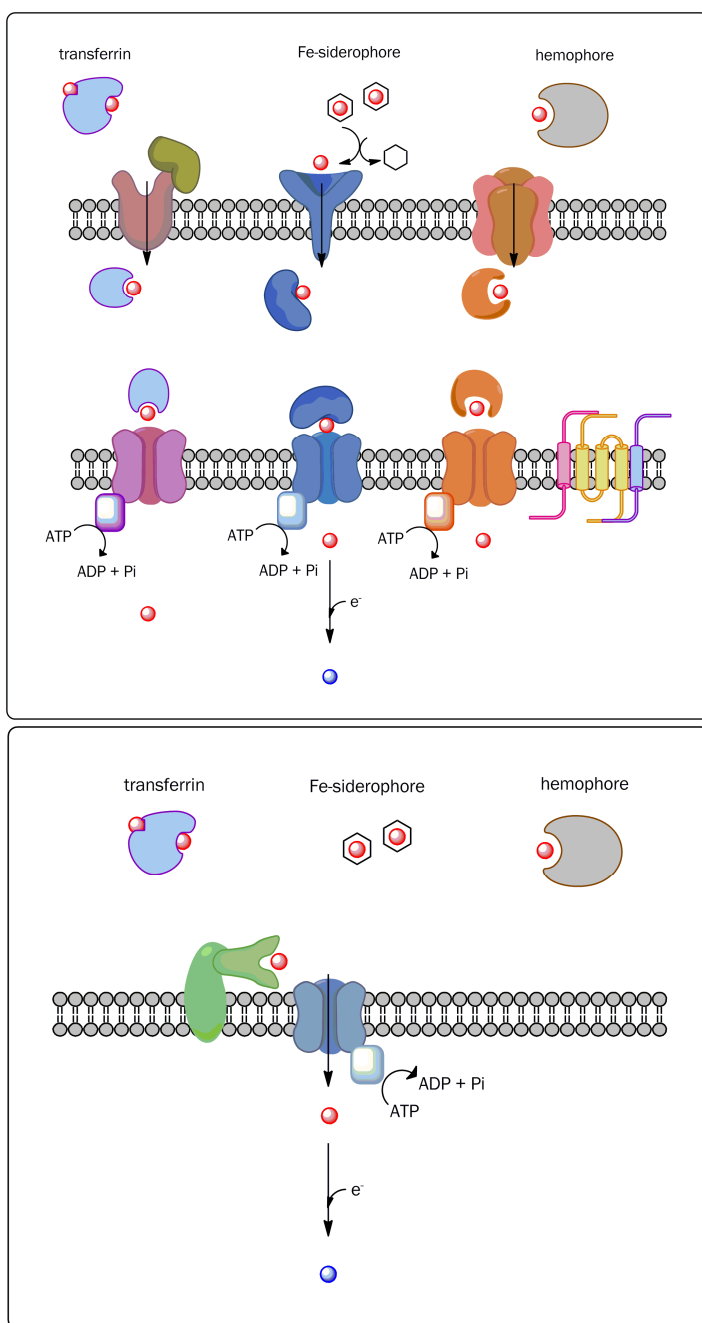


Figure 1.7. General scheme for iron transport in Gram-negative bacteria (top) and Gram-positive bacteria (bottom).

The first several chapters of this manuscript detail new information regarding iron transport in the *B. cereus* group of bacteria. In Chapter 2, petrobactin-mediated iron transport and the requirements for binding by the *B. cereus* and *B. anthracis* siderophore

Gram-positive iron transport is less understood, and fewer complete systems of iron transport are described in the literature. With only one cell membrane separating the internal environment of the bacterium and the extracellular environment, Gram-positive bacteria must express slightly different proteins that constitute its iron import systems. Siderophore-binding proteins are still present in Gram-positive organisms, tethered to the membrane and in close proximity to a membrane channel. Typically, recognition occurs at the siderophore-binding protein stage, where compatible siderophores and iron-siderophores are bound and then transferred to the inter-membrane channel, where iron is actively imported (Figure 1.7) (61, 96–98).

A model organism often used to study Gram-positive metabolism is *Bacillus subtilis*, a harmless soil inhabitant. The study of iron transport in this bacterium could provide insight into understanding iron transport in highly pathogenic and related group members, *Bacillus cereus* and *Bacillus anthracis*. All three bacteria belong to the *B. cereus* group of bacteria.

binding proteins FpuA and FatB, as well as the *B. subtilis* petrobactin binding protein YclQ will be reviewed.

In Chapter 3, a novel citrate transport system in *B. cereus* will be reported. The system is unique in that the citrate-binding protein binds a trimeric iron-citrate species that is normally very rare in neutral solution. These findings are unique and compelling since the only clear depiction of citrate transport in bacteria is in the Gram-negative system of proteins related to FecA, in which the siderophore-binding protein binds to a ferric citrate dimer or citrate alone (99).

Both *B. anthracis* and a related bacterium, *B. licheniformis*, synthesize and secrete a polyglutamic acid capsule that behaves as a siderophore at a particular stage of the infection cycle (100). The dependence of the bacterium on Fe-sequestration by the capsule will be discussed in Chapter 4, along with structural investigations of the iron-capsule and the ability of the capsule to remove iron from human ferric transferrin.

Siderocalin-mediated mammalian iron transport

Withholding iron from bacteria is one method mammalian hosts such as humans have to fight infections. Siderocalin is a main player in this host defense and is only secreted as an immune response as part of the neutrophil granules of white blood cells. It was around two decades ago when evidence was reported for the antibacterial role of Siderocalin. Since then, the list of possible roles of Siderocalin has grown, since its expression has been linked to several non-disease cases such as early nephrogenesis or modulation of intracellular iron stores (80, 81, 101). Furthermore, Siderocalin has been designated as a biomarker in several conditions such as acute kidney injury, gastric and ovarian cancers and psoriasis (102–104).

The focus of Chapter 5 will be on the role of Siderocalin as an iron delivery protein and a rigidified definition of human siderophores. The equivalent of an organic cofactor is necessary for any Siderocalin-iron interaction, since Siderocalin cannot bind iron directly. A discussion of whether the Siderocalin mediates inflammation, including iron-induced inflammation is presented in Chapter 6.

Conclusion

How both hosts and pathogens strive to restore the delicate concentration of iron needed for survival without incurring iron-induced damage has been endlessly fascinating to the world of scientists, especially when considered in the context of host-pathogen coevolution. In general, iron transport in living systems is a topic important to nearly all because it is relevant to the survival of most living organisms on Earth. Fundamental processes of iron transport must be understood in both bacteria and humans if there is to be a way for humans to combat bacterial infections, especially those caused by pathogenic bacteria for which no current effective treatment exists. Furthermore, mapping and understanding iron transport routes in humans could shed light on methods to remedy human problems with iron homeostasis such as iron overload or iron deficiency. This manuscript highlights details of iron transport in both pathogenic

bacteria from the *B. cereus* group of bacteria and in humans that would be useful for clinical communities as well as those plainly fascinated by science.

References

1. Jordan TH (1979) Structural geology of the Earth's interior. *PNAS* 76:4192–4200.
2. W.F. McDonough, S-s. Sun (1995) The composition of the Earth. *Chemical Geology* 120:223–253.
3. N. N. Greenwood, A. Earnshaw (1984) *Chemistry of the Elements* (Pergammon, New York). 2nd Ed.
4. Hanzlik M et al. (2000) Superparamagnetic Magnetite in the Upper Beak Tissue of Homing Pigeons. *Biometals* 13:325–331.
5. Blakemore R (1975) Magnetotactic Bacteria. *Science* 190:377–379.
6. Frankel R, Blakemore R, Wolfe R (1979) Magnetite in Freshwater Magnetotactic Bacteria. *Science* 203:1355–1356.
7. Cain SD, Boles LC, Wang JH, Lohmann KJ (2005) Magnetic Orientation and Navigation in Marine Turtles, Lobsters, and Molluscs: Concepts and Conundrums. *Integr Comp Biol* 45:539–546.
8. Walker MM, Dennis TE, Kirschvink JL (2002) The magnetic sense and its use in long-distance navigation by animals. *Current Opinion in Neurobiology* 12:735–744.
9. Lohmann KJ, Putman NF, Lohmann CMF (2008) Geomagnetic imprinting: A unifying hypothesis of long-distance natal homing in salmon and sea turtles. *PNAS* 105:19096–19101.
10. Iron Age (history) -- Britannica Online Encyclopedia Available at: <http://www.britannica.com/EBchecked/topic/294368/Iron-Age> [Accessed February 5, 2013].
11. Childe VG (1950) *What happened in history* (Penguin books).
12. Boyd PW, Ellwood MJ (2010) The biogeochemical cycle of iron in the ocean. *Nature Geoscience* 3:675–682.
13. Delaude L, Laszlo P (1996) A Novel Oxidizing Reagent Based on Potassium Ferrate(VI)1. *J Org Chem* 61:6360–6370.
14. Sharma VK (2010) Oxidation of nitrogen-containing pollutants by novel ferrate(VI) technology: A review. *Journal of Environmental Science and Health, Part A* 45:645–667.

15. Licht S (1999) Energetic Iron(VI) Chemistry: The Super-Iron Battery. *Science* 285:1039–1042.
16. Kazama F (1994) Inactivation of coliphage Q β by potassium ferrate. *FEMS Microbiology Letters* 118:345–349.
17. Crabtree RH (2011) *The Organometallic Chemistry of the Transition Metals* (John Wiley & Sons).
18. Thomas JM, Thomas WJ (1996) *Principles and Practice of Heterogeneous Catalysis* (Wiley).
19. Freyschlag CG, Madix RJ (2011) Precious metal magic: catalytic wizardry. *Materials Today* 14:134–142.
20. Blanchard S et al. (2012) Non-Innocent Ligands: New Opportunities in Iron Catalysis. *European Journal of Inorganic Chemistry* 2012:376–389.
21. Fürstner A et al. (2008) A Cheap Metal for a “Noble” Task: Preparative and Mechanistic Aspects of Cycloisomerization and Cycloaddition Reactions Catalyzed by Low-Valent Iron Complexes. *J Am Chem Soc* 130:1992–2004.
22. Bouwkamp MW, Lobkovsky E, Chirik PJ (2005) Bis(imino)pyridine Iron(II) Alkyl Cations for Olefin Polymerization. *J Am Chem Soc* 127:9660–9661.
23. Moreau B, Wu JY, Ritter T (2009) Iron-Catalyzed 1,4-Addition of α -Olefins to Dienes. *Org Lett* 11:337–339.
24. Fleischhacker AS, Kiley PJ (2011) Iron-containing transcription factors and their roles as sensors. *Current Opinion in Chemical Biology* 15:335–341.
25. Gray HB (2005) Long-Range Electron Transfer Special Feature: Long-range electron transfer. *Proceedings of the National Academy of Sciences* 102:3534–3539.
26. Guengerich FP (2007) Mechanisms of cytochrome P450 substrate oxidation: MiniReview. *Journal of Biochemical and Molecular Toxicology* 21:163–168.
27. Ortiz de Montellano PR, De Voss JJ (2002) Oxidizing species in the mechanism of cytochrome P450. *Natural Product Reports* 19:477–493.
28. Raymond KN, Carrano CJ (1979) Coordination chemistry and microbial iron transport. *Accounts of Chemical Research* 12:183–190.
29. Reynolds CH (1988) An AM1 theoretical study of the structure and electronic properties of porphyrin. *The Journal of Organic Chemistry* 53:6061–6064.

30. Ghosh A (1997) Theoretical Comparative Study of Free Base Porphyrin, Chlorin, Bacteriochlorin, and Isobacteriochlorin: Evaluation of the Potential Roles of ab Initio Hartree–Fock and Density Functional Theories in Hydroporphyrin Chemistry. *The Journal of Physical Chemistry B* 101:3290–3297.
31. Meunier B, De Visser SP, Shaik S (2004) Mechanism of Oxidation Reactions Catalyzed by Cytochrome P450 Enzymes. *Chemical Reviews* 104:3947–3980.
32. Guengerich FP (2001) Common and Uncommon Cytochrome P450 Reactions Related to Metabolism and Chemical Toxicity. *Chem Res Toxicol* 14:611–650.
33. Rittle J, Green MT (2010) Cytochrome P450 Compound I: Capture, Characterization, and C-H Bond Activation Kinetics. *Science* 330:933–937.
34. Martin W, Baross J, Kelley D, Russell MJ (2008) Hydrothermal vents and the origin of life. *Nature Reviews Microbiology*. Available at: <http://www.readcube.com/articles/10.1038/nrmicro1991> [Accessed January 31, 2013].
35. Imlay JA (2006) Iron-sulphur clusters and the problem with oxygen. *Molecular Microbiology* 59:1073–1082.
36. Russell MJ, Martin W (2004) The rocky roots of the acetyl-CoA pathway. *Trends Biochem Sci* 29:358–363.
37. Dance I (2011) Electronic Dimensions of FeMo-co, the Active Site of Nitrogenase, and Its Catalytic Intermediates. *Inorg Chem* 50:178–192.
38. Einsle O et al. (2002) Nitrogenase MoFe-Protein at 1.16 Å Resolution: A Central Ligand in the FeMo-Cofactor. *Science* 297:1696–1700.
39. Volbeda A et al. (1996) Structure of the [NiFe] Hydrogenase Active Site: Evidence for Biologically Uncommon Fe Ligands¹. *J Am Chem Soc* 118:12989–12996.
40. Higuchi Y, Yagi T, Yasuoka N (1997) Unusual ligand structure in Ni–Fe active center and an additional Mg site in hydrogenase revealed by high resolution X-ray structure analysis. *Structure* 5:1671–1680.
41. Evans DJ, Pickett CJ (2003) Chemistry and the hydrogenases. *Chem Soc Rev* 32:268–275.
42. Thayer MM, Ahern H, Xing D, Cunningham RP, Tainer JA (1995) Novel DNA binding motifs in the DNA repair enzyme endonuclease III crystal structure. *EMBO J* 14:4108–4120.

43. Lloyd SJ, Lauble H, Prasad GS, Stout CD (1999) The mechanism of aconitase: 1.8 Å resolution crystal structure of the S642a: citrate complex. *Protein Sci* 8:2655–2662.
44. Rouault TA et al. (1992) An iron-sulfur cluster plays a novel regulatory role in the iron-responsive element binding protein. *Biometals* 5:131–140.
45. Hentze MW, Kühn LC (1996) Molecular control of vertebrate iron metabolism: mRNA-based regulatory circuits operated by iron, nitric oxide, and oxidative stress. *PNAS* 93:8175–8182.
46. Beinert H, Kiley P (1996) Redox control of gene expression involving iron-sulfur proteins. Change of oxidation-state or assembly/disassembly of Fe-S clusters? *FEBS Letters* 382:218–219.
47. Gaudu P, Weiss B (1996) SoxR, a [2Fe-2S] transcription factor, is active only in its oxidized form. *PNAS* 93:10094–10098.
48. Hidalgo E, Bollinger JM Jr, Bradley TM, Walsh CT, Dimple B (1995) Binuclear [2Fe-2S] clusters in the Escherichia coli SoxR protein and role of the metal centers in transcription. *J Biol Chem* 270:20908–20914.
49. Winterbourn CC (1995) Toxicity of iron and hydrogen peroxide: the Fenton reaction. *Toxicology Letters* 82-83:969–974.
50. Henle ES (1996) Oxidative Damage to DNA Constituents by Iron-mediated Fenton Reactions. THE DEOXYCYTIDINE FAMILY. *Journal of Biological Chemistry* 271:21167–21176.
51. Fuqua BK, Vulpe CD, Anderson GJ (2012) Intestinal iron absorption. *Journal of Trace Elements in Medicine and Biology* 26:115–119.
52. Weng-In Leong R. D. PD, Ph.D BL (2012) in *Iron Physiology and Pathophysiology in Humans*, Nutrition and Health., eds Anderson GJ, McLaren GD (Humana Press), pp 81–99. Available at: http://link.springer.com/chapter/10.1007/978-1-60327-485-2_5 [Accessed January 31, 2013].
53. Andrews NC (2012) Closing the Iron Gate. *New England Journal of Medicine* 366:376–377.
54. Valerio LG (2007) Mammalian iron metabolism. *Toxicol Mech Methods* 17:497–517.
55. Ganz T, Nemeth E (2012) Heparin and iron homeostasis. *Biochimica et Biophysica Acta (BBA) - Molecular Cell Research* 1823:1434–1443.

56. Bertini I (2007) *Biological Inorganic Chemistry: Structure and Reactivity* (University Science Books).
57. Harrison P (1996) The ferritins: molecular properties, iron storage function and cellular regulation. *Biochimica et Biophysica Acta (BBA) - Bioenergetics* 1275:161–203.
58. Vulpe CD et al. (1999) Hephaestin, a ceruloplasmin homologue implicated in intestinal iron transport, is defective in the sla mouse. *Nature Genetics* 21:195–199.
59. Weinberg ED (1978) Iron and infection. *Microbiol Rev* 42:45–66.
60. Bollmann R (1987) J. J. Bullen and E. Griffiths (Editors), *Iron and Infection — Molecular, Physiological and Clinical Aspects*. IX + 325 S., 70 Abb., 30 Tab. Chichester-New York-Brisbane-Toronto-Singapore 1987. John Wiley and Sons, £ 38.00. ISBN: 0-471-91168-2. *Journal of Basic Microbiology* 27:448–448.
61. Crosa J (2004) *Iron transport in bacteria* (ASM Press, Washington D.C.).
62. Weinberg ED (2000) Microbial pathogens with impaired ability to acquire host iron. *Biometals* 13:85–89.
63. Chow JK, Werner BG, Ruthazer R, Snyderman DR (2010) Increased Serum Iron Levels and Infectious Complications after Liver Transplantation. *Clin Infect Dis* 51:e16–e23.
64. Teehan GS, Ruthazer R, Balakrishnan VS, Snyderman D, Jaber BL (2004) Iron storage indices and risk of bacterial infections in hemodialysis patients. *Hemodial Int* 8:226–232.
65. Reed W, Vichinsky EP (2001) Transfusion therapy: a coming-of-age treatment for patients with sickle cell disease. *J Pediatr Hematol Oncol* 23:197–202.
66. Sandy M, Butler A (2009) Microbial Iron Acquisition: Marine and Terrestrial Siderophores. *Chem Rev* 109:4580–4595.
67. Loomis LD, Raymond KN (1991) Solution equilibria of enterobactin and metal-enterobactin complexes. *Inorg Chem* 30:906–911.
68. Crumbliss AL, Harrington JM (2009) in *Advances in Inorganic Chemistry*, ed Rudi van Eldik and Colin D. Hubbard (Academic Press), pp 179–250. Available at: <http://www.sciencedirect.com/science/article/pii/S0898883809002049> [Accessed February 1, 2013].
69. *Inorganic chemistry* (2006) (W.H. Freeman, New York) 4th ed.

70. D J Morton PW (1990) Siderophore-independent acquisition of transferrin-bound iron by *Haemophilus influenzae* type b. *Journal of general microbiology* 136:927–33.
71. Cornelissen CN, Sparling PF (1994) Iron piracy: acquisition of transferrin-bound iron by bacterial pathogens. *Mol Microbiol* 14:843–850.
72. Wooldridge K (1993) Iron uptake mechanisms of pathogenic bacteria. *FEMS Microbiology Reviews* 12:325–348.
73. Posey JE (2000) Lack of a Role for Iron in the Lyme Disease Pathogen. *Science* 288:1651–1653.
74. Bonnah RA, Yu R, Schryvers AB (1995) Biochemical analysis of lactoferrin receptors in the Neisseriaceae: identification of a second bacterial lactoferrin receptor protein. *Microb Pathog* 19:285–297.
75. Gray-Owen SD, Loosmore S, Schryvers AB (1995) Identification and characterization of genes encoding the human transferrin-binding proteins from *Haemophilus influenzae*. *Infect Immun* 63:1201–1210.
76. Schryvers AB, Morris LJ (1988) Identification and characterization of the transferrin receptor from *Neisseria meningitidis*. *Mol Microbiol* 2:281–288.
77. Schryvers AB (1989) Identification of the transferrin- and lactoferrin-binding proteins in *Haemophilus influenzae*. *J Med Microbiol* 29:121–130.
78. Correnti C, Strong RK (2012) Mammalian Siderophores, Siderophore-binding Lipocalins, and the Labile Iron Pool. *Journal of Biological Chemistry* 287:13524–13531.
79. Goetz DH et al. (2002) The Neutrophil Lipocalin NGAL Is a Bacteriostatic Agent that Interferes with Siderophore-Mediated Iron Acquisition. *Molecular Cell* 10:1033–1043.
80. Bao G et al. (2010) Iron traffics in circulation bound to a siderocalin (Ngal)–catechol complex. *Nature Chemical Biology* 6:602–609.
81. Yang J et al. (2002) An Iron Delivery Pathway Mediated by a Lipocalin. *Molecular Cell* 10:1045–1056.
82. Goetz DH et al. (2000) Ligand Preference Inferred from the Structure of Neutrophil Gelatinase Associated Lipocalin †. *Biochemistry* 39:1935–1941.

83. Hoette TM, Abergel RJ, Xu J, Strong RK, Raymond KN (2008) The Role of Electrostatics in Siderophore Recognition by the Immunoprotein Siderocalin¹. *J Am Chem Soc* 130:17584–17592.
84. Johnson EE et al. (2010) Siderocalin inhibits the intracellular replication of *Mycobacterium tuberculosis* in macrophages. *FEMS Immunology & Medical Microbiology* 58:138–145.
85. Flo TH et al. (2004) Lipocalin 2 mediates an innate immune response to bacterial infection by sequestering iron. *Nature* 432:917–921.
86. Berger T (2006) Lipocalin 2-deficient mice exhibit increased sensitivity to *Escherichia coli* infection but not to ischemia-reperfusion injury. *Proceedings of the National Academy of Sciences* 103:1834–1839.
87. Koppisch AT et al. (2005) Petrobactin is the Primary Siderophore Synthesized by *Bacillus anthracis* Str. Sterne under Conditions of Iron Starvation. *Biometals* 18:577–585.
88. Abergel RJ et al. (2006) Anthrax pathogen evades the mammalian immune system through stealth siderophore production. *Proceedings of the National Academy of Sciences* 103:18499–18503.
89. Abergel RJ, Zawadzka AM, Raymond KN (2008) Petrobactin-Mediated Iron Transport in Pathogenic Bacteria: Coordination Chemistry of an Unusual 3,4-Catecholate/Citrate Siderophore¹. *J Am Chem Soc* 130:2124–2125.
90. Wilson MK, Abergel RJ, Arceneaux JEL, Raymond KN, Byers BR (2010) Temporal production of the two *Bacillus anthracis* siderophores, petrobactin and bacillibactin. *Biometals* 23:129–134.
91. Stintzi A, Barnes C, Xu J, Raymond KN (2000) Microbial iron transport via a siderophore shuttle: A membrane ion transport paradigm. *Proceedings of the National Academy of Sciences* 97:10691–10696.
92. Braun V (1998) Pumping Iron Through Cell Membranes. *Science* 282:2202–2203.
93. Faraldo-Gómez JD, Sansom MSP (2003) Acquisition of siderophores in Gram-negative bacteria. *Nature Reviews Molecular Cell Biology* 4:105–116.
94. Moeck GS, Coulton JW (1998) TonB-dependent iron acquisition: mechanisms of siderophore-mediated active transport†. *Molecular Microbiology* 28:675–681.
95. Postle K, Kadner RJ (2003) Touch and go: tying TonB to transport. *Molecular Microbiology* 49:869–882.

96. Zawadzka AM et al. (2009) Characterization of a *Bacillus subtilis* transporter for petrobactin, an anthrax stealth siderophore. *Proceedings of the National Academy of Sciences* 106:21854–21859.
97. Brown JS, Holden DW (2002) Iron acquisition by Gram-positive bacterial pathogens. *Microbes Infect* 4:1149–1156.
98. Davidson AL, Dassa E, Orelle C, Chen J (2008) Structure, Function, and Evolution of Bacterial ATP-Binding Cassette Systems. *Microbiology and Molecular Biology Reviews* 72:317–364.
99. Yue WW, Grizot S, Buchanan SK (2003) Structural Evidence for Iron-free Citrate and Ferric Citrate Binding to the TonB-dependent Outer Membrane Transporter FecA. *Journal of Molecular Biology* 332:353–368.
100. Jang J et al. (2011) The Poly- γ -d-Glutamic Acid Capsule of *Bacillus anthracis* Enhances Lethal Toxin Activity. *Infect Immun* 79:3846–3854.
101. Mori K (2005) Endocytic delivery of lipocalin-siderophore-iron complex rescues the kidney from ischemia-reperfusion injury. *Journal of Clinical Investigation* 115:610–621.
102. Cho H, Kim J-H (2009) Lipocalin2 Expressions Correlate Significantly With Tumor Differentiation in Epithelial Ovarian Cancer. *J Histochem Cytochem* 57:513–521.
103. Wang H-J et al. (2010) Expressions of neutrophil gelatinase-associated lipocalin in gastric cancer: a potential biomarker for prognosis and an ancillary diagnostic test. *Anat Rec (Hoboken)* 293:1855–1863.
104. Mallbris L et al. (2002) Neutrophil gelatinase-associated lipocalin is a marker for dysregulated keratinocyte differentiation in human skin. *Exp Dermatol* 11:584–591.

Chapter 2

Petrobactin-mediated Iron Uptake in *B. cereus* Group of Bacteria

Introduction

Some of the most successful bacterial pathogens employ multiple iron acquisition strategies to collect a sufficient supply of the growth-limiting element. Both Gram-negative and Gram-positive bacteria have many iron uptake systems that function under low iron condition in tandem. Both classes of bacteria can directly express receptors for human or host iron-containing proteins such as lactoferrins or transferrins, while some may express their own type of transferrin-like protein and uptake system, as is the case with the FbpA system found in *Neisseria gonorrhoeae* (1–3). Iron heme compounds sensed in the environment may also be imported via specific receptors on the outer membrane (4, 5).

Another iron uptake route is through the secretion and binding of iron by siderophores, or small molecule iron chelators. Recall that these siderophores bind iron with either catecholate, hydroxamate or α -hydroxycarboxylate binding moieties as discussed in Chapter 1. Iron siderophores are actively imported back to the organism

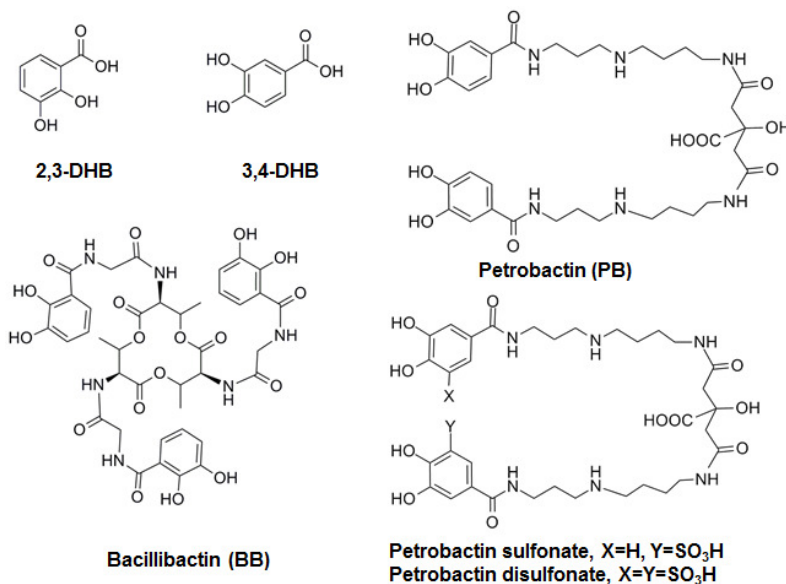


Figure 2.1. Siderophores secreted by *Bacillus* bacteria, particularly *Bacillus thuringiensis*, *Bacillus cereus* and *Bacillus anthracis*.

through ABC-type transporters, which are composed of three components: a substrate or siderophore binding protein (SBP), transmembrane channel, and an ATPase (6).

The SBP is the first site of recognition and selectivity for a siderophore or iron siderophore. Typically SBPs discriminate for particular siderophores based on iron binding moieties, siderophore or iron siderophore size and shape, or chirality (7, 8). Some SBPs are more promiscuous than others, allowing siderophores synthesized from other bacteria, or so called xenosiderophores, to be imported (9, 10). In this way bacteria conserve energy by avoiding the cost of siderophore biosynthesis.

The *Bacillus cereus* group of bacteria includes some extremely pathogenic species such as *Bacillus cereus*, a potentially enterotoxigenic pathogen in humans, and *Bacillus anthracis*, the lethal anthrax pathogen. The bacterium *B. thuringiensis* also belongs to this group of bacteria and is the cause of potentially lethal digestive stress to insects. Members of this group can synthesize and secrete the siderophores bacillibactin (BB) and petrobactin (PB) (Fig. 2.1).

Bacillibactin binds iron with three 2,3-catecholamides that are tethered to a chiral trilactone ring composed of threonine subunits and glycine spacers. It has the second-highest affinity for ferric iron ($K_f = 10^{48}$) of the natural iron chelators (11). Petrobactin binds iron with an α -hydroxycarboxylate and two 3,4-catecholamides. Its affinity for iron is orders of magnitude lower than that of bacillibactin ($K_f \sim 10^{23}$) yet this siderophore garnered much attention with its unprecedented 3,4-catecholamide iron binding moieties that were tied to the ability of petrobactin to evade sequestration by the human immune protein Siderocalin (12–16). Petrobactin was thus termed a ‘stealth siderophore’ since it is could bind iron without inactivation by Siderocalin.

Since petrobactin-mediated iron uptake by bacteria is unaffected by Siderocalin, alternative routes to inhibiting this pathway could be related to its native import systems in *Bacillus* spp. *Bacillus subtilis* is a prototypical member of the *B. cereus* group of bacteria. An innocuous soil inhabitant, *B. subtilis* is often used to study its pathogenic *Bacillus* relatives.

The iron-petrobactin uptake proteins of *Bacillus* may be an attractive target for anti-bacterial strategies being developed. Thus the elucidation of each step in the petrobactin import pathway at the lipid membrane could be of crucial importance for developing effective ways to inhibit the growth of petrobactin-secreting bacteria.

The petrobactin-binding protein in *B. subtilis* was identified as YclQ and characterized by crystallography at 1.75 Å resolution (17). The YclQ residues Glu-107, Lys-84 and His-214 are suspected to be responsible for the specific binding of YclQ to substrates. The size of the binding pocket

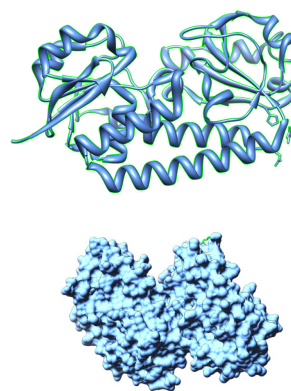


Figure 2.2. Ribbon structure drawing (top) and space-filling depiction (bottom) of YclQ from *B. subtilis*.

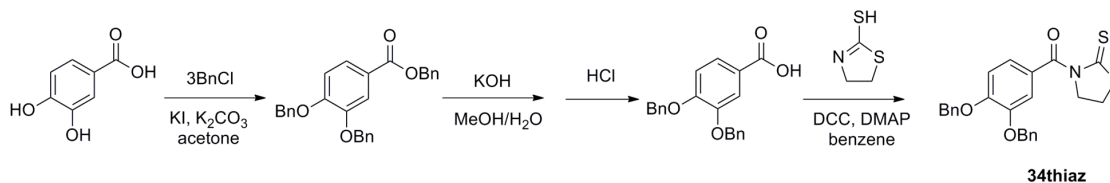
is also large enough to accommodate siderophores with larger shapes, such as Fe(PB). Zawadzka et al. also quantified YclQ affinity for various siderophores. YclQ specifically binds 3,4-catechol siderophores such as petrobactin and 3,4-dihydroxybenzoic acid, whereas its affinity for 2,3-catechol siderophores is orders of magnitude weaker and suggests nonspecific binding (17). Fe(PB) is photolysable since the α -hydroxycarboxylate, when bound to iron, is photoactive and can decarboxylate to the petrobactin photoproduct (PB^v) (Fig. 2.1). Zawadzka et al. showed that Fe(PB^v) has an even lower affinity for YclQ than Fe-PB. An interesting result is that the iron-free, or apo-PB has a higher affinity for YclQ than Fe(PB).

Sulfonated petrobactins also exist (Fig. 2.1), but are secreted by marine bacteria (*Marinobacter aquaeolei* and *Marinobacter hydrocarbonoclasticus*) that are not closely related *Bacillus* bacteria. Whether these siderophores could be viable iron chelators for *Bacillus* transport systems was addressed.

Results

Synthesis of petrobactin models

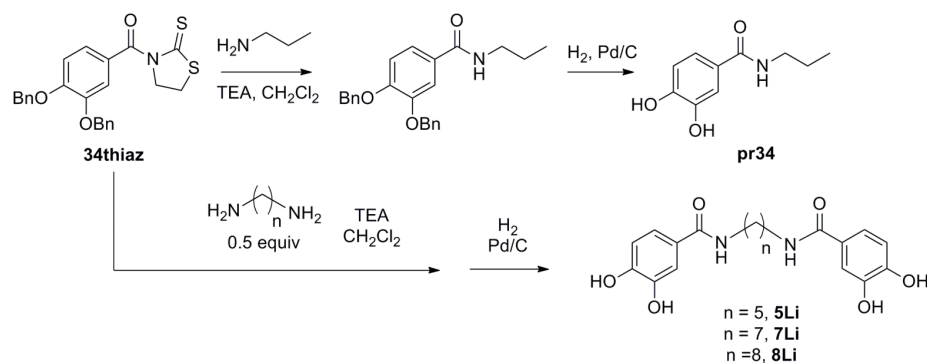
To investigate the trend in apo and ferric(PB) binding and also to probe whether *Marinobacter* siderophores could be used by *Bacillus*, synthetic PB models were made. All PB models were synthesized from a (3,4-bis(benzyloxy)phenyl)(2-thioxothiazolidin-3-yl)methanone precursor (Scheme 2.1), named **34thiaz** throughout this manuscript.



Scheme 2.1. Synthesis of **34thiaz** (3,4-bis(benzyloxy)phenyl)(2-thioxothiazolidin-3-yl)methanone). BnCl = benzyl chloride, DCC = N, N'-dicyclohexylcarbodiimide, DMAP = 4-dimethylaminopyridine.

The synthesis is published elsewhere (18) but briefly begins with the benzylation of commercially available 3,4-dihydroxybenzoic acid via a Finkelstein reaction. The tribenzylated product is purified by silica column chromatography and saponified, followed by coupling to 2-mercaptotiazoline under standard amide coupling conditions to give **34thiaz** in 83% yield.

A simple bidentate catecholamide, 3,4-dihydroxy-*N*-propylbenzamide or **pr34**, was synthesized by the addition of freshly distilled propylamine to **34thiaz** in methylene

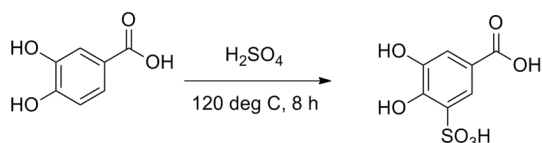


Scheme 2.2. The conversion of **34thiaz** to bidentate or tetradentate catechols as PB mimics. TEA = triethylamine.

chloride with 1% triethylamine (Scheme 2.2). Hydrogeneolysis of the benzyl groups was achieved by reduction with Pd/C catalyst and hydrogen at 1300 psi in a Parr bomb. Tetradentate PB mimics were synthesized analogously, using 0.5 equivalents of a diamine. The ligands **5Li**, **7Li** and **8Li** were synthesized according to Scheme 2.2.

Sulfonation of 3,4-catechols

Sulfonation of free catechols is typically achieved by dissolving the catechol in fuming sulfuric acid and stirring under ambient conditions, with completion of the reaction in less than 12 hours (19, 20). However, such chemistry was unsuccessful for 3,4-catecholamide substrates, so



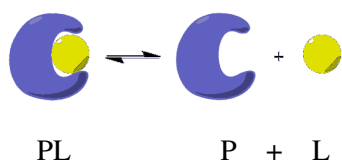
Scheme 2.3. Sulfonation of 3,4-catechol based compounds is achieved by heating the free catechol in 12M sulfuric acid for no longer than 8 hours.

other methods were pursued. The installation of a sulfonate group on 3,4-catecholamides was eventually achieved by heating the free catechol in 12M sulfuric acid to reflux for 5-8 hours (Scheme 2.3) (21). The sulfonated products were precipitated with acetonitrile in nearly 85% yield.

Binding and growth studies with YclQ in B. subtilis

Working concentrations of the PB-binding protein of *B. subtilis*, YclQ, were determined by bicinchoninic acid (BCA) assay (22). *In vitro* testing of affinity between synthesized ligands YclQ was monitored by fluorescence quenching assays. In these assays the inherent protein fluorescence is quenched upon addition of a ligand which

binds specifically to the protein active site. The quenched fluorescence eventually levels off, and a plot of molar equivalents of ligand added against fluorescence values at a certain wavelength is generated. These plots can be fit to a curve using non-linear least



$$K_d = \frac{[\text{P}][\text{L}]}{[\text{PL}]}$$

Figure 2.3. Definition of dissociation constant, K_d , for a protein (P) and ligand (L) complex.

squares regression analysis as computed by the program Hyperquad, from which a protein-ligand dissociation constant, K_d as defined in Fig. 2.3, can be calculated (Fig. 2.4) (23).

Generally, a 100 nM solution of YclQ was titrated with up to twenty equivalents of ligand to ensure equilibrium was reached. Both ferric and apo ligands were tested (Fig. 2.4). Nonsulfonated ferric tetradentate ligands exhibit the highest affinity for YclQ. The ferric *bis*dihydroxybenzoic acid complex ($\text{Fe}(\text{34DHB})_2$), determined as the *bis* complex by speciation calculations, has the highest affinity for YclQ. The data set provided in Fig. 2.4

for $\text{Fe}(\text{34DHB})_2$ is based on less than three equivalents of ligand, since this data set was used to confirm the K_d already reported in reference (17).

The apo versions of nonsulfonated tetradentate ligands are specifically bound by YclQ, but with lower affinity than the ferric counterparts. For both apo and ferric ligands, sulfonation decreased the compatibility of a given ligand with the PB-binding protein. The affinities were orders of magnitude lower, as can be quantitatively compared by the K_d values listed in Table 2.1.

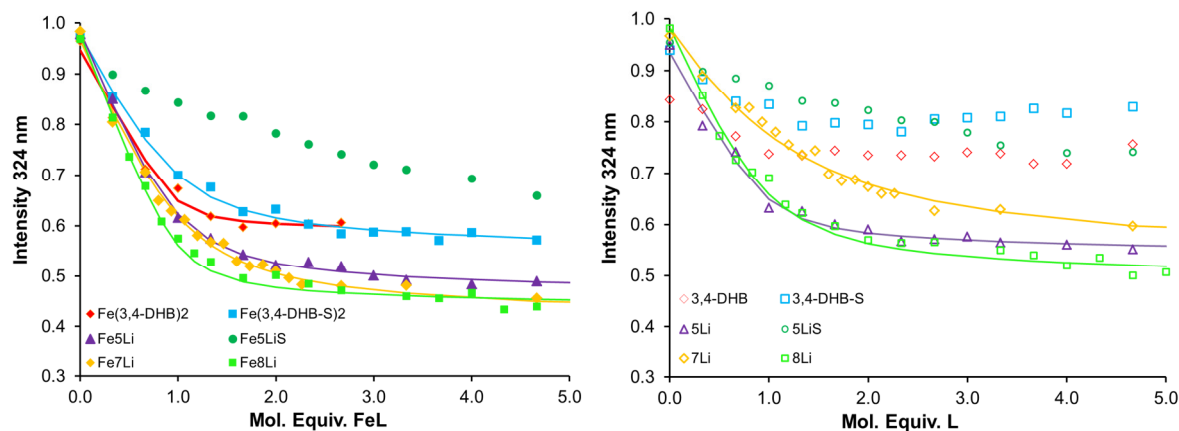


Figure 2.4. YclQ fluorescence quenching assay results with ferric-ligands (left) and apo-ligands (right). Fitted curves (lines) are the result of specifically bound ligands in which experimental observables (data points) could be fit with nonlinear regression lines by Hyperquad.

A qualitative measurement of *B. subtilis* growth when supplemented with PB mimics was obtained by disc diffusion assays. The results of these assays demonstrate whether a given ligand can promote bacterial growth. Wild-type and YclQ-mutant strains were grown in LB medium supplemented with appropriate antibiotics. The cells were washed twice with tris-EDTA buffer and twice with sterile water, diluted 100 fold and added to 0.7% noble agar that was cooled to 45 degrees Celsius. Aliquots of 3 mL were overlaid onto LB agar plates supplemented with 0.5 mM 2,2'-dipyridyl. Sterile paper discs infused with 20 nanomoles of ligand were placed on the agar overlays, incubated overnight at 37 degrees Celsius. Growth was quantitatively measured the following day.

Table 2.1. YclQ dissociation constants for synthetic PB mimics. The values for apo and ferric PB, PB^v and 3,4-DHB are designated with an asterisk as reported by Zawadzka et al (17).

Ligand	K _d (nM)	Ferric Ligand	K _d (nM)
*34DHB	137(18)	*Fe(34DHB) ₂	4.2(1)
*PB	35(2)	*Fe(PB)	113(4)
--	--	*Fe(PB ^v)	142(11)
34S	No binding	Fe(34S) ₂	13.8(4)
5Li	7.2(4)	Fe-5Li	11.2(2)
5LiS	195(3)	Fe-5LiS	409(1)
7Li	57(4)	Fe-7Li	19.0(2)
8Li	14(3)	Fe-8Li	5.2(9)

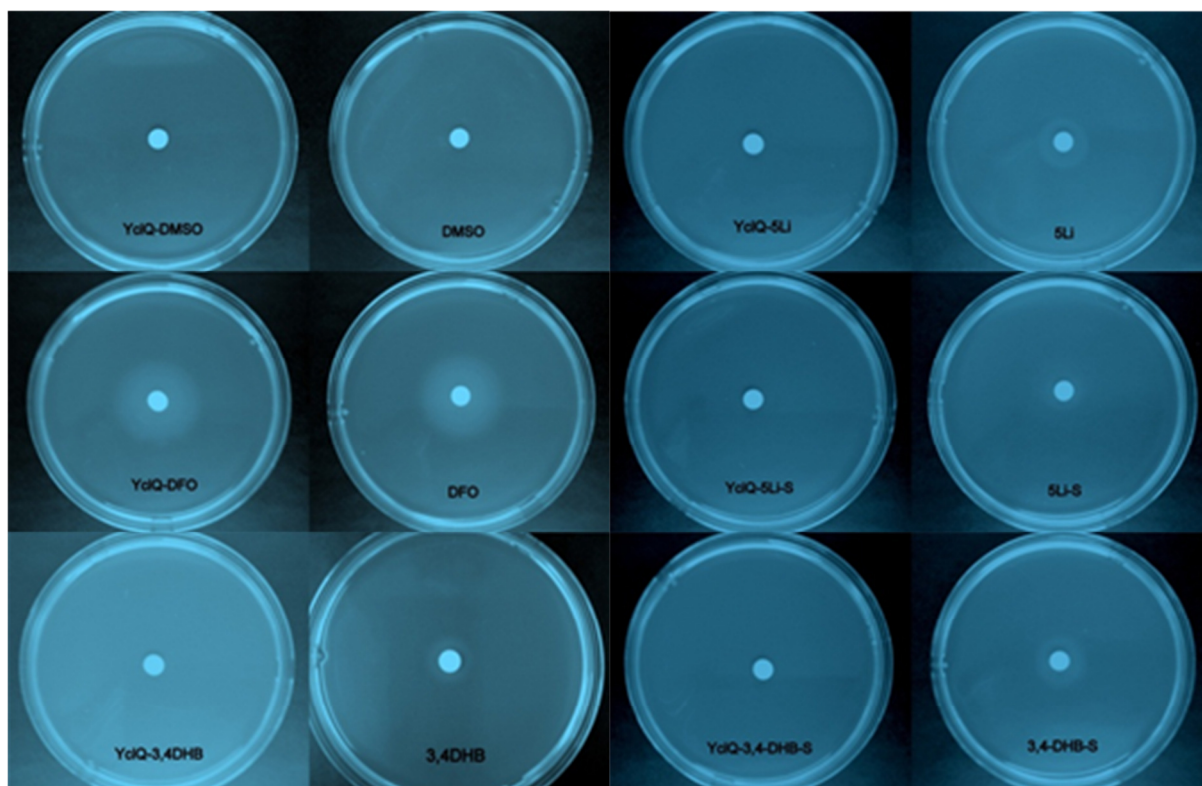


Figure 2.5. Disc-diffusion assays showing *B. subtilis* growth when supplemented with PB mimics. A halo around the white disc signifies bacterial growth. Wild-type (columns 2 and 4) and YclQ mutant (columns 1 and 3) strains were compared. DMSO was the negative control and desferrioxamine B, or DFO, is a tris-hydroxamate siderophore for which *B. subtilis* has an uptake system for.

Wild-type strains are shown in columns 2 and 4 of Figure 2.5 and YclQ mutants are shown in columns 1 and 3. Appropriate negative (DMSO) and positive (desferrioxamine B, or DFO) controls were done to show background and positive growth, respectively. The ligand 5Li was used to represent the tetradentate PB mimics, 5LiS represents sulfonated tetradentate ligands, and sulfonated 3,4-dihydroxybenzoic acid (3,4DHBS) was used to observe growth supported by a bidentate sulfonated PB mimic. *B. subtilis* growth is supported by both 5Li and 3,4DHBS to similar extents, whereas 5LiS does not give a positive result for bacterial growth. These results roughly correlate with the YclQ binding constants determined *in vitro*, which shows that nonsulfonated tetradentate ligands and the sulfonated bidentate ligand 3,4DHBS both support growth sufficiently.

Quantitative *in vivo* studies were performed in which the optical density of bacteria culture at 600 nm (OD_{600}) was monitored over several hours in 96 well plates. Tetradentate ligand solutions were 0.4 mM and bidentate ligands were 1.2 mM. Bacterial cultures were washed twice with Tris-EDTA buffer and twice with sterile Millipore water. Pellets were reconstituted in sterile water and added to iron-limited media

containing different ligand solutions. Optical densities were measured by an automated spectrophotometer every 15 minutes for several hours.

The addition of PB mimics to wild type cultures increased the growth of wild type bacteria compared to the culture with no ligand added (Fig. 2.6). The exception is in the case of the 5LiS ligand, in which wild type growth is delayed. This ligand has the same growth delay effect in the YclQ mutant cultures. While YclQ mutant cultures, in general, experience a slightly delayed growth due to the ligand competition between PB mimics and natural *B. subtilis* siderophores that are in the media, the addition of 5LiS results in the most extreme growth delay. This result suggests that the 5LiS ligand is a competitor with natural *B. subtilis* siderophores whether the PB uptake protein is intact or not.

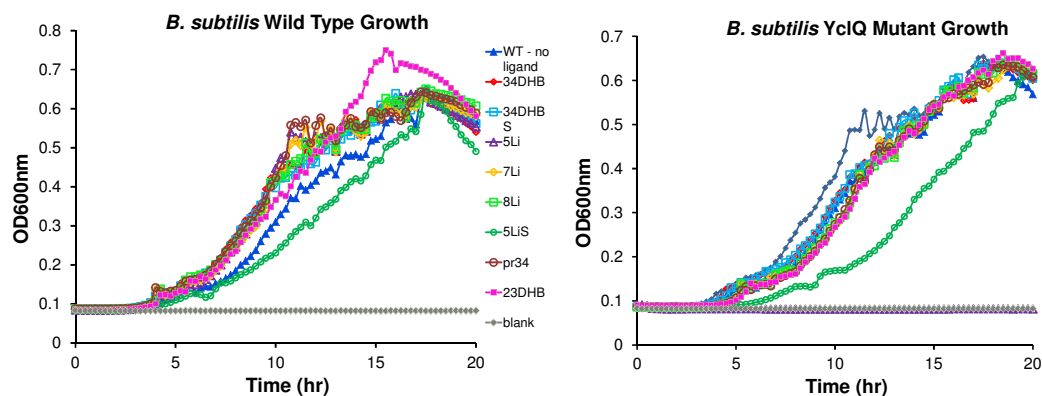


Figure 2.6. *B. subtilis* wild type (left) and YclQ mutant (right) growth curves measured by optical densities at 600 nm. The legend in the middle is applicable to both plots. Closed purple diamonds in the right plot correspond to YclQ mutant culture without addition of ligand.

Binding and growth studies with FatB in B. cereus

Like *B. anthracis*, *B. cereus* has two PB-binding proteins, FpuA and FatB. Our studies with *B. cereus* were focused on FatB, since this protein was readily available and because FpuA does not have a clearly identified ATPase for it to function for *in vivo* experiments. Thus, analogous to *B. subtilis* and YclQ experiments, *in vitro* studies were performed to investigate the affinities of PB mimics with the PB-binding protein FatB. In addition, another ligand (**pr34**) (Scheme 2.2) was synthesized and used in this study. The methodology was maintained as in experiments with YclQ, with the active concentration of FatB being determined by BCA assay. The concentration of FatB for each titration was 100 nM, and the molar equivalents of either ferric or apo ligand added was at least five equivalents.

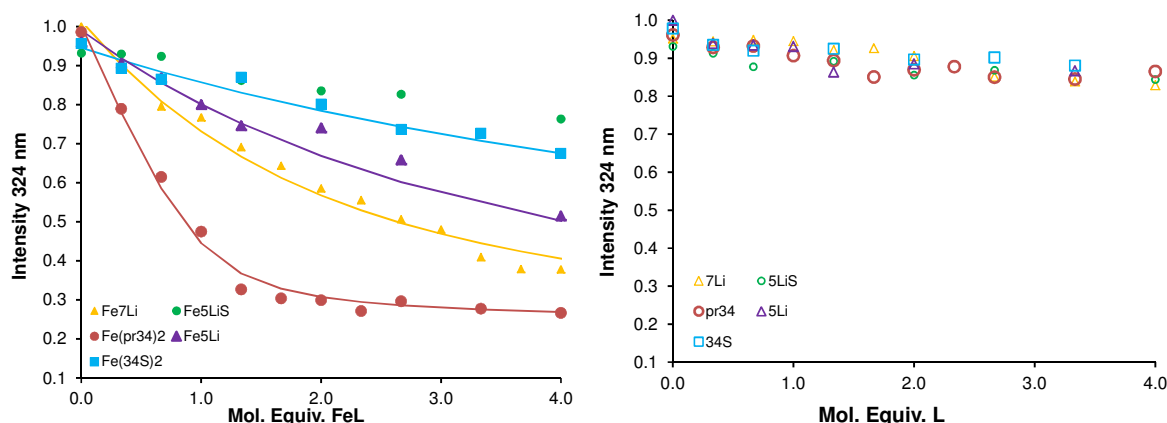


Figure 2.7. FatB fluorescence quenching assays showing FatB affinity for ferric ligands (left) and apo ligands (right).

Of the ferric ligands, FatB had the strongest affinity for **Fe(pr34)₂**, whereas the ferric tetradentate ligands only exhibited mediocre binding that bordered the classification of specific and nonspecific binding (Fig. 2.7). **Fe5LiS** had a very low affinity for FatB. All apo ligands tested did not quench FatB fluorescence. Table 2.2 lists K_d values that can be compared with previously reported K_d s for FatB and natural ligands (24). Ferric complexes of simple, nonsulfonated bidentate ligands were specifically bound by FatB with low dissociation constants. Unlike the binding of PB mimics to YclQ, the nonsulfonated tetradentate ligands and the corresponding ferric complexes had affinities for FatB lower than that of native PB. Furthermore, it seems that sulfonation in substrates for FatB has an even greater effect of decreasing the affinity of FatB for a PB mimic.

Table 2.2. FatB dissociation constants for synthetic PB mimics. The values for apo and ferric PB, PB^v and 34DHB are designated with an asterisk as reported by Zawadzka et al (24).

Ligand	K_D (nM)	Ferric Ligand	K_D (nM)
*34DHB	191(6)	*Fe(34DHB) ₂	1.2(1)
*PB	77(9)	*Fe(PB)	127.1
--	--	*Fe(PB ^v)	135(47)
34DHBS	No binding	Fe(34DHBS) ₂	693(6)
pr34	No binding	Fe(pr34) ₂	9.1(4)
5Li	316(1)	Fe-5Li	313(8)
5LiS	No binding	Fe-5LiS	No binding
7Li	504(6)	Fe-7Li	140(6)

Quantitative *in vivo* growth assays for *B. cereus* wild type and FatB/FpuA mutant strains were carried out by measuring the growth of bacteria (optical density, OD, at 600nm) over several hours. Bacteria were incubated in LB media overnight. Tetradentate ligand solutions were 0.4 mM and bidentate ligands were 1.2

mM. Bacterial cultures were washed twice with Tris-EDTA buffer and twice with sterile Millipore water. Pellets were reconstituted in sterile water and added to iron-limited media containing different ligand solutions. The culture-ligand solutions were distributed appropriately in a 96-well plate, and optical densities were measured by an automated spectrophotometer every 15 minutes for several hours.

B. cereus wild type growth was not affected much by the addition of PB mimics (Fig. 2.8). This may suggest that the bacteria are capable of growing under iron-limited conditions without the synthetic PB mimics inhibiting typical growth under stress conditions.

The PB mimics delay bacterial growth in double mutant *B. cereus*, which suggests that the ligands are adequate competitors for iron with native siderophores. Since these strains lack both the FatB and FpuA PB uptake systems, the iron chelated by PB mimics may be temporarily unavailable for chelation by native siderophores bacillibactin and petrobactin, thus resulting in a growth delay over time.

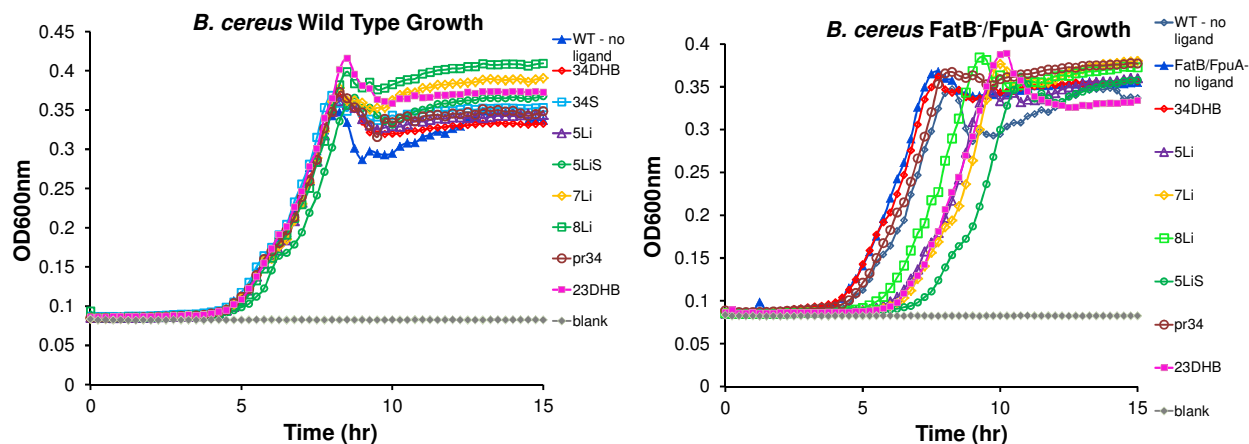


Figure 2.8. *In vivo* growth assays of *B. cereus* wild type (left) and FatB/FpuA mutant (right).

Discussion

Sulfonation of 3,4-catechols by concentrated sulfuric acid

Sulfonation, defined as the transfer of a sulfonate (SO_3^-) group, has a net effect of increasing the water solubility of a substrate (19, 25). While sulfonation is common amongst natural aliphatic compounds, it is less prominent in natural aromatic compounds (25). In nature, sulfonation of aromatic catecholamines results in either the formation of a sulfonate ester via sulfotransferase enzymes, or as a post-translational modification as in the sulfonation of 2,3-catecholamides (25, 26). Another possible mechanism of aromatic sulfonation is the Bucherer reaction, a synthetic scheme in which a sulfonate intermediate is formed (27). In the current literature there is no biosynthetic mechanism proposed for the sulfonation of 3,4-catecholates or 3,4-catecholamides. Evidence for synthetic

sulfonation of 3,4-catecholates can be found in a patent by Frost and Bui, on which the sulfonation chemistry presented in this chapter was based (21). Prior to the success reported here, several alternative methods of sulfonation were tried for 3,4-catecholamide starting materials. These methods were unsuccessful in sulfonating the 3,4-catecholamide on the 2-carbon, as in the purported structures of sulfonated petrobactins. Using the methodology proposed by Frost and Bui, 3,4-catecholamide starting materials were sulfonated using sulfuric acid and heat (21). The ^1H NMR spectrum unambiguously confirms that the sulfonate is bound to the 5-carbon. Coupling constants for aromatic protons correspond to meta-coupled aromatic protons. Considering the difficulty and limited chemistry for sulfonation of 3,4-catecholamides, the 5-SO₃⁻ synthetic compounds were used as models for petrobactin sulfonate and petrobactin disulfonate mediated iron transport in *Bacillus*.

Selectivity of YclQ, the PB binding protein of B. subtilis

The structural elucidation of YclQ by crystallography was a major stepping stone toward understanding PB-mediated iron uptake in *Bacillus*. Compared with the crystal structure of Siderocalin, a protein which does not bind PB or FePB, the structure of YclQ yields important information about the requirements for a protein to bind PB substrates. The ligand-binding calyx must be able to accommodate a ligand with floppy, aliphatic arms, as in PB or FePB.

The YclQ binding results reported by Zawadzka et al. shows that both apo-PB and ferric 3,4-dihydroxybenzoic acid (34DHB) have higher affinities for the protein than FePB (Table 2.1) (17). One would typically expect a PB-uptake protein to have high selectivity and high affinity for FePB. The PB mimics reported in this chapter were synthesized to probe the effect of PB structural changes on YclQ affinity as well as to shed light on the discrepancy in natural PB ligand binding affinities. Specifically, the α -hydroxycarboxylate binding moiety of PB was removed and the backbone was simplified with methylene units. In effect, these PB mimics can be considered structures that are intermediary to PB and to 34DHB.

The ferric PB mimic complexes, **Fe5Li**, **Fe7Li** and **Fe8Li**, had YclQ K_d constants that were higher than **Fe(34DHB)**₂ but lower than FePB. Thus these ferric complexes had higher affinities for YclQ than FePB. The PB mimics have a much shorter backbone than PB which may contribute to a difference in the overall shape of corresponding ferric complexes. A scheme of this speculation is depicted in Scheme 2.4. Geometry optimized structures of gallium complexes with 7Li and 8Li show that these metal complexes are smaller compared to calculated metal-PB structures (Fig. A2.1). The presence of 3,4-catecholates and high affinity of these synthetic compounds for YclQ suggests that the 3,4-catecholate moieties are more important in the selection and ligand binding process than the α -hydroxycarboxylate unit of PB. Furthermore, in the case of **Fe8Li**, the YclQ dissociation constant rivals the constant previously determined for **Fe34DHB**. Of the three nonsulfonated, tetradentate PB mimics there is a lack of a consistent trend correlating the methylene linker length of PB mimics with K_d .



Scheme 2.4. Schematic representation of how tetradentate PB mimics and corresponding ferric complexes (left) would fit better inside the YclQ binding pocket than FePB (right).

The strong interaction between YclQ and **Fe8Li** suggests that eight methylene linkers may be enough physical separation for two 3,4-catecholates to behave like two independent 34DHB moieties that form a *bis*34DHB complex with iron under the fluorescence titration conditions. The dissociation constants come close to being the same numbers when considering the standard error of each K_d (Table 2.2).

Moreover, YclQ showed high affinities for apo-PB mimics, higher than the corresponding ferric complexes. This trend is consistent with the YclQ binding to apo and ferric PB (17). It is typically the ferric complex which binds siderophore binding proteins tighter than their apo counterparts and induces a conformational change in the receptor for translocation. However, the tighter binding of apo siderophores has been reported before, for example in cases of a siderophore shuttle mechanism of iron import (28). Furthermore, these observations may be a result of apo siderophores affecting the protein conformation, perhaps outside of the binding pocket, such that tryptophan environments are altered and protein fluorescence is quenched.

The YclQ response to sulfonated PB mimics is a decrease in overall affinity compared to the respective nonsulfonated PB versions of the ligand. While **Fe(34DHBS)**₂ had a low K_d and supported *B. subtilis* growth in the disc diffusion assay, the sulfonated tetradentate ligand 5LiS and its ferric complex were not compatible ligands for YclQ and *B. subtilis*. The placement of sulfonate groups on the 5-carbon of the catechols is different from petrobactin sulfonates, where the sulfonate groups are installed on the 2-carbons of catechols. The difference in how the sterics of 5-SO₃H versus 2-SO₃H substituted catechols affect iron coordination may also affect the binding of the iron

complex to YclQ. However, the difference in sulfonation position on the catechol should not affect the *B. subtilis* growth results significantly. Using the PB mimics with 5-SO₃H groups as a model for sulfonated PBs, *in vivo* growth experiments suggest that *B. subtilis* may not be able to use sulfonated PBs secreted by *Marinobacter* species.

Selectivity of FatB, the PB binding protein of B. cereus

The two PB-binding proteins of *B. cereus*, FatB and FpuA, are also present and responsible for PB uptake in *B. anthracis*. FpuA, however, does not have an ATPase linked to the transmembrane component and is difficult to study *in vitro* and *in vivo*. Thus we concentrated our efforts in studying FatB, an easily isolable protein that has all of the components of an ABC type importer, in *B. cereus*.

The trend in binding apo PB more tightly than **FePB** is also seen in FatB. However, unlike YclQ of *B. subtilis*, FatB is not particularly selective for 34DHB, **Fe(34DHB)₂** or **Fe(34DHBS)₂**. The ferric complexes **Fe5Li** and **Fe7Li** do not have FatB affinities that indicate stronger binding than FatB to **FePB**. The sulfonated tetradentate ligand and its ferric complex **Fe5LiS** do not have a specific binding affinity for FatB. By this *in vitro* selectivity alone, FatB has more specific requirements for binding than YclQ. Perhaps the α -hydroxycarboxylate unit of PB is required for FatB recognition, which could possibly be related to downstream iron-release mechanisms that occur intracellularly. Sulfonation of a PB mimic could possibly be preventing FatB binding by increasing the steric bulk. The *in vitro* binding results suggest that sulfonated PBs may not be compatible with FatB as iron delivery agents.

In the *B. cereus in vivo* growth studies, both PB-binding proteins FatB and FpuA were not expressed. This means that any PB mimic that delayed growth was a viable iron competitor in the media. **5LiS** delayed growth for the longest period of time, as was the case in *B. subtilis*, but maximum OD₆₀₀ was still achieved. While the synthetic PB mimics chelated iron and delayed growth by competing with native siderophores BB and PB in mutant culture, the wild type growth studies show that the iron complexed by PB mimics did not substantially promote growth. This implies that the PB mimics do not aid the organism beyond its normal capabilities to obtain iron under growth-limiting conditions, nor do these ligands inhibit growth completely.

Conclusion

PB uptake in its native *Bacillus* bacteria was studied to elucidate the requirements for PB-mediated iron uptake and transport. Understanding iron transport in the lethal anthrax pathogen is important since PB is a virulence factor for *B. anthracis*. Siderophore binding proteins are responsible for the initial recognition and transport stages of siderophore-mediated iron import and are key components to studying possible ways of inhibiting PB and iron uptake.

The existence of sulfonated PBs secreted by marine bacteria invoked another question about PB-mediated iron uptake in *Bacillus*: could sulfonated PBs be pirated as exogenous iron chelators in *Bacillus* PB import systems? This was addressed by the

synthesis of sulfonated PB mimics and subsequent use in both *in vitro* and *in vivo* assays with *B. subtilis* and *B. cereus*. While sulfonated PB mimics could bind YclQ and support some growth in *B. subtilis*, such was not the case with FatB and *B. cereus*. *B. subtilis* is an innocuous soil pathogen with fewer requirements for PB-mediated iron transport, whereas the potentially enterotoxic human pathogen *B. cereus* does not accept PB mimics as potential iron delivery agents. The best ferric complex for FatB is ferric petrobactin possibly indicating that the same may be true for the FatB and FpuA systems in *B. anthracis*. While it is possible for exogenous, nonnative chelators in the extracellular milieu to be used for iron import, such is not the case for *B. cereus* and its FatB iron uptake system. Multiple ABC-type iron importers exist, often expressed at once, and it is possible that xenosiderophores could be imported through these other systems. Perhaps *B. cereus* maintains a strict requirement for ligand binding by FatB to ensure the facile release of iron in subsequent steps. FePB is photolabile whereas Fe(34DHB)₂ and Fe(PB mimics) are not, which could hint at a photoreduction step being necessary for PB-mediated iron import in *B. cereus* and potentially *B. anthracis*.

The synthesis of petrobactin analogs and the study of them *in vitro* and *in vivo* has shown that YclQ of *B. subtilis* binds a wider variety of 3,4-catecholate siderophores than FatB of *B. cereus* and potentially *B. anthracis*. Perhaps the ability of YclQ to recognize and specifically bind various 3,4-catecholate siderophores could reflect a means by which the bacterium must survive. It may be more common for siderophores in the soil to be small bidentate or tetradentate chelators as opposed to larger hexadentate siderophores which require more complex biosynthetic machinery. The higher degree of specificity for FatB in *B. cereus* and *B. anthracis* could be explained by the possibility of these pathogenic bacteria having ferric-siderophore uptake systems highly optimized for petrobactin only, where perhaps the iron-release processes down the line may depend on the photoreduction of petrobactin. It is possible that in the time of the life cycle in which these pathogenic bacteria require iron-siderophores that there is little competition from other chelators but also more siderophore-uptake proteins are expressed to ensure iron acquisition at the crucial time.

Experimental

General. All chemicals were obtained from commercial suppliers and used without further purification unless otherwise noted. Chemical analyses were performed by the Microanalytical Services Laboratory, College of Chemistry, University of California, Berkeley, Berkeley, CA 94720. Ultraviolet-visible spectra were measured with a Cary Model 300 Scan spectrophotometer unless otherwise noted. All ¹H NMR and ¹³C NMR spectra were recorded at room temperature in deuterated solvents on an AVQ-400 Bruker FT spectrometer unless otherwise noted. Mass spectrometry experiments were performed by the QB3/Chemistry Mass Spectrometry Facility in B207 Stanley Hall, UC Berkeley. Iron chloride stock solutions in 1 M HCl were standardized by EDTA titration according to the methods of Welcher (29). Tris(hydroxymethyl)aminomethane (Tris) buffered saline solutions were made according to routine protocols (30) except the pH was adjusted to

7.2. All chemicals were purchased from Sigma Aldrich and used without further purification unless otherwise noted.

Fluorescence quenching binding assay. Fluorescence quenching of recombinant YclQ and FatB were measured on a Cary Eclipse fluorescence spectrophotometer. A 5 nm slit band pass for excitation and a 10 nm slit band pass for emission was used with a high voltage detector (PMT = 900V). An excitation wavelength of $\lambda_{\text{exc}} = 280$ nm was used and emission was collected at $\lambda_{\text{em}} = 320$ nm to 340 nm. Measurements were made at a protein concentration of 100 nM in buffered aqueous solutions, plus 32 $\mu\text{g/mL}$ ubiquitin (Sigma) and 5% DMSO. Fluorescence intensities were corrected for dilution due to addition of ligand. Fluorescence data were analyzed by a nonlinear regression analysis of the normalized fluorescence response versus ligand concentration using Hyperquad (23) which allows for a multiwavelength treatment of the data and simultaneously refines all titrations. Dissociation constants were determined from at least three independent titrations.

Ligand solutions preparation. Ligand and ferric-ligand solutions were prepared *in situ*. An aliquot of a DMSO stock solution of the free ligand (12 mM, 25 μL) and FeCl_3 salt (27 mM, 3.7 μL , 0.33 equiv) were combined, vigorously shaken, and diluted with TBS buffer (pH 7.2) to form the metal complexes at a concentration of 0.1 mM (no metal added for apo-ligands). The solutions were vigorously shaken, equilibrated for 1.5 hr and diluted to a final concentration of 20 μM in 5% DMSO/TBS buffer. Apo ligand solutions were prepared analogously without the addition of the metal salt.

Bicinchoninic acid (BCA) Assay. To accurately determine the protein concentration of recombinant YclQ and FatB proteins, the BCA assay was used. The BCA Protein Assay kit was purchased from Pierce. One albumin standard of 1000 $\mu\text{g/mL}$ was made, after which serial diluted solutions were made to make the other albumin standard solutions (100, 250, 500, 750 $\mu\text{g/mL}$). The BCA working solution was made according to the instructions (50:1 Reagent A: Reagent B, or 2000 μL Reagent A with 40 μL Reagent B), and 200 μL of this solution was added to each of 7 wells in a 96-well flat bottomed plate. The first five wells contained 10 μL of the corresponding albumin standard, while the last two wells were reserved for 10 μL (each) of YclQ or FatB samples of unknown concentration. The YclQ or FatB samples were prepared as followed: a 5 μL aliquot was diluted with 45 μL of freshly prepared 100% TBS buffer. The dilution factor (10) was automatically taken into account by the protocol built in to Softmax Pro 5.2 for BCA protein quantification. The plate was incubated at 37 °C for 30 minutes in a Molecular Devices Spectramax Plus 384 microplate reader. Using the Softmax Pro 5.2 software with the experiment setup for BCA protein concentration quantification, the plate was read at 562 nm, with automixing allowed 10 seconds before the first reading.

Disc-diffusion assays. The *B. subtilis* strain yclQd and the complemented mutant strain were grown to late exponential phase in LB medium supplemented with the appropriate antibiotics. The cells were washed twice with TE buffer at pH 8, resuspended in sterile

water, and diluted 1:100 in 0.7% noble agar cooled to 45 degrees C and containing erythromycin (0.3 µg/mL) and chloramphenicol (10 µg/mL) and 2 mM IPTG in the case of the complemented strains. Aliquots of 3 mL of these suspensions were overlaid onto LB agar plates supplemented with 0.5 mM 2,2'-dipyridyl. Sterile paper discs infused with 20 nanomoles of ligands (DMSO, DFO, 34DHB, 34DHBS, 5Li, 5LiS) were placed on the agar overlays, incubated at 37 degrees C overnight, and examined for the presence of zones of growth around the discs.

***Bacillus subtilis* growth assays (OD_{600nm})**

Wild-type and YclQ mutant strains were inoculated on an LB-media plate overnight. After 12 hours, 2-3 colonies of each culture were incubated separately in 3 mL of LB media for 6-7 hours. During incubation, iron-limited media and ligand solutions were prepared. Iron-limited media were composed of the following (below), totaling a volume of 20 mL in a 50 mL Falcon tube. After 6-7 hours of incubation, 1 mL of each culture was pipetted into sterile eppendorf tubes. All work was performed in the biohood. The cultures were centrifuged for 2 min at 8000 rpm. Supernatants were carefully discarded. Pellets were resuspended in 500 µL TE buffer (10 mM Tris and 1 mM EDTA, filtered). These samples were centrifuged three times at 8000 rpm for 2 min. Supernatants were decanted each time. Pellets were washed 3x with 500 µL filtered milliQ water (centrifugation @ 8000 rpm x 2min each). Finally, pellets were reconstituted in 1 mL filtered milliQ water. Aliquoted 25 µL of each culture into 975 µL filtered milliQ water. Five µL of each culture was added to appropriate wells in a 96-well plate. Optical densities were read at 600 nm with an automatic microtitre plate reader immediately after cultures were added to plate wells. Using Spectramax 364 software: set up Kinetics run for 96-well plate. Read for 12:00:00 hr every 00:15:00 (15 min) at 600 nm. Automixed before reading and between reads.

Iron-limited media

Iron-limited media was prepared in a sterile environment (biosafety hood) the same day of intended use. The following were mixed together in a sterile falcon tube:

- 20 µL of 40 mM nicotinic acid
- 16.6 µL of 1M MgSO₄
- 20 µL 36 mM MnSO₄
- 6 µL 1 mM ZnSO₄
- 480 µL 2 mg/mL L-Tryptophan
- 20 µL 100 mM thiamine
- 100 µL 50 mM 2,2'-dipyridyl (concentrations varied in order to promote growth, see main text)
- 4 mL 5X Fe-free media (added by sterile disposable pipette)
- 15.4 mL filtered milliQ water (added by sterile disposable pipette)

Ligand solutions for OD₆₀₀ growth assays

From 4 mM stock solutions of ligands in 100% DMSO, diluted 100 µL into 900 µL milliQ water to obtain 0.4 mM solutions. Ligands used are listed in main text and abbreviations are included in the growth plots. In biohood, diluted 6.5 µL of each ligand

into a sterile eppendorf tube with 1.3 mL of Fe-limited media. Distributed 195 μ L of each ligand-Fe-limited media sample into each of 6 wells (3 wells for wild-type strain, 3 wells for mutant strain) appropriated for that ligand in a 96-well plate (flat bottomed).

***Bacillus cereus* growth assays (OD600nm)**

Wild-type and FatB mutant *B. cereus* strains were inoculated on an LB-media plate overnight. The next morning, 2-3 colonies of each culture were incubated separately in 3 mL of LB media for 6-7 hours. During incubation, iron-limited media and ligand solutions were prepared. Iron-limited media was prepared totaling a volume of 20 mL in a 50 mL Falcon tube. All work was performed in a sanitary environment in a biohood. Ligand solution preparation and culture resuspension protocols were the same as for *B. subtilis* described above.

Synthesis

(3,4-Bis-benzyloxy-phenyl)-(2-thioxo-thiazolidin-3-yl)-methanone (34thiaz).

34thiaz was synthesized according to previously published work (18). ^1H NMR (400 MHz, CDCl_3): δ 7.39 (m, 12H, ArH), 6.96 (d, 1H, ArH), 5.03 (d, 4H, CH_2), 4.40 (t, 2H, CH_2), 3.45 (t, J=?, 2H, CH_2). ^{13}C NMR (75 MHz, CDCl_3): δ 162.60, 153.80, 137.09, 136.58, 128.90, 128.36, 128.28, 122.72, 127.49, 125.92, 125.46, 116.49, 113.14, 71.84, 71.10, 57.07, 53.77, 30.15. (+)FABMS: m/z calc. 434, obs. 434 (MH^+).

3,4-Dihydroxy-N-propyl-benzamide.

4.0 g (9.18 mmol) of (3,4-Bis-benzyloxy-phenyl)-(2-thioxo-thiazolidin-3-yl)-methanone, (34thiaz) was dissolved in 100 ml CH_2Cl_2 . A separate solution of 0.543 g (9.18 mmol) distilled propylamine and 1.28 ml (9.18 mmol) triethylamine were dissolved in 30 ml CH_2Cl_2 . The amine solution was added to the solution of 34thiaz under a nitrogen atmosphere for 2 days. A light yellow, clear solution resulted, which was washed 3x with 75 ml of 1M KOH in 50% brine, 3x with 25 ml 1M HCl, and 3x 20 ml brine. The organic layer was then filtered, dried over MgSO_4 and evaporated to give a white solid. The solid was redissolved in methylene chloride and run through a column, initially packed with 100% CH_2Cl_2 and eluted to 96% CH_2Cl_2 , 4% MeOH. The compound was then deprotected after being stirred with a 50 ml solution of 50:50 acetic acid: HCl. The acid was slowly co-evaporated with methanol and ether to give a clear orange oil. ^1H NMR (400 MHz, CDCl_3): δ 7.41 (m, 12H, ArH), 6.90 (d, 1H, ArH), 6.0 (s, 1H, NH), 5.22 (s, 4H, CH_2), 3.41 (m, 2H, NHCH_2), 1.65 (m, 2H, CH_2), 1.02 (t, 3H, CH_3). ESI(+) 224.13 m/z ($\text{M}+1$). Anal. Calcd (found): C 64.55 (64.42), H 7.67 (7.59), N 6.27 (6.23).

3,4-Dihydroxy, 5-sulfobenzoic acid. Synthesized according to Frost and Bui (21).

Obtained 80% yield, an off-white solid. Product was further purified by centrifuging compound in methanol, decanting supernatant, and repeating. ^1H NMR (400 MHz, MeOD): δ 7.93 (d, J = 2 Hz, 2H, ArH), 7.48 (d, 2H, ArH, J = 2 Hz). ESI(-) 232.97 m/z ($\text{M}-1$).

***N,N'*-1-5-Pentanediylbis(3,4-dihydroxybenzamide), 5Li.**

0.837 g (4.78 mmol) of 1,5-diaminopentane-dihydrochloride salt was dissolved in 25 ml CH₂Cl₂. 1.33 ml (9.56 mmol) of triethylamine was added to the solution and reaction was stirred overnight. The following day, this diamine solution was added to a 200 ml solution of 4.16 g (9.56 mmol) of **34thiaz**, stirring under nitrogen. Another 1.33 ml of triethylamine was subsequently added and the reaction was stirred overnight. The reaction mixture slowly turned from a clear yellow solution to clear solution with white precipitate. The white precipitate was washed 2x with 125 ml 1M HCl, 3x 10 ml 1M KOH, and 2x 20 ml brine. The organic layer was dried, filtered and evaporated. The resulting white solid dissolved in dimethylformamide (DMF) and subsequently deprotected with H₂ and Pd/C at 1500 psi for 8 hours. **5Li** was obtained in 80% yield. ¹H NMR (400 MHz, DMSO): δ 9.34 (s, 2H, ArH), 9.05 (s, 2H, ArH), 8.07 (m, 2H, ArH), 7.23 (s, 2H, ArH), 7.13 (m, 2H, ArH), 6.69 (d, 2H, J = 8.4 Hz, ArH), 3.15 (m, 4H, NHCH₂), 1.46 (m, 4H, CH₂), 1.27 (m, 2H, CH₂). (+)FABMS: m/z calc. 374, obs.374. Anal. Calcd. (found) for C₁₉H₂₂N₂O₆: C, 60.95 (60.90), H, 5.92 (5.95), N, 7.48 (7.42).

5LiS. 5Li (0.048 g, 0.128 mmol) was dissolved in 0.641 mL concentrated sulfuric acid. The clear, colorless solution was heated to 120 degrees C for 8 hours, with a reflux condenser attached to the roundbottom flask and with nitrogen flow. After 3 hours, the reaction turned a dark opaque brown. After 8 hours, the system was cooled to room temperature, then chilled in an ice bath. Dry MeCN (0.6 mL) was added to the chilled system, and the precipitate was collected, washed with minimal dry MeCN and dried *in vacuo* overnight. The next day, dissolved the brown-grey solid in minimal methanol, centrifuged for 20 min @ 13.3 x 1000 rev/min. Decanted supernatant. Repeated centrifugation twice more, obtained off-white solid. 70% yield. ¹H NMR (400 MHz, MeOD): δ 7.64 (d, J = 2 Hz, 2H, ArH), 7.31 (d, 2H, ArH, J = 2 Hz), 3.49 (t, 4H, CONHCH₂), 1.68 (m, 4H, CH₂), 1.50 (m, 2H, CH₂). ESI(-) 533.15 m/z (M-1).

***N,N'*-1-7-Heptanediylbis(3,4-dihydroxybenzamide), 7Li.**

0.729 g (1.67 mmol) of **34thiaz**, was dissolved in 100 ml CH₂Cl₂. 0.109 g (0.837 mmol) 1,7-diaminoheptane was dissolved in a separate solution of 25 ml CH₂Cl₂ and 0.233 ml (1.67 mmol) triethylamine. This amine solution was added to the solution of **34thiaz** under nitrogen and was stirred overnight. The clear, yellow solution turned into a clear colorless solution with white precipitate overnight. The reaction mixture was washed with 2x 125 ml 1M HCl, 2x 125 ml 1M NaOH, 2x 100 ml brine. The organic layer was dried, filtered and evaporated to give an off-white solid. This material was purified by silica column chromatography, with the silica packed in 100% CH₂Cl₂ and eluted to 95% CH₂Cl₂ and 5% MeOH. The product with R_f = 0.22 was collected, concentrated and dissolved in DMF with heat. Subsequent hydrogeneolysis in H₂ and Pd/C at 1500 psi for 8 hours afforded **7Li** in 85% yield. ESI(-): m/z calc. 401, obs. 401. ¹H NMR (400 MHz, DMSO): δ 9.38 (s, 2H, ArH), 9.05 δ 9.34 (s, 2H, ArH), 8.07 (m, 2H, ArH), 7.23 (s, 2H, ArH), 7.12 (m, 2H, ArH), 6.70 (d, 2H, J = 8.4 Hz, ArH), 3.14 (m, 4H, NHCH₂), 1.44 (m, 4H, CH₂), 1.26 (m, 6H, CH₂). Anal. Calcd. (found) for C₂₁H₂₆N₂O₆ • H₂O: C 59.99 (59.28), H 6.71 (6.92), N 6.66 (6.67).

***N,N'*-1-8-Octanediybis(3,4-dihydroxybenzamide), 8Li.** 3,4-benzyloxybenzamide(thiazolide), or **34thiaz**, (1.098 g, 2.52 mmol) was dissolved in 125 mL of chloroform. To this clear yellow solution was added a 25 mL chloroform solution of 1,8-diaminooctane (0.182 g, 12.6 mmol) and triethylamine (0.351 mL, 2.52 mmol). The reaction mixture was stirred overnight under nitrogen, resulting in a clear, colorless solution with white precipitate. The white precipitate was collected and washed with methylene chloride (100 mL) and methanol (40 mL) to give 8Li-Bn₄ in 90% yield. ¹H NMR (400 MHz, d₆-DMSO): δ 8.29 (m, 2H, *NH*), 7.51-7.09 (m, 26*H*, *ArH*), 5.19 (d, 8H, *ArCH*₂), 3.20 (d, 4H, *NHCH*₂*CH*₂), 1.50 (m, 4H, *CH*₂), 1.39 (m, 10H, *CH*₂). (+)FABMS: *m/z* calc. 777, obs. 777 (*MH*⁺). IR (cm⁻¹) 3289.7 (w), 2920.6 (w), 2853.2 (w), 1630.2 (s), 1542.1 (m), 1510.5 (s), 1312.9 (s), 1274.6 (s), 1215.9 (s), 1132.2 (s), 1005.7 (s), 745.15 (m), 731.27 (m), 691.62 (s). A hydrogenolysis catalyzed by 10% Pd/C was carried out to deprotect 8Li-Bn₄ by dissolving 0.520 g (0.669 mmol) of 8Li-Bn₄ in 40 mL dimethylformamide. The solution was heated to dissolve the material. Added 20% mol. equiv (0.268 g) of 10% Pd/C to reaction flask. Charged Parr bomb to 1300 psi, stirred for 48 hours. Filtered catalyst, evaporated most of DMF. Recrystallized with hot methanol and minimal hot water. ¹H NMR (400 MHz, d₄-MeOD): δ 8.16 (t, 2H, *NH*), 7.25 (s, 2H, *ArH*), 7.17 (m, 2H, *ArH*), 6.76 (d, 2H, *ArH*), 3.39 (m, 4H, *NH*₂*CH*₂), 1.57 (m, 4H, *CH*₂), 1.36 (s, 7H, *CH*₂). ¹³C NMR (75 MHz, d₄-MeOD): δ 168.78, 148.51, 144.80, 125.82, 118.97, 114.31, 114.23, 39.45, 29.09, 28.91, 26.55. Anal. Calcd (found): C 63.45 (63.50), H 6.88 (6.93), N 6.73 (6.66).

References

1. Wooldridge K (1993) Iron uptake mechanisms of pathogenic bacteria. *FEMS Microbiology Reviews* 12:325–348.
2. Parker Siburt CJ, Mietzner TA, Crumbliss AL (2012) FbpA — A bacterial transferrin with more to offer. *Biochimica et Biophysica Acta (BBA) - General Subjects* 1820:379–392.
3. Cornelissen CN, Sparling PF (1994) Iron piracy: acquisition of transferrin-bound iron by bacterial pathogens. *Mol Microbiol* 14:843–850.
4. Stoebner JA, Payne SM (1988) Iron-regulated hemolysin production and utilization of heme and hemoglobin by *Vibrio cholerae*. *Infect Immun* 56:2891–2895.
5. Payne SM, Henderson DP (1994) in *Molecular Mechanisms of Bacterial Virulence*, Developments in Plant Pathology., eds Kado CI, Crosa JH (Springer Netherlands), pp 173–184. Available at: http://link.springer.com/chapter/10.1007/978-94-011-0746-4_12 [Accessed March 4, 2013].
6. Davidson AL, Dassa E, Orelle C, Chen J (2008) Structure, Function, and Evolution of Bacterial ATP-Binding Cassette Systems. *Microbiology and Molecular Biology Reviews* 72:317–364.
7. Shanzer A et al. (1993) Siderophore-Mediated microbial iron(III) uptake: An exercise in chiral recognition. *Chirality* 5:359–365.
8. Abergel RJ, Zawadzka AM, Hoette TM, Raymond KN (2009) Enzymatic Hydrolysis of Trilactone Siderophores: Where Chiral Recognition Occurs in Enterobactin and Bacillibactin Iron Transport. *J Am Chem Soc* 131:12682–12692.
9. Miethke M, Kraushaar T, Marahiel MA (2013) Uptake of xenosiderophores in *Bacillus subtilis* occurs with high affinity and enhances the folding stabilities of substrate binding proteins. *FEBS Lett* 587:206–213.
10. Crosa J (2004) *Iron transport in bacteria* (ASM Press, Washington D.C.).
11. Dertz EA, Xu J, Stintzi A, Raymond KN (2006) Bacillibactin-Mediated Iron Transport in *Bacillus subtilis*. *J Am Chem Soc* 128:22–23.
12. Zhang G et al. (2009) Ferric Stability Constants of Representative Marine Siderophores: Marinobactins, Aquachelins, and Petrobactin. *Inorg Chem* 48:11466–11473.
13. Bergeron R (2003) Total synthesis and structure revision of petrobactin. *Tetrahedron* 59:2007–2014.

14. Barbeau K, Zhang G, Live DH, Butler A (2002) Petrobactin, a Photoreactive Siderophore Produced by the Oil-Degrading Marine Bacterium *Marinobacter hydrocarbonoclasticus*. *J Am Chem Soc* 124:378–379.
15. Abergel RJ et al. (2006) Anthrax pathogen evades the mammalian immune system through stealth siderophore production. *Proceedings of the National Academy of Sciences* 103:18499–18503.
16. Abergel RJ, Zawadzka AM, Raymond KN (2008) Petrobactin-Mediated Iron Transport in Pathogenic Bacteria: Coordination Chemistry of an Unusual 3,4-Catecholate/Citrate Siderophore¹. *J Am Chem Soc* 130:2124–2125.
17. Zawadzka AM et al. (2009) Characterization of a *Bacillus subtilis* transporter for petrobactin, an anthrax stealth siderophore. *Proceedings of the National Academy of Sciences* 106:21854–21859.
18. Hoette TM (2009) Siderocalins and siderophores: The competition for iron in mammals and pathogenic bacteria. Available at: <http://search.proquest.com/dissertations/docview/614136454/abstract/13CCB4B872458B3C531/1?accountid=14496> [Accessed March 13, 2013].
19. Weigl FL, Harris WR, Raymond KN (1979) Sulfonated catecholamide analogs of enterobactin as iron sequestering agents. *J Med Chem* 22:1281–1283.
20. Weigl FL, Raymond KN (1980) Specific sequestering agents for the actinides. 3. Polycatecholate ligands derived from 2,3-dihydroxy-5-sulfobenzoyl conjugates of diaza- and tetraazaalkanes. *J Am Chem Soc* 102:2289–2293.
21. Frost J, Bui V (2011) Sulfonation of Polyhydroxyaromatics. Available at: <http://www.freepatentsonline.com/y2011/0046412.html> [Accessed March 6, 2013].
22. Walker JM (1994) *Basic Protein and Peptide Protocols* (Humana Press).
23. Gans, Peter, Sabatini, Antonio, Vacca, Alberto (1996) Investigation of equilibria in solution. Determination of equilibrium constants with the HYPERQUAD suite of programs. *Talanta* 43:1739–1753.
24. Zawadzka AM, Abergel RJ, Nichiporuk R, Andersen UN, Raymond KN (2009) Siderophore-Mediated Iron Acquisition Systems in *Bacillus cereus*: Identification of Receptors for Anthrax Virulence-Associated Petrobactin^{†,‡}. *Biochemistry* 48:3645–3657.
25. Strott CA (2002) Sulfonation and Molecular Action. *Endocrine Reviews* 23:703–732.

26. Budzikiewicz H, Fuchs R, Taraz K, Marek-kozaczuk M, Skorupska A (1998) Dihydropyoverdin- 7-Sulfonic Acids - Unusual Bacterial Metabolites. *Natural Product Letters* 12:125–130.
27. Budzikiewicz H Bacterial Aromatic Sulfonates - A Bucherer Reaction in Nature? *Mini-Reviews in Organic Chemistry* 3:93–97.
28. Stintzi A, Barnes C, Xu J, Raymond KN (2000) Microbial iron transport via a siderophore shuttle: A membrane ion transport paradigm. *Proceedings of the National Academy of Sciences* 97:10691–10696.
29. Welcher FJ (1958) *The analytical uses of ethylenediaminetetraacetic acid* (Van Nostrand).
30. Sambrook J, Russell DW (David W, Sambrook J (2006) (Cold Spring Harbor Laboratory Press, Cold Spring Harbor, N.Y). Available at: <http://www.loc.gov/catdir/toc/ecip0517/2005022077.html> [Accessed March 13, 2013].

Chapter 2 Appendix



Figure A2.1. Solutions of $\text{Fe}(3,4\text{DHB})_2$ and $\text{Fe}(3,4\text{DHBS})_2$. The solutions are slightly different in intensity of purple color and also have different UV-visible spectra (Fig. A2.2).

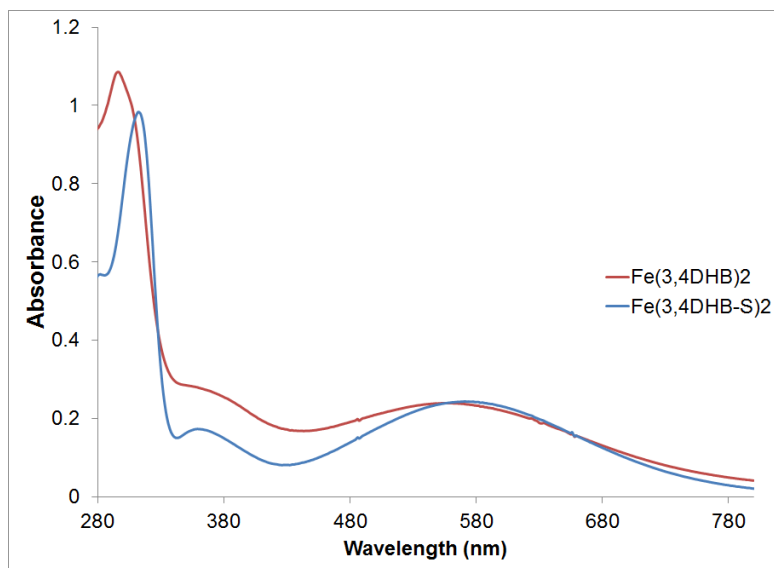


Figure A2.2. UV-visible spectra of $\text{Fe}(3,4\text{DHB})_2$ and $\text{Fe}(3,4\text{DHBS})_2$. The λ_{max} values differ by 20nm.

Chapter 3

Solution Thermodynamics, Structure and Transport of a Ferric Citrate Trimer in *Bacillus cereus*

Introduction

Citric acid is a low molecular weight organic acid and an important biomolecule needed to support the biochemistry of many living organisms. The conjugate base, citrate, is used in one of the main metabolic processes in aerobic organisms: the citric acid, or Krebs, cycle (1). Citrate is also a metal chelator that can be used in phytoremediation processes (2, 3) or as a metal complexing agent that is directly imported and used in an organism's biochemistry (4, 5). Citrate could be used as a carbon source while the metal may serve other purposes vital to the organism.

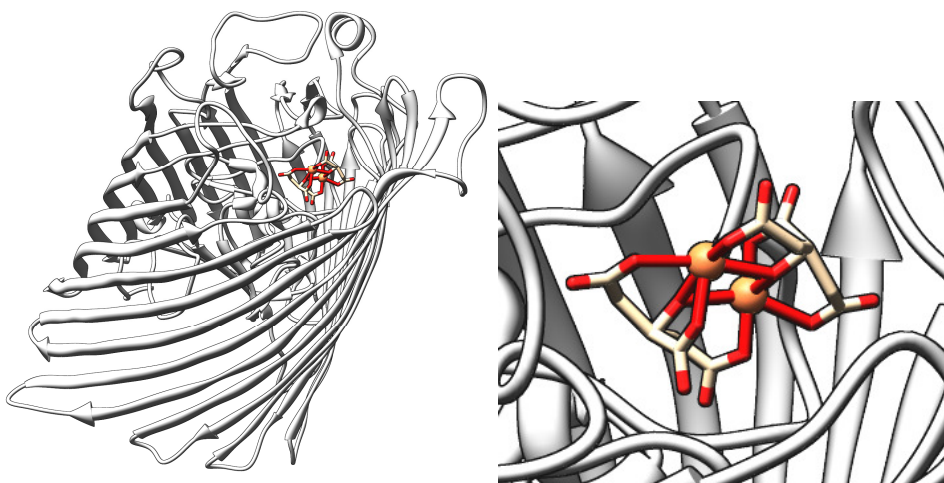


Figure 3.1. The ferric-citrate uptake protein, FecA (left) with Fe_2cit_2 in its binding pocket. A closeup of Fe_2cit_2 (right); coordinating protein residues are not shown for simplicity.

Although citrate is a relatively weak chelator of metals such as iron, almost all bacteria can utilize iron obtained by citrate. Additionally, the fact that citric acid is produced by host organisms and other environmental cohabitants makes it a readily available molecule for use by bacteria. The Gram-negative bacteria *E. coli* has an iron-citrate uptake system FecABCDE which has been well studied and described in the literature (6, 7). FecA is the outermembrane transporter that binds both diferric dicitrate (Fe_2cit_2) (Fig. 3.1) and iron-free dicitrate (7). This transport system is also utilized by other bacteria such as *Pseudomonas* (8). Gram-positive organisms such as *B. subtilis* and *Staphylococcus* also possesses iron-citrate uptake machinery such as YfmCDEF (9).

Recently, Fukushima et al. have identified ferric citrate uptake machinery in pathogenic *B. cereus* that is not similar to YfmCDEF in *B. subtilis* (10). A ^{55}Fe -citrate radiotracing experiment shows that the *B. cereus* strain ATCC 14579 takes up ferric citrate. The siderophore-binding protein of this system was isolated and named ferric citrate-binding protein C (FctC) after protein fluorescence quenching assays and nano ESI-MS analyses demonstrated the specificity of FctC for ferric citrate species (10) (Fig. 3.2). Specifically,

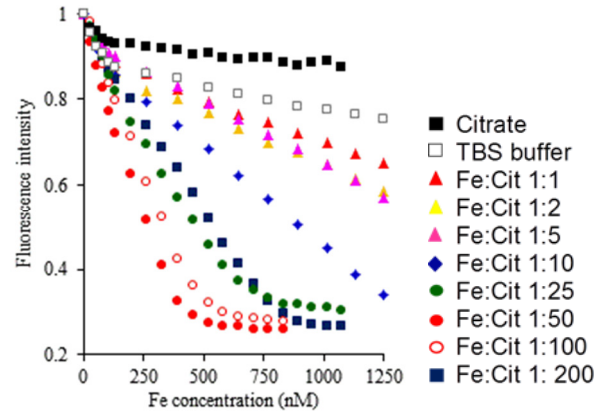


Figure 3.2. Fluorescence quenching assay of FctC with various ferric citrate solutions of different compositions.

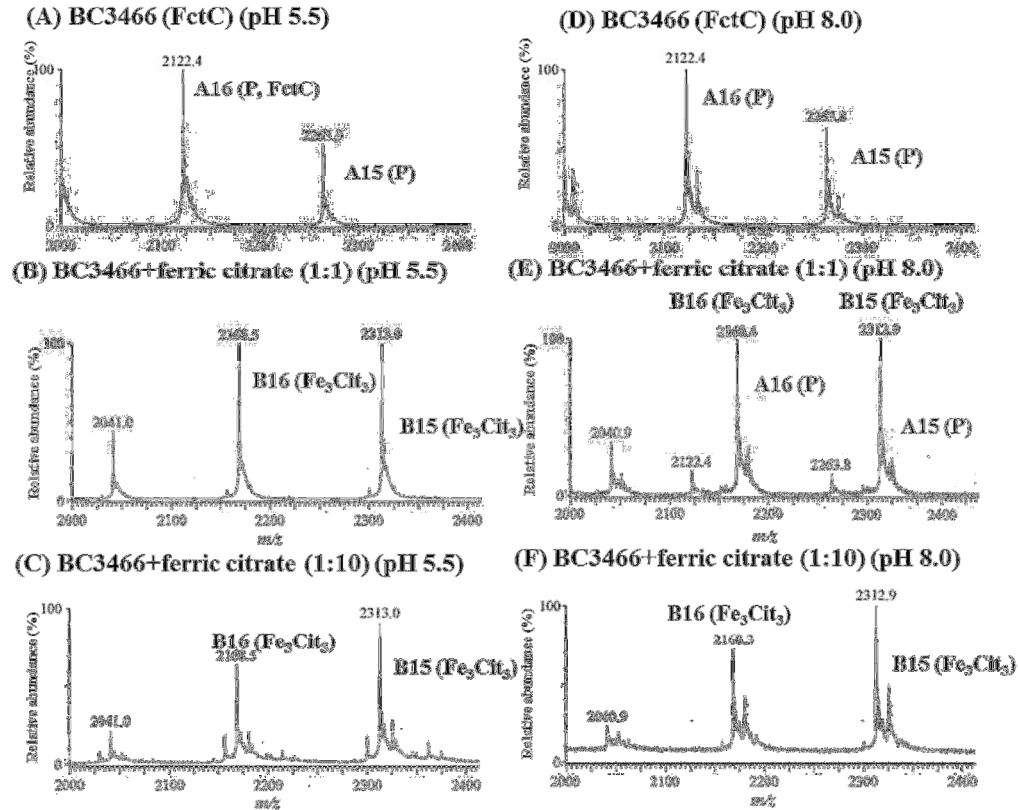


Figure 3.3. Nano ESI-MS results. Protein:ligand peaks were obtained in the +15 and +16 charge states. The theoretical mass of FctC is 34,676.5 Daltons. Variation of pH and Fe: citrate stoichiometry generated similar results: FctC shows selective binding for Fe_3cit_3 (right) and Fe_2cit_2 (not shown).

the nano ESI-MS results suggest that ferric citrate complexes of iron: citrate ratios 3:3 and 2:2 are compatible ligands that are bound with high affinity to FctC (Fig. 3.3).

Ferric citrate multimers such as a ferric citrate trimer (Fe_3cit_3) or Fe_2cit_2 do not exist in large amounts at physiological pH. This chapter investigates the ferric citrate species distribution under different conditions and the results highlight the remarkable selectivity of FctC. We also report theoretical structural investigations of the ferric citrate trimer, and calculate a more accurate protein ligand dissociation constant (K_d) to quantify the FctC: Fe_3cit_3 interaction.

Results

Speciation Diagrams of Ferric Citrate

Speciation diagrams were generated with Hyperquad Simulation and Speciation (HySS) (11). Stability constants ($\log \beta$) used for these calculations for MLH, ML_2 , ML_2H , ML_2H_2 , M_2L_2 and M_3L_3 were 24.84 (MLH), 32.73 (ML_2), 38.74 (ML_2H), 43.53 (ML_2H_2), 48.0 (M_2L_2), and 73.8 (M_3L_3) as described by Silva *et al* (12, 13). Citrate was treated as a tetrabasic ligand (LH_4) with pK_a values 3.13, 4.76, 6.40 and 14.4. Iron hydroxide formation constants were entered as -2.563 ($[\text{FeOH}]^{2+}$), -6.205 ($[\text{Fe}[\text{OH}]_2]^+$), -15.1 ($[\text{Fe}[\text{OH}]_3]$), -21.883 ($[\text{Fe}[\text{OH}]_4]^-$), -2.843 ($[\text{Fe}_2[\text{OH}]_2]^{4+}$) and -6.054 ($[\text{Fe}_3[\text{OH}]_4]^{5+}$).⁴⁶ Various stoichiometries of iron: citrate were used to calculate speciation, as indicated below each set of plots.

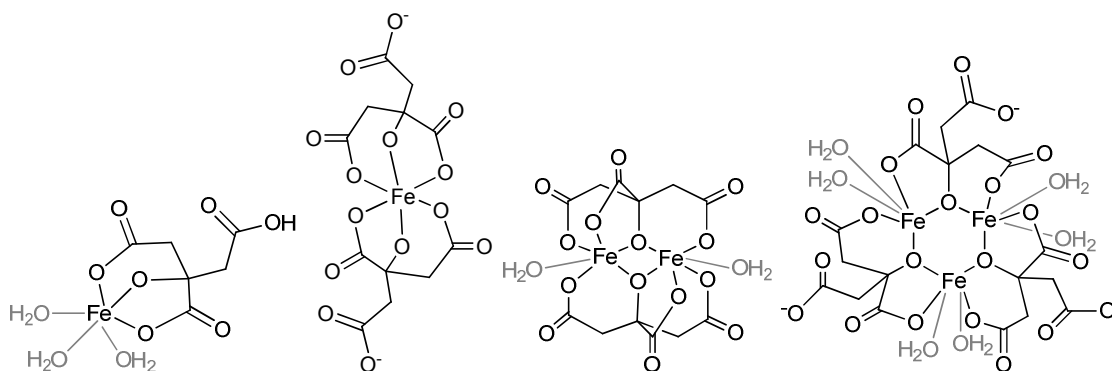


Figure 3.4. Various ferric citrate species in solution. Coordination sites are filled with water molecules where needed. All iron atoms are Fe^{III} . From left to right: Fecit, Fecit₂, Fe_2cit_2 , Fe_3cit_3 proposed by Silva *et al* (12).

The speciation diagrams in Figure 3.3 show the distribution of iron citrate complexes when the ratio of Fe: cit is 1:50 and 1:100. In both cases at physiological pH,

neither Fe_2cit_2 nor Fe_3cit_3 make up a large percentage of total iron citrate species in solution. Instead, Fecit_2 complexes are the majority of species in these solutions. Bond-line renderings of possible iron citrate species in solution are shown in Figure 3.4.

Speciation diagrams were also calculated for solutions in which the protein FctC was present, and concentrations were consistent with nano ESI-MS samples. At pH 7.4

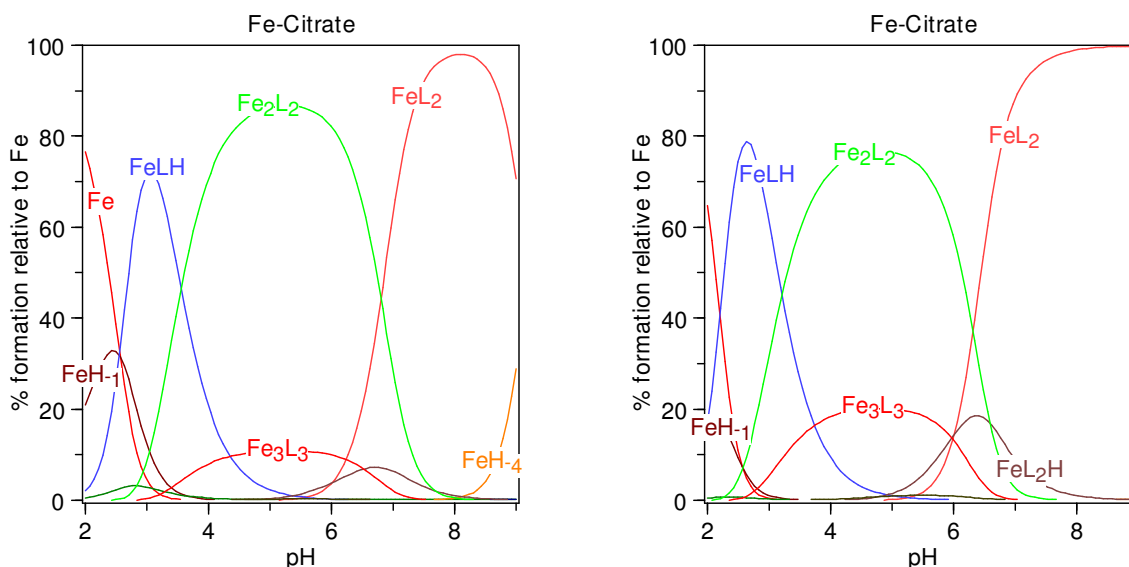


Figure 3.5. Speciation diagrams for ferric citrate solutions where $\text{FeCl}_3 = 4 \mu\text{M}$ and citrate = $200 \mu\text{M}$ (left, $\text{Fe: cit} = 1:50$) and $\text{FeCl}_3 = 20 \mu\text{M}$, citrate = $2000 \mu\text{M}$ (right, $\text{Fe: cit} = 1:100$). Formation constants for both Fe_2cit_2 and Fe_3cit_3 are considered in these diagrams. L refers to one molar equivalent of citrate, H_1 refers to one equivalent of hydroxide (OH).

when Fe: cit is 1:1, the dimer Fe_2cit_2 makes up slightly less than 70% of total species in solution. This percentage decreases to less than 30% when the Fe: cit ratio is changed to 1:10 (Fig. 3.5). The trimer Fe_3cit_3 constitutes about 30% of all iron citrate species in solution when Fe: cit is 1:1, but this percentage distribution decreases drastically to less than 10% at pH 7.4 when the citrate equivalents are increased ($\text{Fe: cit} = 1:10$) (Fig. 3.6).

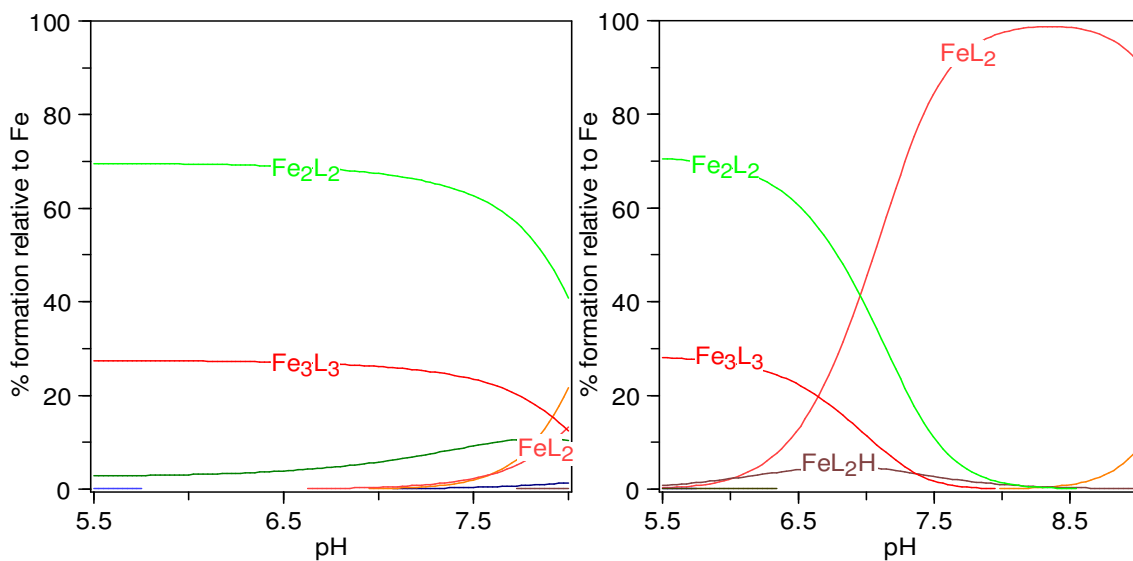


Figure 3.6. Speciation diagrams corresponding to solution conditions used in nano ESI-MS experiments. Left: Fe:cit is 1:1 (50 μM :50 μM), right: Fe:cit is 1:10 (50 μM : 500 μM).

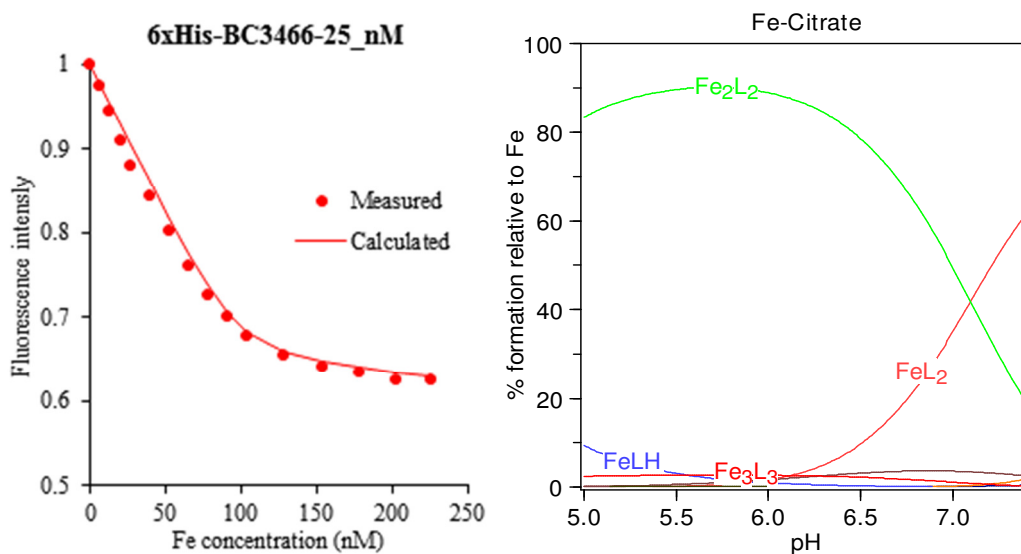


Figure 3.7. Fluorescence quenching assay corresponding to the quenching of FctC upon addition with a ferric citrate solution of Fe:cit 1:50 at pH 7.4 (left). Speciation diagram of ferric citrate (Fe:cit 1:50) solutions used in fluorescence quenching assay.

A speciation diagram was generated to accurately reflect the composition of a Fe: cit 1:50 solution. Specifically, the concentrations of iron and citrate were 0.226 μM Fe: 11.3 μM citrate that correspond to the end concentrations after fluorescence quenching assays (Fig. 3.7). Note that the species distribution of Fe_3cit_3 is well below 5% under these conditions.

K_d actual and upper limit calculations for the FctC: Fe_3cit_3 interaction

The K_d of FctC for ferric citrate determined by the fluorescence quenching assay was 2.60 nM (Fig. 3.7). This number was refined by the program Hyperquad (14) based on the change in fluorescence emission at 340 nm upon addition of ferric citrate solution (Fe: cit 1:50). Because the solution in the quenching experiment contains Fe_2Cit_2 and FeCit_2 as major species and Fe_3Cit_3 and $\text{Fe}(\text{HCit})$ as minor species (Fig. 3.7) and FctC can bind only Fe_2Cit_2 and Fe_3Cit_3 , the apparent K_d of the protein actually describes the protein affinity for both Fe_2Cit_2 and Fe_3Cit_3 . Thus the calculated K_d for this system represents an upper limit of the affinity that FctC has for all species in solution; because Fe_3Cit_3 is a minor species (less than 5% according to the speciation), the affinity of FctC for the substrate must be higher ($K_d < 2.60$ nM). Using the titration equivalence point (FctC–FexCitx complex: 150 nM) (Fig. 3.7), the calculated affinity of FctC for Fe_3Cit_3 is 0.267 nM.

A molecular scheme of Fe_3cit_3

While a structure for $\text{Fe}_3\text{citrate}_3\text{-oxo}$ has been modeled (15), we proposed a structure for Fe_3cit_3 ($\text{Fe}_3\text{C}_{18}\text{H}_{15}\text{O}_{21}$) evidenced by our nano ESI-MS results. Ideas for a structural starting point were inspired by a trialuminum tricitrate-hydroxo crystal structure (16) as well as both iron-citrate trimers in the literature to generate the Fe_3O_3 core (Fig. 3.8) (12, 15). Citrate ligands were then built around the Fe_3O_3 core using the Gaussian '09 package. The schematic structure was optimized in the Schrodinger Inc. graphical user interface Maestro. This model was initially minimized by a molecular mechanics approach (Schrodinger Inc. Macromodel package, OPLS 2005 force field, solvent model = water, Fe-OH₂ distances constrained to 2.7 Å) and was subject to minimization by density functional theory methods. However, a reasonable electronic structure could not be calculated, even from using various functionals (MO6-L and SDD) and basis sets (LANL2DZ, B3LYP). Therefore, our proposed structure remains a scheme, as the structure itself is hypothetical and excludes any optimization that accounts for the electronic structure of Fe_3cit_3 . Calculated bond angles of Fe-OH₂ are consistent with those found in Fe_2cit_2 found in the literature.

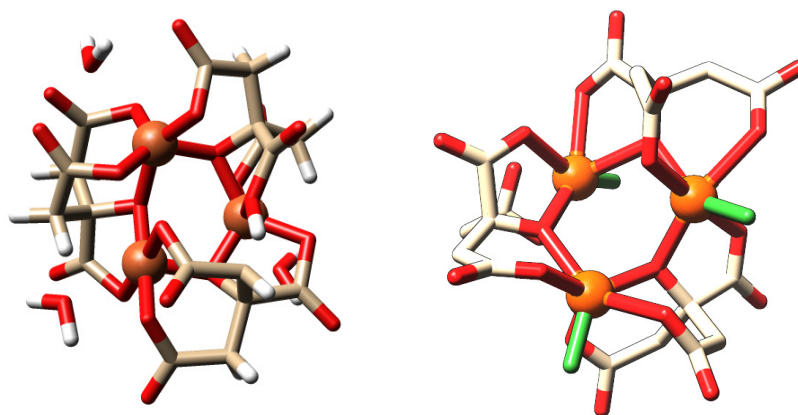


Figure 3.8. Molecular models of $\text{Fe}_3\text{cit}_3 \cdot 3\text{H}_2\text{O}$. Water ligands (left) could potentially be replaced by donor atoms from protein residues (green) within the FctC protein pocket (right). Red atoms = oxygens, orange spheres = Fe^{3+} , green rods represent basic protein residues from FctC.

Discussion

Fe_3cit_3 constitutes a low percentage of total iron citrate species under various conditions but is selected for by FctC

At pH 7.4, the predominant iron citrate species in solution, regardless of the presence of FctC and the ratio of Fe: citrate, is FeCit_2 . This result was determined by speciation calculations using the program HySS (11). Specifically, when the Fe: cit ratio is 1:10 (50:500 μM), FeCit_2 is the major iron citrate species in solution at pH 8.0-9.0. However, nano ESI-MS results at pH 8.0 and 9.0 clearly demonstrate that FctC does not bind FeCit_2 . Furthermore, FQ experiments of FctC, performed at pH 8.5, where FeCit_2 predominates in solution, show a significant decrease in fluorescence change upon addition of ferric citrate solution. This indicates that FeCit_2 does not bind FctC.

Ferric citrate solutions made to optimize the formation of FeCit were then tested for binding to FctC by similar methods. A complex of FctC and FeCit could not be detected by nano ESI-MS. Moreover, the FQ experiment at pH 3.5 showed that there is no suitable ferric citrate substrate for FctC under these conditions, even though speciation calculations indicate that the solution contains ferric monocation. Thus, FeCit is also not a compatible target for FctC.

Speciation diagrams show that the multimetric complexes Fe_2cit_2 and Fe_3cit_3 are not present in large amounts at physiological pH when the Fe: cit ratio is varied from 1:1, 1:10 to 1:50. In solutions independent of the siderophore binding protein FctC, Fe_3cit_3 makes up less than 5% of the total iron species in solution at pH 7.4. When the Fe: cit ratio is 1:10 (Fig.6), Fe_3cit_3 is less than 5%, compared to FeCit_2 (85%) and Fe_2cit_2 (10%).

Under these same conditions, FctC selectively binds Fe_3cit_3 and with an affinity that is strong enough to withstand the ionization methods of nano ESI-MS. It is clear that FctC selectively binds Fe_3Cit_3 , because the FctC: Fe_3Cit_3 complex was detected under all nano ESI-MS conditions tested (at pH 5.5, 6.9, 8.0, and 9.0 with ferric: citrate molar ratios of 1:1 and 1:10). Remarkably, FctC formed a complex with Fe_3Cit_3 at pH 5.5 with a ferric: citrate molar ratio of 1:1 and 1:10 (ferric: citrate = 50:50 μM and 50:500 μM , respectively) even though Fe_2Cit_2 is a major species. These results suggest that Fe_3Cit_3 is the preferred ferric citrate species for FctC compared with Fe_2Cit_2 and is an instance of a siderophore-binding protein selective for a multinuclear ferric complex such as Fe_3Cit_3 .

FctC can bind both ferric citrate complexes, Fe_2Cit_2 and Fe_3Cit_3 , but has a preference for Fe_3Cit_3 across a variety of conditions. Low citrate concentrations (10^{-6} – 10^{-9} M) are predicted to contain more Fe_2Cit_2 than Fe_3Cit_3 . The ability to bind both ferric citrate substrates, Fe_2Cit_2 and Fe_3Cit_3 , by FctC may confer an advantage to *B. cereus* as the bacterium must adjust to different environments where citrate concentrations are variable, and we suggest this aids the selectivity of iron.

The dissociation constant K_d for FctC: Fe_3cit_3 is the lowest of any siderophore-binding protein and ferric siderophore reported

Previously, Zawadzka et al. described that the K_d of FeuA for Fe-bacillibactin, FpuA for Fe-petrobactin, and FatB for Fe-petrobactin is 19, 175, and 127 nM, respectively (17). Moreover, the K_d of the other *B. cereus* siderophore-binding proteins, YxeB for Fe-desferrioxamine and YfiY for Fe-schizokinen, is 18 and 34 nM, respectively (17). Only the K_d of FatB for Fe-(3,4-dihydroxybenzoic acid)₂ has a similar value (1.2 nM) to the K_d of FctC for ferric citrate ($K_d < 2.7$ nM). The subnanomolar K_d of the FctC ferric citrate system indicates that FctC strongly binds multinuclear ferric citrate (Fe_2Cit_2 and Fe_3Cit_3). The calculated affinity of FctC for Fe_3Cit_3 , 0.267 nM, is one of the lowest dissociation constants determined for a siderophore-binding protein and a ferric-siderophore complex.

The molecular scheme for Fe_3cit_3 involves direct coordination by protein residues

Exclusive of solutions with siderophore binding proteins present, some evidence for ferric citrate multimers exist. A nonairon citrate “triple decker” complex was synthesized and characterized by X-ray diffraction (18). An iron-citrate trimer oxo has been isolated from plant xylem sap and is implicated in long distance iron transport in plants (15). Mass spectrometry experiments of iron citrate solutions, also independent of siderophore binding proteins, show evidence for an iron citrate trimer, but the authors propose a structure with dangling, deprotonated carboxylate arms (Figure 3.4).

In our structure for a ferric citrate trimer, we propose that all hard oxygens are coordinated to the ferric iron centers, and that water molecules are displaced by basic protein residues once the complex is bound within the ligand binding domain. Direct coordination by protein residues has been reported in other cases, for example in the FecA: Fe_2cit_2 system (7). There is no current crystallographic evidence to support our

structure, so at this point the purported structure in Fig. 3.8 remains a scheme based on theoretical calculations.

Comparing Fe_3cit_3 with an aluminum-citrate trimer

An aluminum-citrate trimer is known, yet this structure differs from ours in that it has a bridging hydroxyl moiety between two aluminum centers (Fig. 3.9) (16). We have rendered a three-dimensional model based on the crystallographic information obtained from Feng et al. (Fig. 3.9). One water molecule fills the empty coordination shell of an aluminum center.

Speciation diagrams for the aluminum citrate trimer were generated based on known complexation constants. When the stoichiometric ratio of Al:cit is 1:1 (50 μ M:50

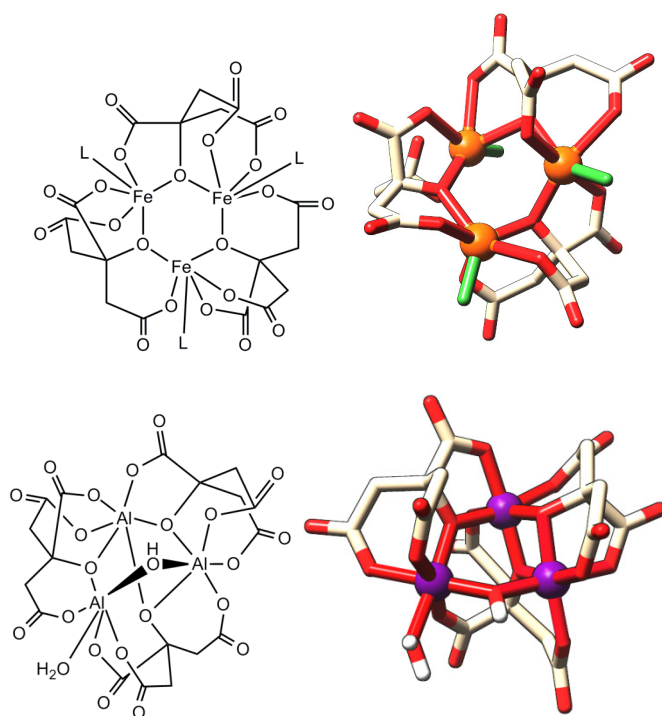


Figure 3.9. Ferric citrate trimer (top) and aluminum citrate trimer (bottom). Left: bond-line structure; right, 3D rendering of structure.

μ M), the concentration of trimer is higher than when Al:cit is 1:10 (50 μ M: 500 μ M) (Figure 3.8). However, unlike the iron citrate trimer, the aluminum citrate trimer is much more predominant from pH 4.5-9.0 and constitutes 100% of all species from pH 5.9 onward (when Al:cit is 1:1).

An increase in the concentration of citrate at micromolar concentrations diminishes the percentage distribution of aluminum citrate trimer. This effect is also seen

in the iron citrate speciation plots, however, the iron citrate trimer exists at pH 7.4 whereas the aluminum citrate trimer does not.

The existence of an aluminum citrate trimer in aqueous solutions served as our initial structural basis for our proposed iron citrate complex. The central 6-membered ring consisting of alternating Al and O atoms was also seen in the crystallographically evidenced iron-citrate multimers reported in the literature (18). A comparison of aluminum citrate and iron citrate speciation diagrams shows that the aluminum citrate trimer composes 100% of the solution over pH 5.9 when Al: cit is 1:1 at micromolar concentrations, whereas the iron citrate trimer never constitutes more than 25% under any conditions reported here.

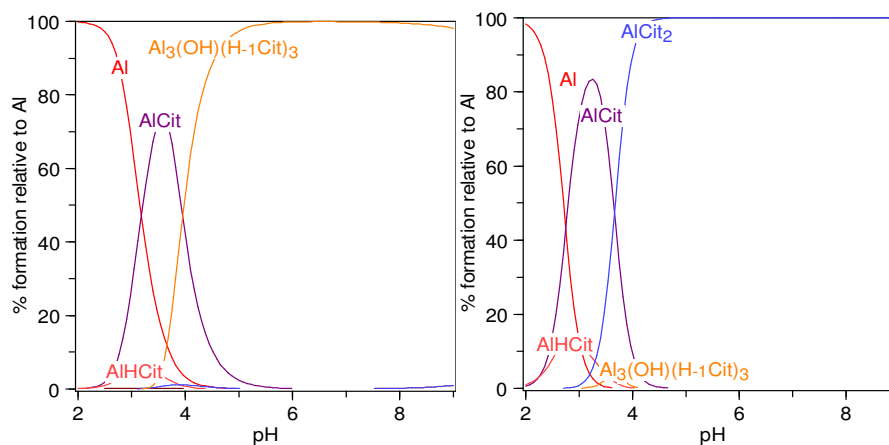


Figure 3.10. Speciation diagrams of aluminum citrate compounds in solution. Aluminum citrate species form depending on pH and stoichiometric ratio of metal to ligand. Left: Al: cit is 1:1 (50 μ M:50 μ M). Right: Al: cit is 1:10 (50 μ M: 500 μ M).

Conclusion

Both citrate and ferric iron are necessary nutrients for bacteria such as *B. cereus*. Citrate can chelate metal ions and such complexes can be imported through specific uptake pathways. Ferric citrate uptake machinery was identified and isolated by Fukushima et al (10). The identity of the iron citrate complex bound by the ferric citrate binding protein FctC was a trimer, Fe_3cit_3 as evidenced by nano ESI-MS experiments. The nano ESI-MS results consistently showed the formation of the ternary $\text{FctC}:\text{Fe}^{\text{III}}:\text{citrate}$ complex across a variety of pHs and ratios of Fe: cit. The iron citrate species that are bound by FctC are both Fe_3cit_3 and Fe_2cit_2 . The affinity of FctC for ferric citrate was determined by fluorescence quenching assays and subsequent nonlinear regression analyses that generated a protein-ligand dissociation constant (K_d). In actuality, the empirical K_d of 2.60 nM is an effective upper limit for the $\text{FctC}:\text{Fe}_3\text{cit}_3$

interaction. Thus a more accurate K_d was determined to be 0.267 nM for FctC:Fe₃cit₃ by taking into account the percent distribution of Fe₃cit₃ under the conditions used in the fluorescence quenching assay. This calculated K_d is one of the lowest reported for a siderophore-binding protein and a given iron-containing ligand.

We also built a theoretical model for Fe₃cit₃ based on crystal structures of similar metal-citrate complexes in the literature, including an aluminum citrate trimer. Unlike the two other instances in which an iron citrate trimer is implicated, we propose that all hard oxygens are coordinated to the Fe^{III} centers, and that the coordination shells of each iron center are filled with either water or protein residues.

The remarkable ability of FctC to fish out the iron citrate trimer, a species of low distribution, was consistent across some changes in pH and variation in the molar ratio of Fe:cit. The *B. cereus* bacteria may encounter various environments in which the pH and concentrations of iron and citrate are not optimal. Perhaps the binding of the iron citrate trimer is advantageous to the bacterium for reasons not proposed or supported by the data here. The FctC selectivity could be part of *B. cereus*' recognition mechanism for iron citrate and could potentially be the discriminatory site in which other metal-citrate species in the surrounding environment are not bound and consequently not imported.

Experimental

General. All chemicals were obtained from commercial suppliers and used without further purification unless otherwise noted. Nano ESI-mass spectrometry experiments were performed by the QB3/Chemistry Mass Spectrometry Facility in B207 Stanley Hall, UC Berkeley. Iron chloride stock solutions in 1 M HCl were standardized by EDTA titration according to the methods of Welcher (19). Tris(hydroxymethyl)aminomethane (Tris) buffered saline solutions were made according to routine protocols.

Fluorescence quenching binding assay. Fluorescence quenching of FctC was measured on a Cary Eclipse fluorescence spectrophotometer. A 5 nm slit band pass for excitation and a 10 nm slit band pass for emission was used with a high voltage detector (PMT = 900V). An excitation wavelength of $\lambda_{exc} = 280$ nm was used and emission was collected at $\lambda_{em} = 320$ nm to 340 nm. Measurements were made at a protein concentration of 100 nM in buffered aqueous solutions, plus 32 μ g/mL ubiquitin (Sigma) and 5% DMSO. Fluorescence intensities were corrected for dilution due to addition of ligand. Fluorescence data were analyzed by a nonlinear regression analysis of the normalized fluorescence response versus ligand concentration using Hyperquad (14) which allows for a multiwavelength treatment of the data and simultaneously refines all titrations. Dissociation constants were determined from at least three independent titrations.

Ligand solutions preparation. Ligand and ferric-ligand solutions were prepared *in situ*. An aliquot of a DMSO stock solution of the free ligand (12 mM, 25 μ L) and FeCl₃ salt (27 mM, 3.7 μ L, 0.33 equiv) were combined, vigorously shaken, and diluted with TBS buffer (pH 7.2) to form the metal complexes at a concentration of 0.1 mM (no metal

added for apo-ligands). The solutions were vigorously shaken, equilibrated for 1.5 hr and diluted to a final concentration of 20 μM in 5% DMSO/TBS buffer.

Speciation plots Speciation Diagram of Ferric Citrate. Speciation diagrams were generated with Hyperquad Simulation and Speciation (HySS) (29). Stability constants ($\log \beta$) used for these calculations for MLH, ML_2 , ML_2H , ML_2H_2 , M_2L_2 and M_3L_3 were 24.84 (MLH), 32.73 (ML_2), 38.74 (ML_2H), 43.53 (ML_2H_2), 48.0 (M_2L_2), and 73.8 (M_3L_3) as described by Silva et al. (16). Citrate was treated as a tetrabasic ligand (LH_4) with pK_a values 3.13, 4.76, 6.40 (36), and 14.4 (37). Iron hydroxide formation constants were entered as -2.563 ($[\text{FeOH}]^{2+}$), -6.205 ($[\text{Fe}(\text{OH})_2]^+$), -15.1 ($\text{Fe}(\text{OH})_3$), -21.883 ($[\text{Fe}(\text{OH})_4]^-$), -2.843 ($[\text{Fe}_2(\text{OH})_2]^{4+}$) and -6.054 ($\text{Fe}_3(\text{OH})_4^{5+}$) (16, 38). The concentrations of Fe(III) and citrate utilized for generating the speciation diagrams were 0.226 μM and 11.3 μM (Fe:citrate = 1:50), 1.25 μM and 62.5 μM (Fe:citrate = 1:50), 1.25 μM and 125 μM (Fe:citrate = 1:100), 1.25 μM and 250 μM (Fe:citrate = 1:200), 50 μM and 50 μM (Fe:citrate = 1:1), 50 μM and 500 μM (Fe:citrate = 1:10), and 0.1 μM and 50 μM (Fe:citrate = 1:500).

Triferric Tricitrate Structural Modeling. Fe_3Cit_3 was constructed using the Gaussian '09 package. We then employed the Schrodinger Inc. graphical user interface Maestro. The MacroModel package was used to minimize the structure using the OPLS_2005 force field, water as a solvent, and with constraints on the Fe-OH₂ distances (2.7 Å). Calculated bond angles of Fe-OH₂ are consistent with those found in Fe_2Cit_2 . The molecular mechanics (MM) structure was subject to minimization by density functional theory (DFT) methods. A sensible electronic structure could not be calculated by DFT, even from using various functionals (MO6-L and SDD) and basis sets (LANL2DZ, B3LYP), so the MM minimized structure was used as a suitable schematic model of Fe_3Cit_3 . Calculated bond angles and lengths are reported in Appendix 3.

References

1. Voet D (2011) *Biochemistry* (John Wiley & Sons, Hoboken, NJ)4th ed.
2. Chen Y. et al. (2003) The role of citric acid on the phytoremediation of heavy metal contaminated soil. *Chemosphere* 50:807–811.
3. Turgut C, Katie Pepe M, Cutright TJ (2004) The effect of EDTA and citric acid on phytoremediation of Cd, Cr, and Ni from soil using *Helianthus annuus*. *Environmental Pollution* 131:147–154.
4. Mancusso R, Gregorio GG, Liu Q, Wang D-N (2012) Structure and mechanism of a bacterial sodium-dependent dicarboxylate transporter. *Nature* 491:622–626.
5. Willecke K, Gries E-M, Oehr P (1973) Coupled Transport of Citrate and Magnesium in *Bacillus subtilis*. *J Biol Chem* 248:807–814.
6. Wagegg W, Braun V (1981) Ferric citrate transport in *Escherichia coli* requires outer membrane receptor protein *fecA*. *J Bacteriol* 145:156–163.
7. Yue WW, Grizot S, Buchanan SK (2003) Structural Evidence for Iron-free Citrate and Ferric Citrate Binding to the TonB-dependent Outer Membrane Transporter *FecA*. *Journal of Molecular Biology* 332:353–368.
8. Marshall B, Stintzi A, Gilmour C, Meyer J-M, Poole K (2009) Citrate-mediated iron uptake in *Pseudomonas aeruginosa*: involvement of the citrate-inducible *FecA* receptor and the *FeoB* ferrous iron transporter. *Microbiology (Reading, Engl)* 155:305–315.
9. Ollinger J, Song K-B, Antelmann H, Hecker M, Helmann JD (2006) Role of the *Fur* Regulon in Iron Transport in *Bacillus subtilis*. *J Bacteriol* 188:3664–3673.
10. Fukushima T et al. (2012) *Bacillus cereus* iron uptake protein fishes out an unstable ferric citrate trimer. *PNAS*. Available at: <http://www.pnas.org/content/early/2012/09/26/1210131109> [Accessed February 21, 2013].
11. Alderighi L. et al. (1999) Hyperquad simulation and speciation (HySS): a utility program for the investigation of equilibria involving soluble and partially soluble species. *Coordination Chemistry Reviews* 184:311–318.
12. Silva AMN, Kong X, Parkin MC, Cammack R, Hider RC (2009) Iron(III) citrate speciation in aqueous solution. *Dalton Trans*:8616–8625.
13. Silva AMN, Kong X, Hider RC (2009) Determination of the pK_a value of the hydroxyl group in the alpha-hydroxycarboxylates citrate, malate and lactate by ¹³C

NMR: implications for metal coordination in biological systems. *Biometals* 22:771–778.

14. Gans, Peter, Sabatini, Antonio, Vacca, Alberto (1996) Investigation of equilibria in solution. Determination of equilibrium constants with the HYPERQUAD suite of programs. *Talanta* 43:1739–1753.
15. Rellán-Alvarez R et al. (2010) Identification of a tri-iron(III), tri-citrate complex in the xylem sap of iron-deficient tomato resupplied with iron: new insights into plant iron long-distance transport. *Plant Cell Physiol* 51:91–102.
16. Feng TL, Gurian PL, Healy MD, Barron AR (1990) Aluminum citrate: isolation and structural characterization of a stable trinuclear complex. *Inorg Chem* 29:408–411.
17. Zawadzka AM, Abergel RJ, Nichiporuk R, Andersen UN, Raymond KN (2009) Siderophore-Mediated Iron Acquisition Systems in *Bacillus cereus*: Identification of Receptors for Anthrax Virulence-Associated Petrobactin[†],[‡]. *Biochemistry* 48:3645–3657.
18. Bino A, Shweky I, Cohen S, Bauminger ER, Lippard SJ (1998) A Novel Nonairon(III) Citrate Complex: A “Ferric Triple-Decker.” *Inorg Chem* 37:5168–5172.
19. Welcher FJ (1958) *The analytical uses of ethylenediaminetetraacetic acid* (Van Nostrand).

Chapter 3 Appendix

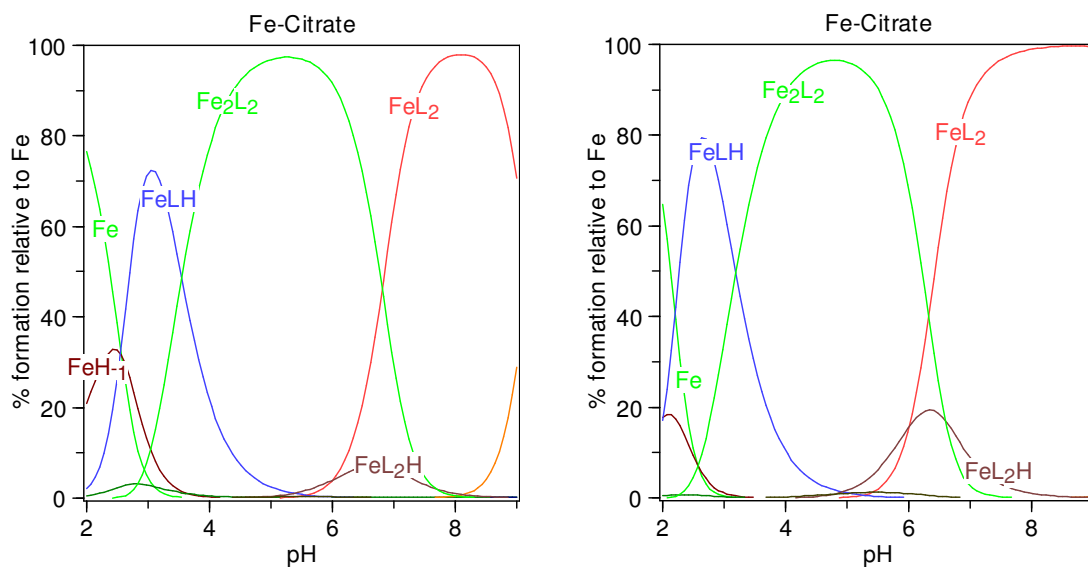


Figure A3.1. Iron-citrate speciation diagrams using multi-iron complex formation constants for only M_2L_2 . Relevant concentrations are: $FeCl_3 = 4 \mu M$, Citrate = $200 \mu M$ (left) and $FeCl_3 = 20 \mu M$, Citrate = $2000 \mu M$ (right).

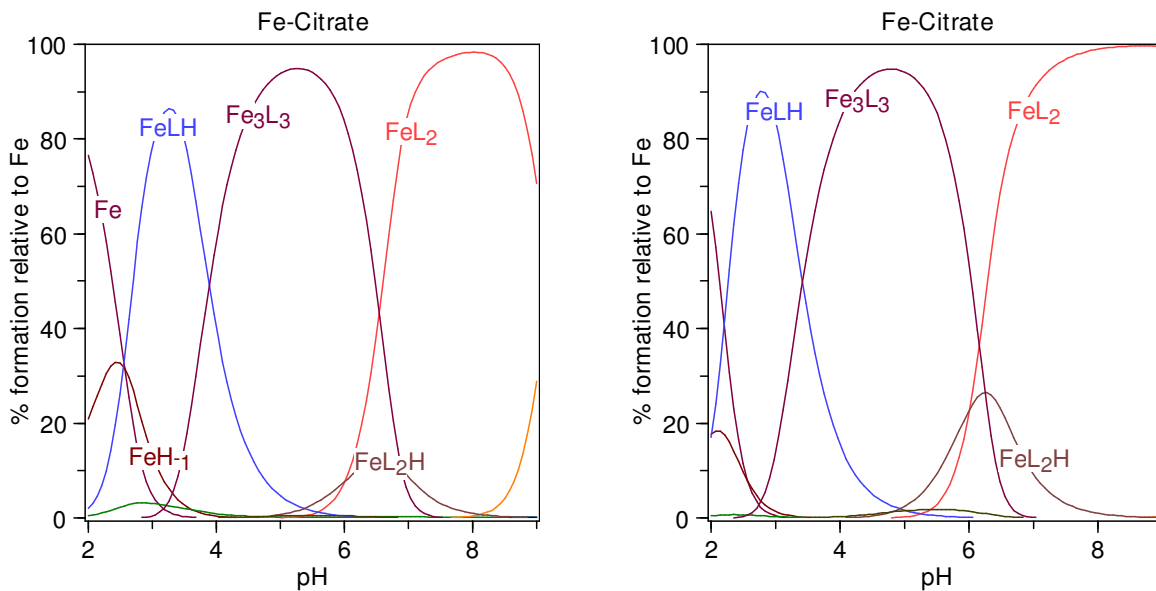
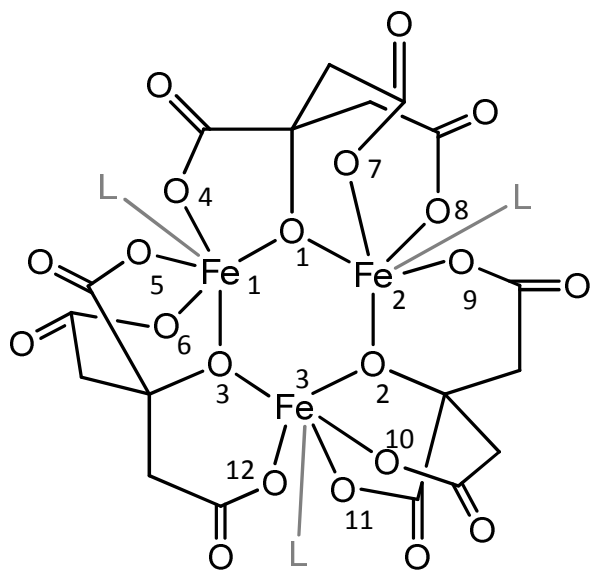


Figure A3.2. Iron-citrate speciation diagrams using multi-iron complex formation constants for only M_3L_3 . Relevant concentrations are: $FeCl_3 = 4 \mu M$, Citrate = $200 \mu M$ (left) and $FeCl_3 = 20 \mu M$, Citrate = $2000 \mu M$ (right).

Table A3.1. Calculated bond distances and angles for Fe₃cit₃.



Atoms	Calculated bond distance (Å)	Atoms	Calculated bond angle (°)
Fe1-O1	2.20	Fe1-O1-Fe2	121.04
Fe1-O4	2.30	O1-Fe2-O2	109.99
Fe1-O5	2.25	Fe2-O2-Fe3	108.15
Fe1-O6	2.36	O2-Fe3-O3	97.84
Fe1-O3	2.25	Fe3-O3-Fe1	109.58
Fe2-O1	2.27	O3-Fe1-O1	90.04
Fe2-O7	2.35	O4-Fe1-O3	142.07
Fe2-O8	1.94	O4-Fe1-O1	48.02
Fe2-O9	2.38	O4-Fe1-O5	133.94
Fe2-O2	2.34	O4-Fe1-O6	90.05
Fe3-O2	2.22	O7-Fe2-O1	66.34
Fe3-O10	2.24	O7-Fe2-O2	94.75
Fe3-O11	2.40	O7-Fe2-O8	79.26
Fe3-O12	2.28	O7-Fe2-O9	75.05
Fe3-O3	2.19	O10-Fe3-O2	83.52
		O10-Fe3-O11	89.82
		O10-Fe3-O12	176.85
		O10-Fe3-O3	113.55

Chapter 4

Structure and Function of Poly- γ -(D)-glutamic Acid Capsule, a *B. anthracis* Virulence Factor and Potential Siderophore

Introduction

The etiologic agent of the anthrax infection is the Gram-positive bacterium *B. anthracis*. Anthrax infections in human are rare compared to infections caused by more commonly encountered bacteria such as *Escherichia coli* or *Streptococcus pyogenes*. Although anthrax infections are rare, untreated anthrax infections are lethal (1). A limited number of effective treatments exist for anthrax infections exist. Interest in studying the anthrax pathogen has increased due to the potential use of anthrax spores in biological weaponry (2, 3).

Anthrax can be contracted by humans cutaneously, gastrointestinally or inhalationally (1). In all cases, the inoculation of *B. anthracis* spores occurs after spores enter the host and are phagocytosed by resident macrophages (4). Spore germination occurs intracellularly and *B. anthracis* then becomes metabolically active and replicates. At this stage the bacterium expresses virulence factors and subverts immune activity.

It is proposed that *B. anthracis* requires iron at every stage of its infection cycle (5). Soon after the intracellular germination described above, *B. anthracis* siderophores bacillibactin and petrobactin are expressed. Petrobactin is expressed first and is crucial for immunoevasion and survival of the bacterium in the early stages of germination (6, 7). Iron sequestration and delivery by petrobactin then supports the outgrowth and replication of vegetative cells. Bacillibactin biosynthesis and secretion are thought to be important later on in the infection cycle of *B. anthracis* (6).

After the transformation of a germinated spore to a vegetative cell, the bacterium engages in other routes of iron acquisition such as the expression of heme protein receptors to further support growth and replication (5). The vegetative cells of *B.*

anthracis replicate within white blood cells and macrophages. It is also at this stage and onward that anthrax toxins are produced and secreted (8, 9). Eventually *B. anthracis* cells

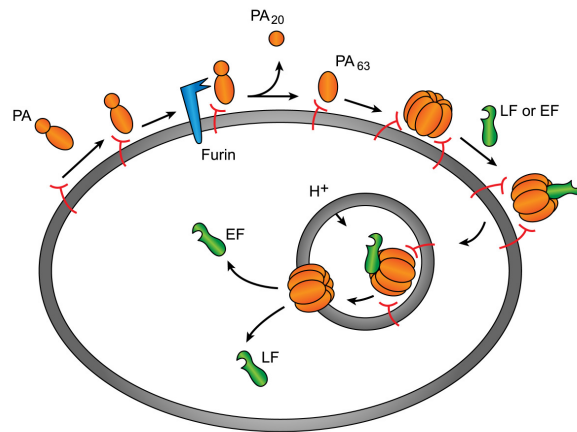


Figure 4.1. Anthrax toxin assembly.

pervade the lymph system of its mammalian host, where toxins are constantly produced and spreadwide, eventually leading to host death.

The anthrax exotoxins, edema toxin and lethal toxin, are each AB-type proteins that are composed by a combination of edema factor (EF) or lethal factor (LF) with protective antigen (PA). Toxin self assembly occurs after monomeric PA has docked onto one of two known cell receptors (ANTXR) (10, 11) and is cleaved by a furin-type protease. The proteolytically active form of PA is referred to in the literature as $_n$ PA. A 20 kDa portion of $_n$ PA (PA₂₀) dissociates and the remaining PA portion (PA₆₃) remains receptor bound and oligomerizes into ring-shaped heptamers (12–16) or octamers (17). Both EF and LF can be recruited and docked to the PA channel to form edema toxin and lethal toxin, respectively. The toxins are endocytosed (18), and acidic conditions of the endosome initiate the insertion of PA₆₃ into the membrane (19, 20). PA₆₃, now a translocase channel, facilitates the translocation of EF and LF into the cytosol where these factors catalyze reactions which disrupt normal metabolic activity of the host (13, 21).

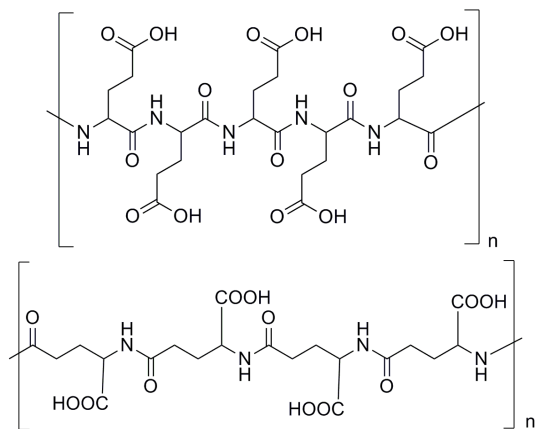


Figure 4.2. Bond-line drawings of poly-(α)-glutamic acid (top) and *B. anthracis*' poly-γ-(D)-glutamic acid capsule (bottom).

In addition to anthrax toxins, *B. anthracis* possesses another virulence factor: the poly-γ-(D)-glutamic acid capsule (PGA) (Fig. 4.2) (22). The glutamic acid monomers are linked at the γ carbons, as opposed to the α carbons. Furthermore, different *Bacillus* species may secrete polyglutamic acid capsules that vary in stereoisomer composition (D or L). *Bacillus anthracis* secretes the 100% D polymer, whereas the related *Bacillus licheniformis* secretes 0.8D:0.2L polymer. In the innocuous soil pathogen *B. subtilis*, PGA is composed of both D and L isomers (23, 24). The all-D configuration of the *B. anthracis* capsule confers resistance to destructive enzymes it may encounter in its life cycle. In the

anthrax pathogen life cycle, capsule formation occurs soon after spore germination (4). Similar to other bacterial capsules, PGA enhances virulence by protecting *B. anthracis* from phagocytosis.

In collaboration with Prof. Bryan Krantz at UC Berkeley, we have found that PGA contains iron as well as other metals such as manganese, and that iron-containing PGA, or holo PGA, inactivates anthrax toxins. This chapter highlights recent inquiries and advances that expose alternative roles for PGA, holo PGA and exotoxins. First, we investigated whether PGA was a putative iron-delivery agent that delivered iron to PA and whether holo PGA was inhibiting PA by a binding event. Secondly, we sought to measure whether PGA was strong enough to remove iron from human transferrin and if so, to measure the rate of this process. Lastly, we were interested in probing the structure of holo PGA to investigate how iron affects the overall structure of PGA.

Results

PA-siderophore interactions

Holo PGA inhibition of PA and, subsequently, anthrax toxins is dependent on PGA length and also percentage of D to L glutamic acid subunits. To elucidate the structural mechanism of PA (and ultimately toxin) inhibition by holo PGA, we asked whether other iron chelators such as ferric siderophores could deliver iron to PA. PA has inherent fluorescence that could be quenched in the event of specific binding. Fluorescence quenching assays with enterobactin, petrobactin, and the corresponding ferric complexes were performed in TBS buffer at 25 °C (Fig. 4.3). Since petrobactin is a siderophore secreted from the *Bacillus cereus* group of bacteria, we also tested ferric petrobactin photoproduct, the photolyzed ferric petrobactin complex (not shown in Fig. 4.3). Both apo and ferric siderophores were freshly prepared in situ and used within 24 hours. We found that neither apo nor ferric siderophores quenched PA fluorescence. The 15% decrease in fluorescence is similar across all experiments, including the natural PA fluorescence decrease due to photobleaching. The percent fluorescence quenching for both apo and ferric siderophores was similar and suggested a nonspecific binding interaction with little PA quenching overall.

Activity assays that measured holo PGA inhibition of PA-toxins were performed in the Krantz lab. Addition of apo siderophores to holo PGA-PA mixtures showed that siderophores could compete with the iron in holo PGA, thus slowing toxin inhibition.

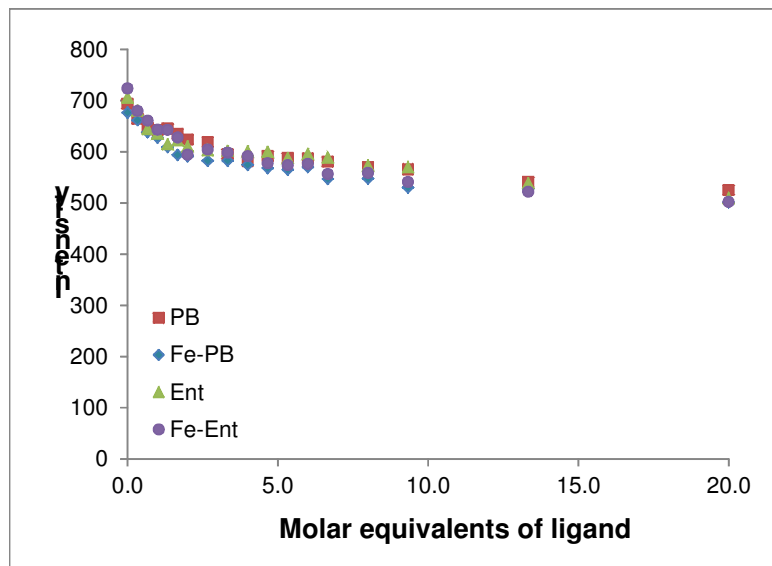


Figure 4.3. Fluorescence quenching plot of PA versus added apo- or ferric-siderophores. PB = petrobactin, Ent = enterobactin. The results of PB photoproduct are not shown but have similar results to PB and Ent.

Structural investigations of Fe-PGA

Since holo PGA was responsible for toxin inhibition, we were interested in probing the structural effect of iron on apo PGA. The average PGA molecular weight for our studies was 150 kDa and had an average of 5-7 Fe atoms per polymer, as determined by ICP-AES. The spectroscopic method we resorted to for such a system was extended x-ray absorption fine structure spectroscopy (EXAFS) as well as some X-ray absorption near-edge spectroscopy (XANES) in collaboration with Dr. Tsuyoshi Yaita and his team at the Japan Atomic Energy Agency. Four samples were expressed and collected from *B. licheniformis*. Sample 1 was the native L/D PGA, sample 2 was the all-D PGA (DPGA) polymer, sample 3 was the all-D iron stripped and supplemented with FeCl_3 , and sample 4 was all-D iron stripped sample. All samples were expressed according to previously reported methods from Kintzer (25), shipped in dry ice and were kept in a -80 degrees Celsius freezer and thawed right before use. The first set of samples were provided by Dr. Kintzer, and a second set of samples were expressed and purified in the Raymond lab according to Kintzer's protocol.

Synchrotron radiation experts Dr. Tsuyoshi Yaita and his group collected iron pre-edge data (XANES) for samples 1-3 at 200K and 298K at the SPring8 national laboratory in Hyogo prefecture, Japan. Interestingly, at the lower temperature, the DPGA sample (sample 2) shows a sharp peak at 7.113 keV (Fig. 4.4). This effect is less evident with samples 1 and 3, perhaps suggesting that sample 2 has a slightly different environment around the iron centers when the DPGA polymer is the chelator.

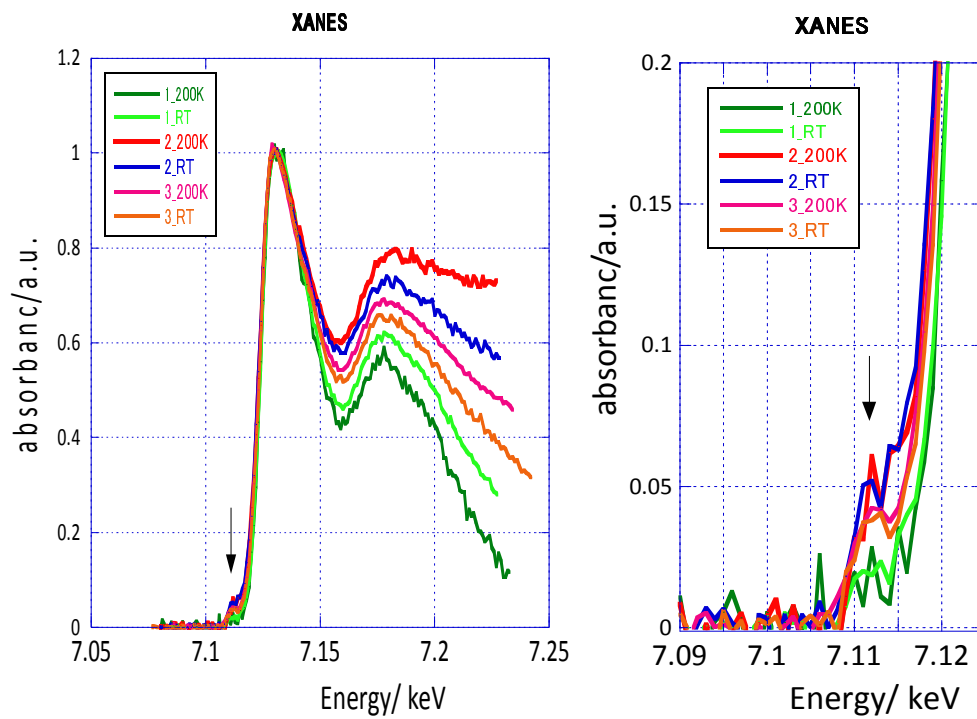
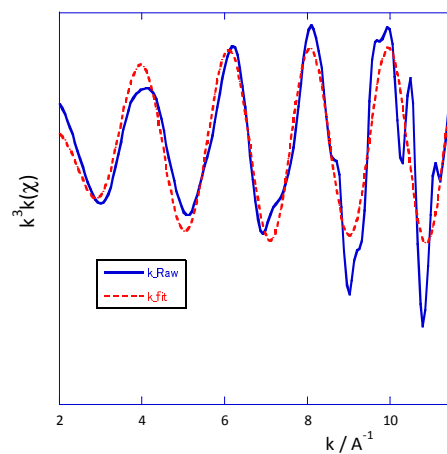
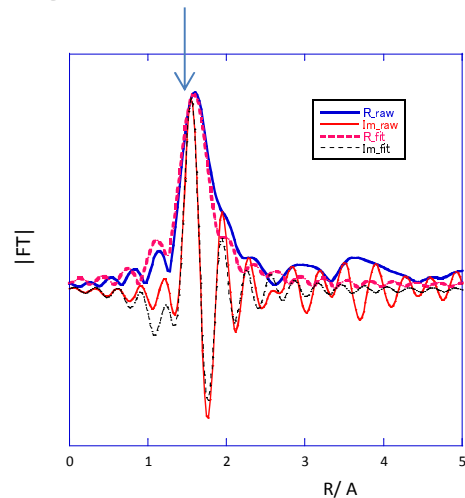


Figure 4.4. Pre-edge data for all capsule samples sent to Dr. Tsuyoshi Yaita (left). A zoomed in version of the XANES data is on the right. Legend: sample number_temperature in Kelvin. RT = 293.15K.

Dr. Yaita and his group collected raw EXAFS measurements of PGA samples. The Fourier transforms for samples 1-4 are shown in Figures 4.5 to 4.8 for samples measured at both 200K and 298K. Solid blue lines are the raw data, and dashed red lines are fitted lines. For samples 1-3, the immediate coordination around the iron was modeled after iron-citrate samples because of available crystal structures that served as iron-carboxylate models for bond angles and lengths.

In sample 1, data at both 200K and 298K overlap well with fitted data based on iron-citrate (Fig. 4.5). For sample 2, the fit at 200K is not a statistically good fit, and this fit gets worse with lower temperature (Fig. 4.6). The iron-supplemented sample (3) data fits well with ferric citrate as a model at both experimental temperatures (Fig. 4.7). Data for sample 4 was collected at one temperature only (200K) for purposes of collecting a background spectrum. However, some iron in the sample is evident (Fig. 4.8). Further investigation of sample 4 is required, including a repeat experiment in which all possible sources of iron contamination are eliminated from sample preparation.

#1@RT O



#1@200K O

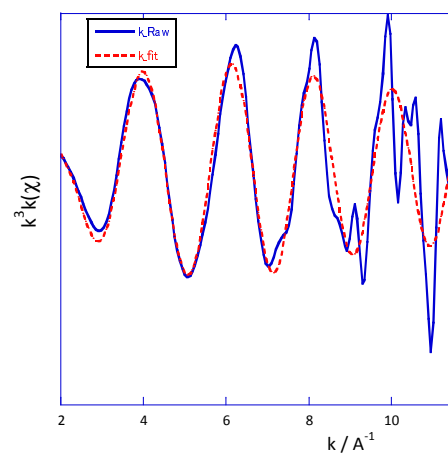
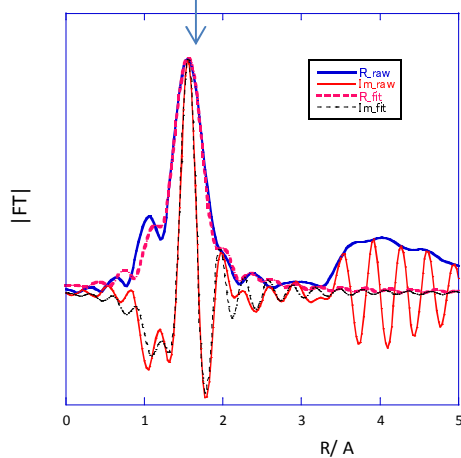


Figure 4.5. EXAFS (left) and Fourier transform (right) of native LDPGA capsule from *B. licheniformis*. Blue solid lines are raw data, red dashed lines are fitted lines.

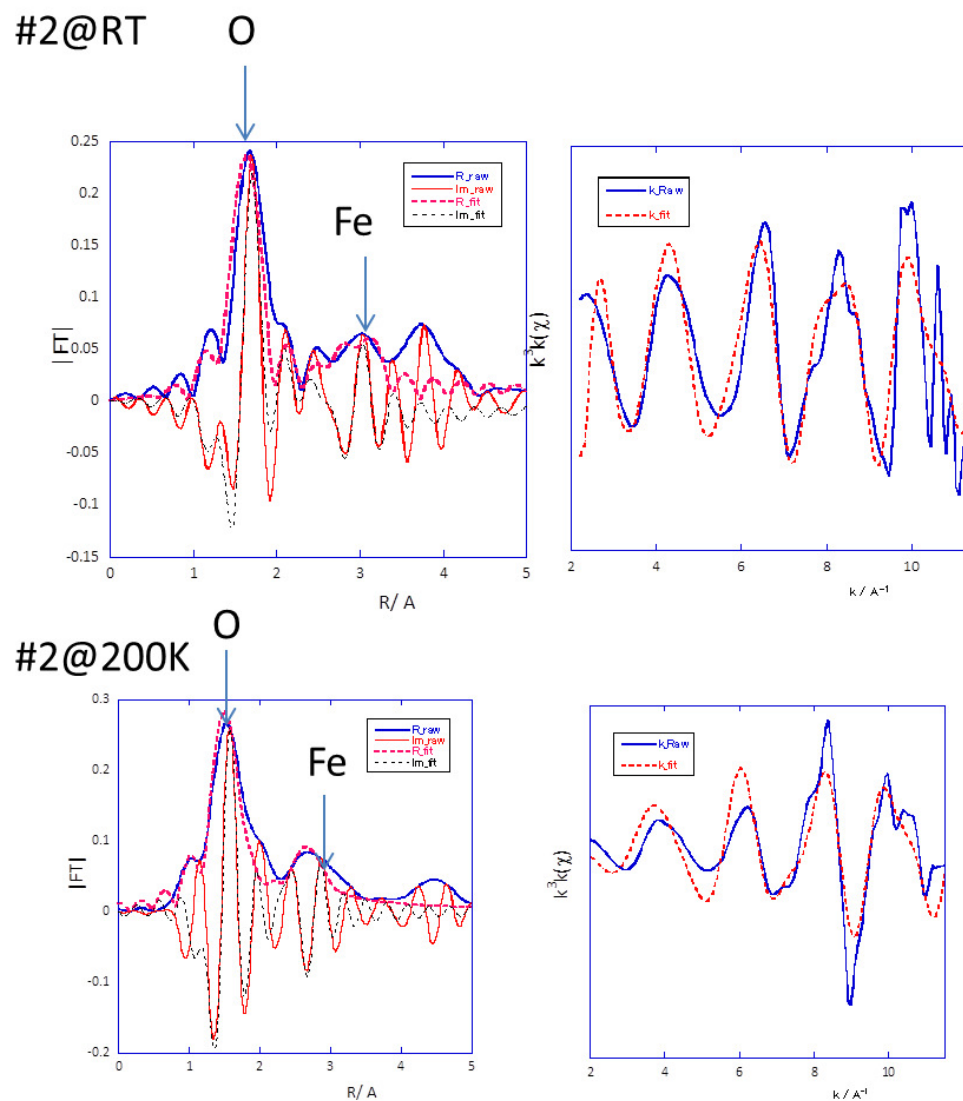


Figure 4.6. EXAFS (left) and Fourier transform (right) of native DPGA capsule from *B. licheniformis*. Blue solid lines are raw data, red dashed lines are fitted lines.

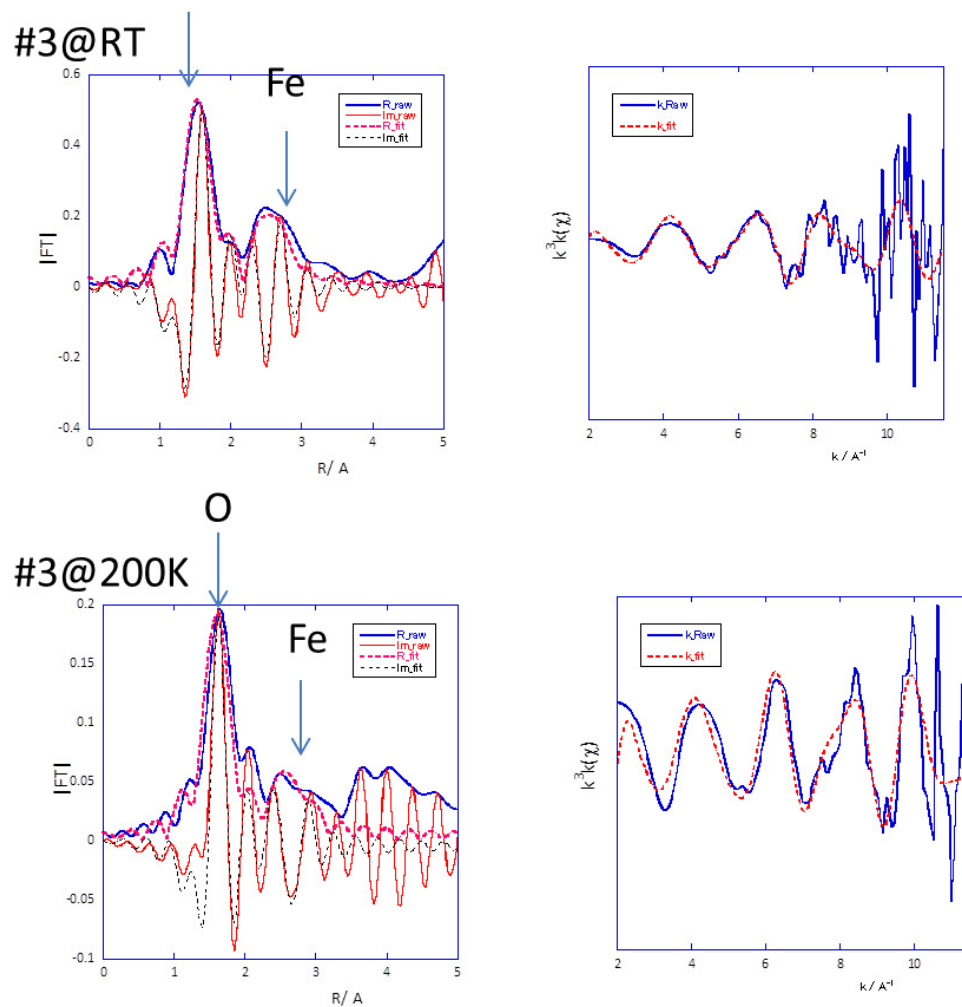


Figure 4.7. EXAFS (left) and Fourier transform (right) of iron-supplemented DPGA capsule from *B. licheniformis*. Blue solid lines are raw data, red dashed lines are fitted lines.

#4@RT

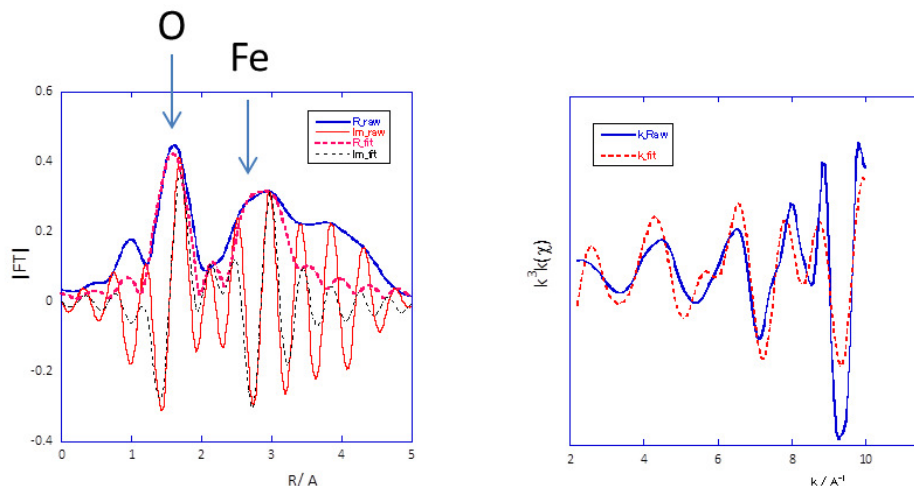


Figure 4.8. EXAFS (left) and Fourier transform (right) of iron-free DPGA from *B. licheniformis*. Blue solid lines are raw data, red dashed lines are fitted lines.

A report of important Fe-O bond distances are reported in Table 4.1. These distances range from 1.96 \AA to 2.02 \AA , which are consistent with other Fe-O single bond distances reported in the literature. Furthermore, Fe-Fe distances were recorded. Samples 1 and 3 exhibit a consistent Fe-Fe distance at both 200K and 298K. Interestingly, the average Fe-Fe distances in sample 2 decrease at 200K from 3.14 \AA at 298K to 3.02 \AA .

Table 4.1. Summary of important bond distances determined from models fit to the EXAFS data.

	Interaction	S_0^2	N	R/ Å	$s^2/\text{\AA}^2$	E_0 / eV
#1@RT	Fe-O	0.80	6	2.02 (0.01)	0.003	5.8
	Fe-Fe		0			
#1@200K	Fe-O	0.89	6	2.01(0.01)	0.001	6.9
	Fe-Fe		0			
#2@RT	Fe-O	0.8	6	2.02(0.01)	0.001	6
	Fe-Fe		2	3.14(0.01)	0.001	8
#2@200K	Fe-O	0.85	6	1.98(0.01)	0.001	-2.7
	Fe-Fe		2	3.02(0.01)	0.001	-0.6
#3@RT	Fe-O	0.80	6	2.03(0.02)	0.001	9.2
	Fe-Fe		2	3.08(0.02)	0.001	8
#3@200K	Fe-O	0.80	6	1.96(0.01)	0.006	6
	Fe-Fe		2	3.07(0.01)	0.005	8
#4@RT	Fe-O	1.4	6	2.01(0.02)	0.001	16
	Fe-Fe		6	3.30(0.02)	0.001	6.2
#4@200K	Fe-O	ND	ND	ND	ND	ND
	Fe-Fe		ND	ND	ND	ND

Kinetic ability of PGA to remove iron from human transferrin

Diferrous human transferrin (Tf) binds two iron atoms to form holotransferrin (Tf-Fe₂) and distributes iron throughout the human internal environment. Previous experiments suggested that PGA has a high affinity for iron. Since PGA is generally understood to be part of the virulence mechanism of *B. anthracis* within the human body, we thought the interaction between PGA and Tf-Fe₂ was highly relevant and important to

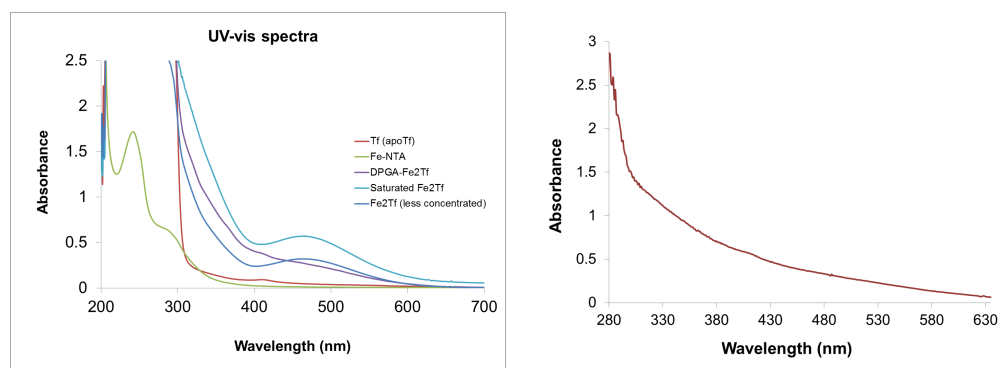


Figure 4.9. Relevant UV-vis spectra for the iron-loading of apo-transferrin (left) and iron-free DPGA (right).

study.

Apo-transferrin was purchased from Spectrum Chemicals and was loaded with iron by the addition of freshly prepared ferric nitrilotriacetic acid. The iron loading of Tf was confirmed by the characteristic UV-vis absorption band of Tf-Fe₂ at 470 nm. The kinetics of iron removal from Tf-Fe₂ was monitored by both UV-visible spectrophotometry and fluorescence. Relevant UV-vis spectra are presented in Fig. 4.9.

Rate constants and rate order determination have been determined for the iron removal by various iron chelators according to the equations listed in Eq. 4.1-4.3. The disappearance of the UV-vis band of Tf-Fe₂ at 470 nm is monitored by UV-vis spectrophotometry. The plot of $\ln[(A_t - A_\infty)/(A_{t_0} - A_\infty)]$ against time generates a slope that is equal to $-k_{\text{obs}}$.

Equation 4.3 describes saturation kinetics under pseudo-first order conditions where [L] is the PGA concentration. The constants k_2 and k_{max} can be calculated using a nonlinear least-squares program such as Hyperquad (26). When PGA concentration is very small compared to Tf, the rate is first order in PGA concentration and k_{obs} is equal to k_2 . Table 4.2 lists k_2 values recorded for other iron chelators. These values allow direct comparison between the efficacy of various chelators to remove iron from Tf-Fe₂.

$\text{FeTf} + \text{L} \rightleftharpoons \text{FeTfL} \longrightarrow \text{FeL} + \text{Tf}$	Eq.4.1
$k_{\text{obs}} = \ln(2)/t_{1/2}$	Eq. 4.2
$k_{\text{obs}} = k_2[\text{L}]/1+(k_2/k_{\text{max}})[\text{L}]$	Eq. 4.3

Table 4.2. Ligand saturation rate constants for various iron chelators.

Siderophore	$k_{\text{obs}} = k_{\text{max}} (10^{-2} \text{ min}^{-1})$
Enterobactin	2.1
Petrobactin	12.3
Aerobactin	0.3
DFO-B	~0
5LiO32HOPO	8.3

Varying molar equivalents (1:1, 1:5, 1:10) of DPGA and LDPGA to apo-Tf were used. Molecular weights of the capsules were estimated by SDS-page gel to be 150 kDa. Figure 4.10 shows the iron transfer from Tf-Fe₂ to DPGA over the course of several hours. Note that the higher molar ratio of DPGA results in UV-vis spectra that more resemble DPGA and that the 470 nm band due to Tf-Fe₂ is less prevalent. However, deconvolution of these overlapping species was possible with data refinement and the absorbances at 470 nm were still used for measuring iron removal from Tf-Fe₂.

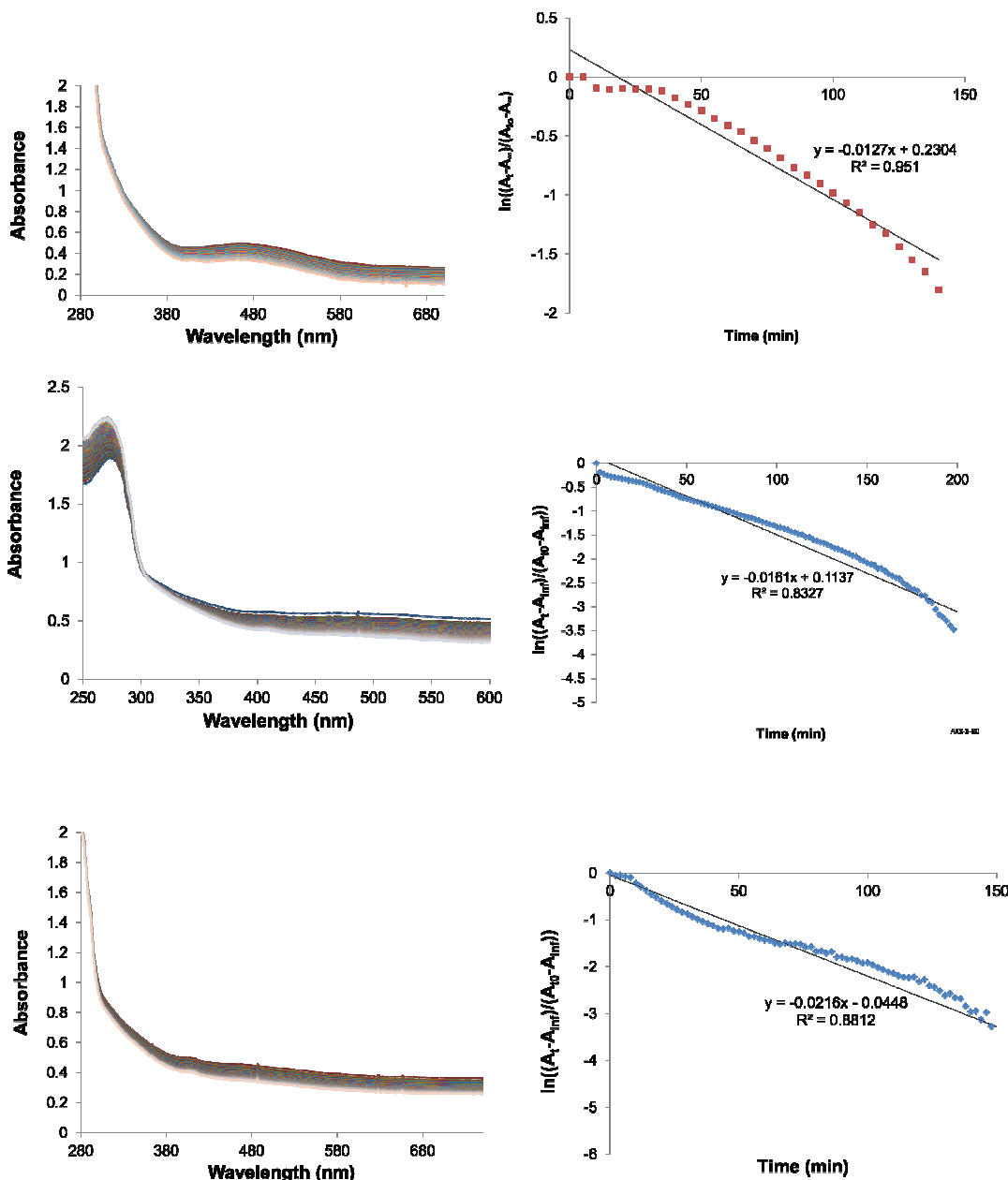


Figure 4.10. Left columns: UV-vis spectra of DPGA capsule added to Tf-Fe₂ over time. Right columns: Kinetics analysis of absorbances at 470 nm. Top row: data relevant to Tf-Fe₂:DPGA 1:1 (36 μM:36 μM) kinetics over 3.5 hours. Middle row: data for Tf-Fe₂:DPGA 1:5 (7.5 μM:37.5 μM) over 3.5 hours. Bottom row: data for Tf-Fe₂:DPGA 1:10 (7.5 μM:75 μM) over 3.5 hours.

The plot of $\ln[(A_t - A_\infty)/(A_0 - A_\infty)]$ against time for each of the iron removal experiments by DPGA generate linear slopes that are equal to $-k_{\text{obs}}$. Increasing DPGA molar equivalents results in an increase in k_{obs} values. A plot of k_{obs} versus equivalents of

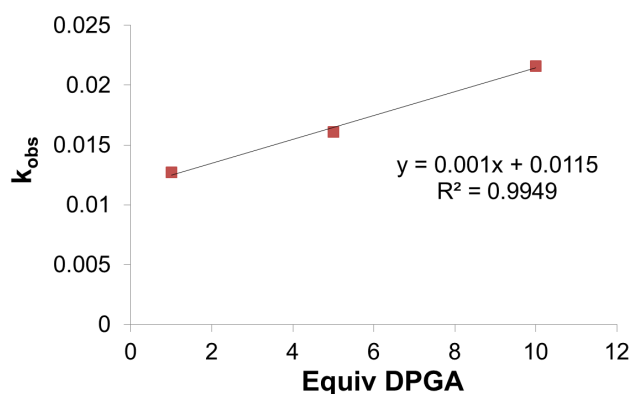


Figure 4.11. Saturation kinetics plot of k_{obs} versus equivalents of DPGA added in Tf-Fe₂ iron removal experiments.

However, a linear plot of k_{obs} versus molar equivalents of LDPGA generates three points that are within error limits of one another (Fig. 4.13).

DPGA (Fig. 4.11) shows a positive slope and is linear, implying first order reaction kinetics. The average of k_{obs} values suggests that $k_{obs} = k_{max} = 1.7 \times 10^{-2} \text{ min}^{-1}$ for DPGA as the iron chelator.

Iron removal by LDPGA generated similar trends in the raw UV-vis spectra. The Tf-Fe₂ absorbance peak at 470 nm decreases with addition of 1,5 and 10 molar equivalents of LDPGA capsule (Fig. 4.12).

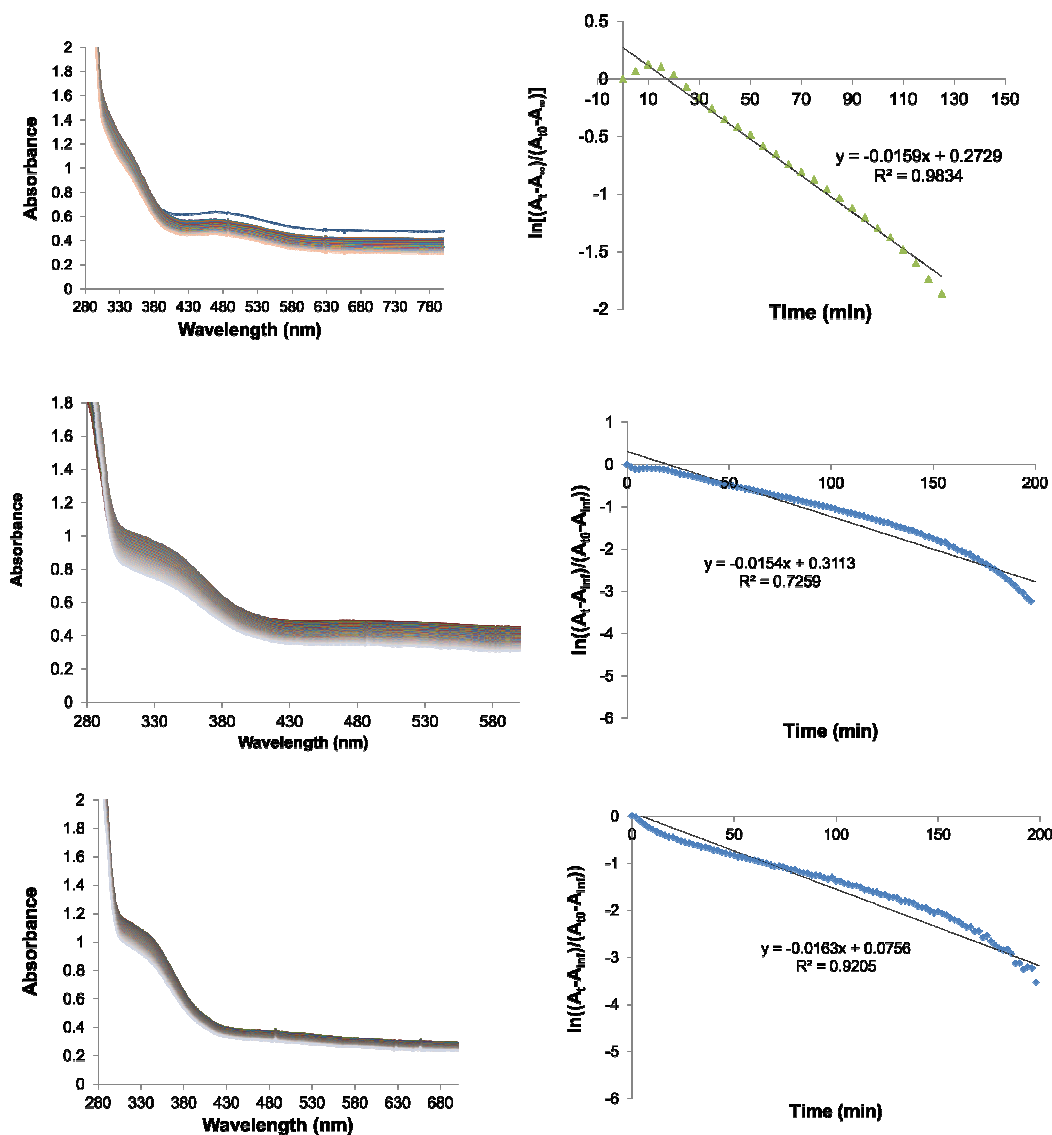


Figure 4.12. Left columns: UV-vis spectra of LDPGA capsule added to Tf-Fe₂ over time. Right columns: Kinetics analysis of absorbances at 470 nm. Top row: data relevant to Tf-Fe₂:LDPGA 1:1 (36 μM:36 μM) kinetics over 3.5 hours. Middle row: data for Tf-Fe₂:LDPGA 1:5 (7.5 μM: 37.5 μM) over 3.5 hours. Bottom row: data for Tf-Fe₂:LDPGA 1:10 (7.5 μM: 75 μM) over 3.5 hours.

Fluorescence emission spectroscopy was used as another method to measure iron removal kinetics by both DPGA and LDPGA capsules. Background fluorescence emission spectra were collected for capsules and Tf-Fe₂ separately. These background spectra are shown in Appendix 4.1 and 4.2.

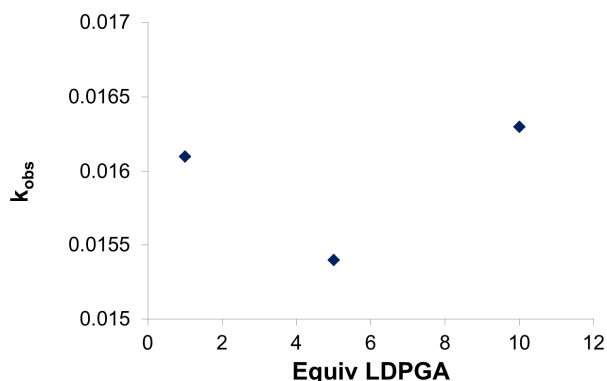


Figure 4.13. Kinetic analysis plot of k_{obs} versus molar equivalents of LDPGA capsule.

Background
fluorescence emission spectra
for Tf-Fe₂ varied over time
(Fig. A4.2) and thus made it
difficult to measure
fluorescence changes due to the
iron removal from Tf-Fe₂.
Nevertheless, the overall trend
in fluorescence emission
spectra is a decrease with the
addition of DPGA (Fig. 4.14).
The kinetics analysis plots of
 $\ln[(I_t - I_\infty)/(I_0 - I_\infty)]$ against time
show a negative slope that is

equal to $-k_{obs}$. There is more noise in the raw data for Tf-Fe₂:DPGA ratio of 1:5 and these data are not fitted as well as those data points in the case where Tf-Fe₂:DPGA is 1:1.

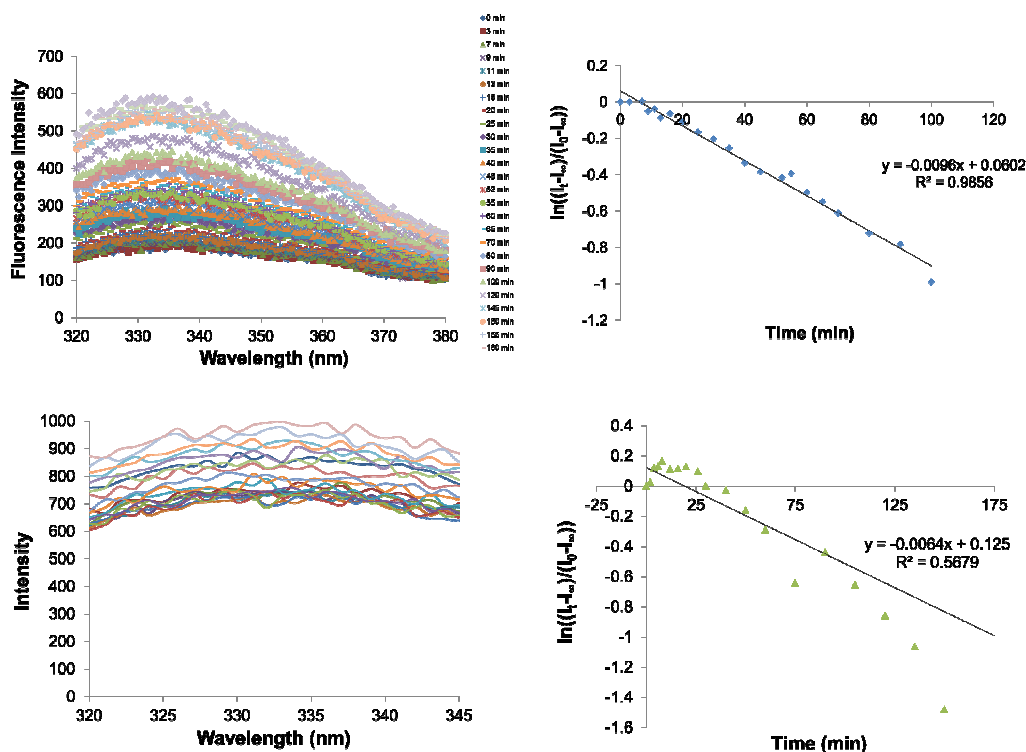


Figure 4.14. Left columns: Fluorescence spectra of Tf-Fe₂:DPGA. Right columns: Kinetics analysis of fluorescence data for Tf-Fe₂:DPGA of varying ratios. Intensities plotted were for emission intensities at 340 nm. Top row: ratio is 1:1 (7.5 μ M:7.5 μ M) for Tf-Fe₂:DPGA, total time = 170 min. Bottom row: Tf-Fe₂:DPGA ratio is 1:5 (7.5 μ M: 37.5 μ M).

Fluorescence spectra and kinetics analyses for the Tf-Fe₂-LDPGA iron transfer is shown in Figure 4.15. The ratios of Tf-Fe₂:LDPGA used were 1:1 and 1:5 to measure the rates of iron transfer from Tf-Fe₂ to LDPGA. In both instances, LDPGA behaves like DPGA. The kinetics plots of $\ln[(I_t - I_\infty)/(I_0 - I_\infty)]$ versus time show a negative slope ($-k_{\text{obs}}$) but the data points for 1:5 Tf-Fe₂:LDPGA do not fit well with the linear equation compared with the 1:1 Tf-Fe₂:LDPGA kinetic data.

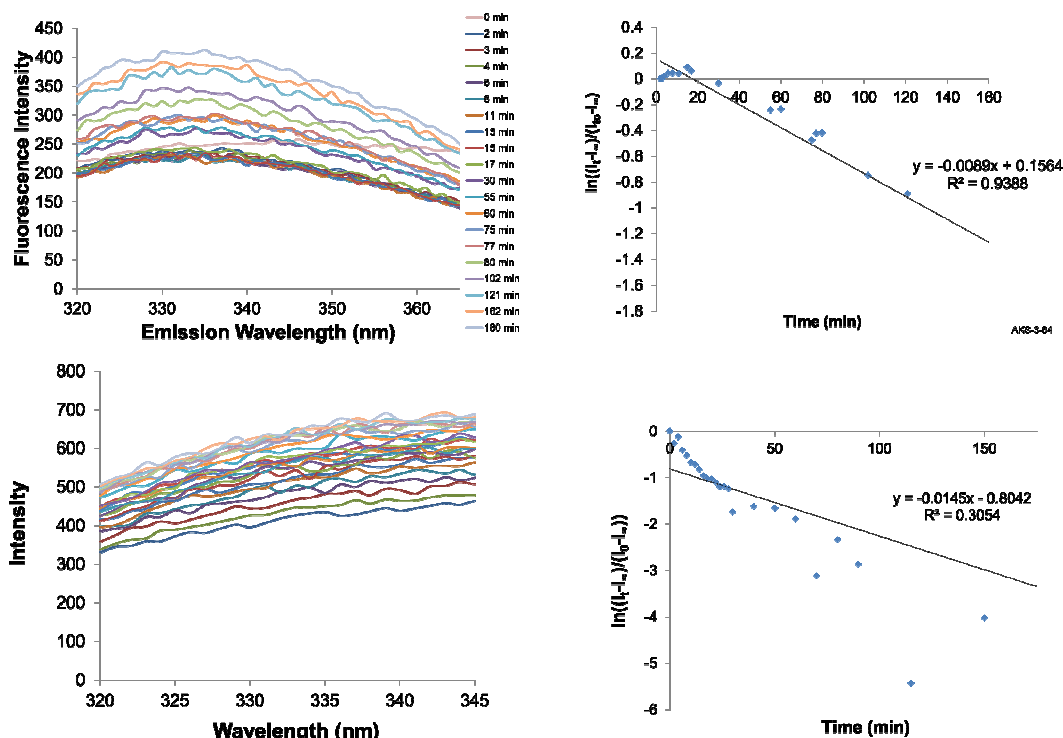


Figure 4.15. Left columns: Fluorescence emission data for Tf-Fe₂:LDPGA. Right columns: Kinetic analysis plot of intensities at 340 nm against time. Top row: Ratio is 1:1 (7.5 μ M:7.5 μ M) for Tf-Fe₂:LDPGA, total time 3 hr 30 min. Bottom row: Ratio is 1:5 (7.5 μ M: 37.5 μ M) for Tf-Fe₂:LDPGA, total time 3 hr 30 min.

Discussion

The inhibition of anthrax exotoxin activity by anthrax-produced PGA capsules is suspected to be part of a self-regulatory mechanism in which the pathogen prevents complete annihilation of a host's internal environment. The fact that iron plays a key role in the inhibitory PGA capsule activity is significant since the presence of iron in capsule was one of the main factors responsible for the inhibitory effects of PGA.

PA has no measurable affinity for bacterial siderophores

To understand the role of iron-containing PGA capsules with anthrax protective antigen inhibition, we pursued a variety of structure-function studies that were probed by spectroscopy. Through fluorescence quenching experiments, we determined that siderophores such as enterobactin and petrobactin do not deliver iron to anthrax protective antigen (PA). However, through toxin-activity assays performed by collaborators, we found that siderophores decrease the iron-PGA activity through sequestering iron from the capsule.

EXAFS studies reveal iron conglomerates within PGA polymer

Structural investigations about how iron affects the structure of iron-free DPGA capsule were pursued with EXAFS experiments, made possible through the help of EXAFS experts Dr. Yaita and group at the Japan Atomic Energy Agency in Japan. Generally, the Fe-LDPGA, native Fe-DPGA and Fe-supplemented DPGA samples had Fe-O bond distances between 1.96-2.02 Å which lie within a range typical for Fe-O single bonds formed between hard oxygen donors and Fe³⁺ ion. These measurements were consistent at both 298 K and 200 K. The native Fe-DPGA sample, however, exhibited shorter atom-atom distances between Fe-Fe vectors with lower temperature (200K). Further experiments at temperatures lower than 200K are being pursued to investigate a possible trend in shortened atom-atom distances near the iron centers with decreased temperatures. The average Fe-Fe distances of 3.14 Å at 298 K may be necessary for FeDPGA to function as an inhibitor of anthrax toxin. More information is required to explain the shortened Fe-Fe distances in the 200 K Fe-DPGA sample. Furthermore, the fact that the few iron atoms that are chelated by a DPGA polymer of 150 kDa and are conglomerated within 3.15 Å of each other is a clue toward understanding the relationship between Fe-DPGA and inhibitory activity toward anthrax toxin.

PGA polymers remove iron from human transferrin as fast as natural siderophores

Since the activity of DPGA capsule depended heavily on the iron content, another relevant inquiry we pursued was an investigation of the source of iron available for chelation by DPGA capsule. The ability of PGA capsules to sequester iron from human diferric transferrin sources (Tf-Fe₂) was investigated by UV-visible spectrophotometry and fluorescence emission spectroscopy.

Human transferrin carries two Fe³⁺ atoms in separate lobes of the protein. Amino acid residues of the protein and a carbonate ion are responsible for binding the Fe³⁺ atoms. Diferric human transferrin (Tf-Fe₂) has a UV-visible absorption band at 470 nm that diminishes when the Fe³⁺ is removed from the protein. We used this peak to monitor the rate of iron removal by PGA capsules (iron-free DPGA and LDPGA) over several hours. The iron transfer is completed after 2 hours. A kinetics analysis plot of $\ln[(A_t - A_\infty)/(A_{t_0} - A_\infty)]$ versus time was generated for both capsule-Tf-Fe₂ iron transfer events, from which $-k_{\text{obs}}$ rate constants were obtained. The average k_{obs} for DPGA was 0.001 min⁻¹

¹ higher than the average for LDPGA, but both sets of k_{obs} lie within the range of k_{obs} values determined for natural siderophores in transferrin iron-removal kinetics.

The kinetics of iron removal from human transferrin were also measured by fluorescence emission spectroscopy as another means of confirming k_{obs} . However, fluorescence emission by PGA capsules seemed variable with concentration of capsules. Note that in both Fig. 4.14 and Fig. 4.15 when the ratios of Tf-Fe₂:capsule is increased from 1:1 to 1:5, the emissions of Tf-Fe₂ appear similar to the spectra of capsules alone, and the fluorescence signal of Tf-Fe₂ is hampered by increased capsule density in the sample. The fluorescence results for a 1:5 mole ratio of Tf-Fe₂ to capsule suggested an experimental limit was reached and that fluorescence was not a good method for measuring samples with mole equivalents of capsule greater than 1. Nevertheless, the k_{obs} values obtained from both UV-vis and fluorescence kinetics experiments are compared in Table 4.3.

Table 4.3. Summary of experimentally determined pseudo-first order kinetics constants, k_{obs} (min⁻¹), as determined by UV-vis and fluorescence experiments. Varying ratios of DPGA and LDPGA capsules were used. Fluorescence experiments for 1:10 Tf-Fe₂:capsule were not determined since capsule emission hampered transferrin signals.

Fe ₂ Tf:DPGA	UV-vis	Fluorescence	Fe ₂ Tf:LDPGA	UV-vis	Fluorescence
1:1	0.0127	0.0096	1:1	0.0161	0.0089
1:5	0.0161	0.0076	1:5	0.0154	0.0145
1:10	0.0216	Not determined	1:10	0.0163	Not determined

The k_{obs} determined by UV-vis spectrophotometry are pseudo-first order rate constants that are comparable to the natural siderophores enterobactin and aerobactin in the ability to remove iron from Tf-Fe₂. The fact that the capsule is not one of the faster iron chelators available to *B. anthracis* may be related to the pathogen's careful regulation of anthrax toxin activity. In fact, the *B. anthracis* siderophore petrobactin is one of the faster iron chelators when the source of iron is human transferrin. Petrobactin plays an important role in supplying iron to *B. anthracis* in initial anthrax infection stages and thus may chelate iron quickly due to this role. The DPGA capsule is expressed in later stages of the pathogen's life cycle and may be intended for use in anthrax toxin regulation when the capsule acquires iron. A relatively fast rate of iron acquisition by DPGA may not be required for the bacterium at this stage.

Our understanding of iron acquisition and use by DPGA capsule in *B. anthracis* is slowly expanding. We have determined that human transferrin may be a source of iron for chelation by DPGA capsule, and that the Fe-DPGA capsule may possibly be used by the pathogen to modulate its exotoxin activity. The iron atoms chelated by DPGA are within angstroms of each other amongst a large (150 kDa) polymer, suggesting that such organization of metal ions is required for Fe-DPGA activity.

Experimental

General. All chemicals were obtained from commercial suppliers and used without further purification unless otherwise noted. Ultraviolet-visible spectra were measured with a Cary Model 300 Scan spectrophotometer. Inductively-coupled plasma experiments were done on an ICP Optima 7000 DV spectrometer (305 Latimer Hall, UC Berkeley). ICP standards were ordered from Ricca Chemical Company unless otherwise noted. ICP standard solutions were made using Millipore water and EDTA-soaked volumetric flasks. Holo-transferrin (ferric transferrin, >95%) was ordered from CalBioChem. Apo-transferrin (97%) was ordered from Spectrum Chemicals. Fluorescence spectroscopy was carried out on a Cary Eclipse spectrometer. Tris buffered saline solutions were 50 mM Tris, 150 mM NaCl, 20 mM NaHCO₃, pH= 7.4.

Anthrax Protective Antigen (PA) samples were expressed, isolated and purified according to reference (17).

Fluorescence binding assays of siderophores to PA. One hundred μ M of PA in TBS buffer was measured for inherent fluorescence ($\lambda_{\text{exc}} = 280$ nm, $\lambda_{\text{em}} = 320$ -340 nm). Twenty micromolar solutions of ferric and apo siderophores were freshly prepared and titrated into PA solutions and subsequent fluorescence was measured ($\lambda_{\text{exc}} = 280$ nm, $\lambda_{\text{em}} = 320$ -340 nm, PMT detector voltage = 900 V).

Poly- γ -(D)-glutamic acid capsule (DPGA) was expressed, isolated and purified according to previous protocols (25).

Extended X-ray Absorption Fine Spectra (EXAFS). PGA polymers (around 1 mM each) were thawed immediately before use. The EXAFS measurement was carried out at beam line BL11XU station at SPring8 laboratory in Hyogo prefecture, Japan, using the fluorescence and the transmission methods. The measurement was carried out on Fe K-edge. The extraction data of EXAFS oscillation from absorption spectra were carried out by WinXAS Ver. 3.1(27). The theoretical parameters for curve fittings of the EXAFS spectra were calculated using FEFF 8.20 (28).

Kinetic experiments: transfer of iron from human transferrin to PGA

UV-vis spectrophotometry. All experiments were carried out in filtered Tris buffered saline, pH = 7.4. Materials were thawed before use. One-hundred μ L cuvettes were used for these experiments. Under the Kinetics/Time-based measurement setup, the wavelengths 280 nm and 470 nm were monitored over the course of 10800 seconds (3 hours). Spectra were collected every 120 seconds, and a single-reference wavelength of 755 nm was used to correct for baseline shifting throughout the experiment.

Fluorescence kinetics experiments. All experiments were done in filtered tris buffered saline (pH = 7.4). Cary Eclipse fluorescence spectrophotometer with a 10 nm slit band pass for excitation and a 5 nm slit band pass for emission using the characteristic excitation and emission wavelengths $\lambda_{\text{exc}} = 280$ nm and $\lambda_{\text{em}} = 320$ -340 nm, respectively. Excitation and emission cut-off filters were both set to automatic. The PMT detector

voltage was manually selected to be 878-950 volts and the scan rate was set to slow. Fluorescence intensities were corrected for dilution due to addition of ligand.

References

1. Turnbull, P. (ed) (2008) *Anthrax in humans and animals* (World Health Organization).
2. Pile JC MJ (1998) ANthrax as a potential biological warfare agent. *Arch Intern Med* 158:429–434.
3. Inglesby TV HD (1999) Anthrax as a biological weapon: Medical and public health management. *JAMA* 281:1735–1745.
4. Cote CK, Welkos SL, Bozue J (2011) Key aspects of the molecular and cellular basis of inhalational anthrax. *Microbes and Infection* 13:1146–1155.
5. Honsa ES, Maresso AW (2011) Mechanisms of iron import in anthrax. *BioMetals* 24:533–545.
6. Wilson MK, Abergel RJ, Arceneaux JEL, Raymond KN, Byers BR (2010) Temporal production of the two *Bacillus anthracis* siderophores, petrobactin and bacillibactin. *Biometals* 23:129–134.
7. Abergel RJ et al. (2006) Anthrax pathogen evades the mammalian immune system through stealth siderophore production. *Proceedings of the National Academy of Sciences* 103:18499–18503.
8. Tournier J-N, Quesnel-Hellmann A, Cleret A, Vidal DR (2007) Contribution of toxins to the pathogenesis of inhalational anthrax. *Cellular Microbiology* 9:555–565.
9. Mock M, Fouet A (2001) Anthrax. *Annual Review of Microbiology* 55:647–671.
10. Bradley KA, Mogridge J, Mourez M, Collier RJ, Young JAT (2001) Identification of the cellular receptor for anthrax toxin. *Nature* 414:225–229.
11. Scobie HM, Rainey GJA, Bradley KA, Young JAT (2003) Human capillary morphogenesis protein 2 functions as an anthrax toxin receptor. *PNAS* 100:5170–5174.
12. Lacy DB (2004) Structure of heptameric protective antigen bound to an anthrax toxin receptor: A role for receptor in pH-dependent pore formation. *Proceedings of the National Academy of Sciences* 101:13147–13151.
13. Katayama H et al. (2008) GroEL as a molecular scaffold for structural analysis of the anthrax toxin pore. *Nature Structural & Molecular Biology* 15:754–760.

14. Milne JC, Furlong D, Hanna PC, Wall JS, Collier RJ (1994) Anthrax protective antigen forms oligomers during intoxication of mammalian cells. *J Biol Chem* 269:20607–20612.
15. Mogridge J, Cunningham K, Collier RJ (2002) Stoichiometry of Anthrax Toxin Complexes†. *Biochemistry* 41:1079–1082.
16. Petosa C, Collier RJ, Klimpel KR, Leppla SH, Liddington RC (1997) Crystal structure of the anthrax toxin protective antigen. *Nature* 385:833–838.
17. Kintzer AF et al. (2009) The Protective Antigen Component of Anthrax Toxin Forms Functional Octameric Complexes. *Journal of Molecular Biology* 392:614–629.
18. Abrami L, Liu S, Cosson P, Leppla SH, Goot FG van der (2003) Anthrax toxin triggers endocytosis of its receptor via a lipid raft-mediated clathrin-dependent process. *J Cell Biol* 160:321–328.
19. Friedlander AM (1986) Macrophages are sensitive to anthrax lethal toxin through an acid-dependent process. *J Biol Chem* 261:7123–7126.
20. Miller CJ, Elliott JL, Collier RJ (1999) Anthrax Protective Antigen: Prepore-to-Pore Conversion †. *Biochemistry* 38:10432–10441.
21. Krantz BA, Finkelstein A, Collier RJ (2006) Protein Translocation through the Anthrax Toxin Transmembrane Pore is Driven by a Proton Gradient. *Journal of Molecular Biology* 355:968–979.
22. Bruckner V, Kovács J, Dénes G (1953) Structure of Poly-D-glutamic Acid isolated from Capsulated Strains of *B. anthracis*. *Nature* 172:508–508.
23. Candela T, Fouet A (2006) Poly-gamma-glutamate in bacteria. *Molecular Microbiology* 60:1091–1098.
24. Wang F, Ishiguro M, Mutsukado M, Fujita K, Tanaka T (2008) Microstructure of Poly(γ -glutamic acid) Produced by *Bacillus subtilis* Consisting of Clusters of d - and l -Glutamic Acid Repeating Units. *Journal of Agricultural and Food Chemistry* 56:4225–4228.
25. Kintzer AF, Tang II, Schawel AK, Brown MJ, Krantz BA (2012) Anthrax toxin protective antigen integrates poly- γ -D-glutamate and pH signals to sense the optimal environment for channel formation. *Proc Natl Acad Sci USA* 109:18378–18383.
26. Gans, Peter, Sabatini, Antonio, Vacca, Alberto (1996) Investigation of equilibria in solution. Determination of equilibrium constants with the HYPERQUAD suite of programs. *Talanta* 43:1739–1753.

27. Ressler, T. (1998) WinXAS: A XAS Data Analysis Program under MS Windows. *J Synch Rad* 5:118.
28. Ankudinov AL, Ravel B, Rehr JJ, Conradson SD (1998) Real-space multiple-scattering calculation and interpretation of x-ray-absorption near-edge structure. *Phys Rev B* 58:7565–7576.

Ch. 4 Appendix

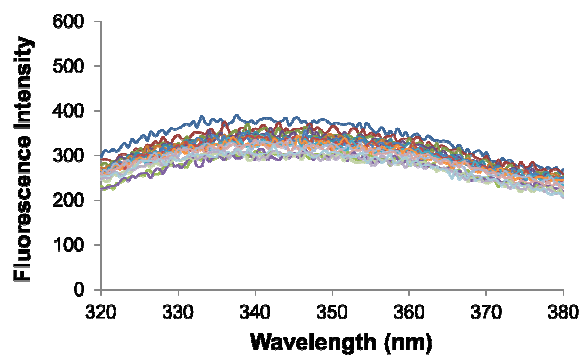


Figure A4.1. Background fluorescence spectrum of 7.5 μM DPGA in Tris buffer over total time 8.2 hr.

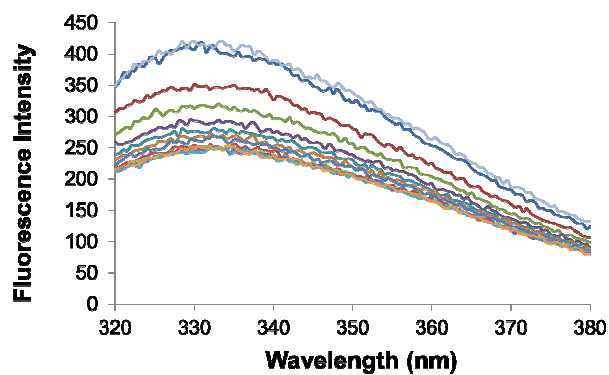


Figure A4.2. Fluorescence emissions of (7.5 μM) Fe₂Tf in Tris buffer over total time 3.5hr.

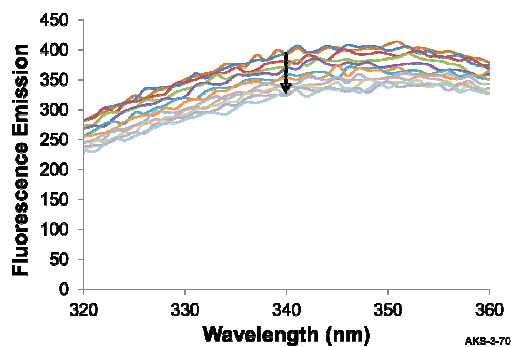


Figure A4.3. Control fluorescence data of LDPGA only (7.5 μM), total time 3hr 30 min.

Chapter 5

Siderocalin-mediated Iron Transport through use of Mammalian Siderophores

Introduction

The human immunoprotein siderocalin (Scn, also known as NGAL, Lcn2, HNL, uterocalin) works as a bacteriostatic agent to combat iron thievery by intercepting bacterial ferric siderophores (1–4). Siderocalin (Scn) binds many iron-siderophores through cation-pi and hybrid electrostatic interactions (5). Key residues in the calyx, or binding area of the Scn, are two lysines (K134, K125), one arginine (R81) and one hydrogen-bonding residue tyrosine (Y106). The calyx is also rigid; it has three pockets which impose steric constraints on its ligands. As a consequence of Scn interception of ferric siderophores, bacteria rely on alternative iron acquisition strategies or face severely limited growth.

While extensive studies have elucidated the role of siderocalin in the competition for iron between mammals and bacteria, recent literature suggests that siderocalin can be secreted in response to non-bacterial stimuli (6–9). This finding suggested that siderocalin may be more than just a bacteriostatic agent. In atransferrinemic mice, organogenesis has been linked to siderocalin, suggesting siderocalin may play some part in mammalian iron transport (10, 11). This would require that siderocalin bind an organic cofactor, otherwise identified as an endogenous ligand since siderocalin does not bind iron directly.

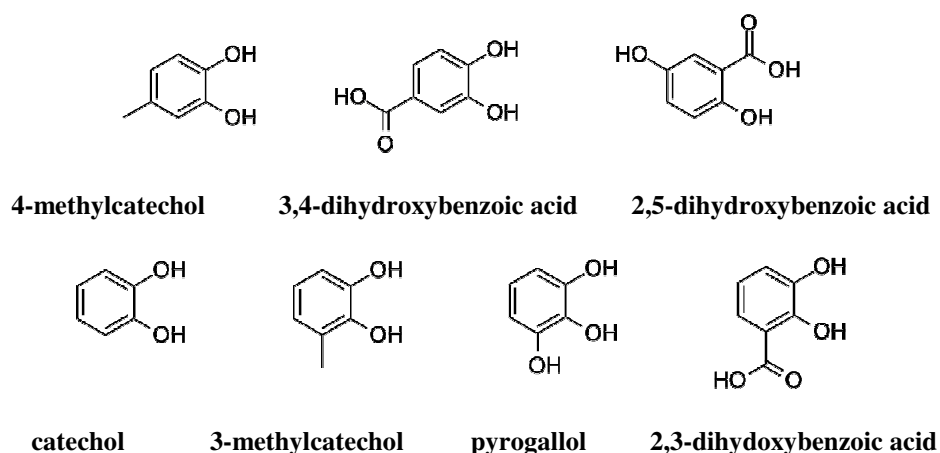
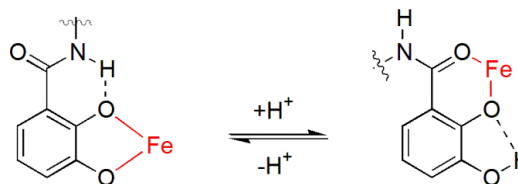


Figure 5.1. A sample of simple catechols that have been screened for mammalian siderophore activity by Bao et al (12).

The first structural identifications of a mammalian siderophore were made in 2010, after many decades of ambiguity regarding the exact identity of an endogenous

iron-transport mammalian siderophore. These mammalian siderophores were identified as catechol and other simple catechol derivatives (12, 13), some of which are shown in Fig. 5.1. Other simple catechols are portrayed in Fig. 5.1 as part of a collection of simple molecules screened by Bao et al. for mammalian siderophore activity (12).

Some disagreement exists in the literature regarding the mammalian siderophore candidacy of 2,5-dihydroxybenzoic acid, or gentisic acid (GA). GA is a constitutional isomer of 2,3-dihydroxybenzoic acid (23DHB), the monomeric unit of the siderophore enterobactin. Both enterobactin and 23DHB are bound by Siderocalin as the corresponding iron complexes. The simple metabolite 23DHB is generally understood to be a mammalian siderophore since binds both iron and Siderocalin and is found endogenously in humans. Deviredy et al. propose that GA is a mammalian siderophore for similar reasons (13). However, several studies suggest that salicylate-mode binding of iron is sterically incompatible with the siderocalin binding pocket (12, 14–16). In fact, the acidification of ferric enterobactin, and a subsequent shift in catecholate to salicylate iron-binding modes (Scheme 5.1) is thought to be part of a putative iron release mechanism from siderocalin-bound siderophores (16–20). Siderocalin is acid-resistant and does not unfold or lose function at pH = 4. A catecholate to salicylate shift in coordination also significantly decreases the Scn affinity for the iron siderophore complex due to binding pocket steric restrictions (15, 16).



Scheme 5.1. Catecholate (left) to salicylate (right) iron coordination.

Further studies were done in attempt to resolve the controversy around GA as a mammalian siderophore. Specifically, iron-GA formation was investigated as well as the iron-GA affinity for Scn. Collaborative work was aimed at clarifying the role of GA in apoptosis by Scn-mediated mammalian iron transport.

Results

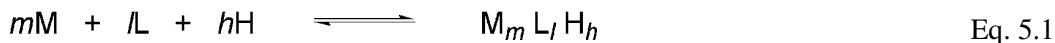
Investigation of iron-GA complexes

Several experiments were designed to investigate the formation of possible Fe(GA) complexes. GA is a bidentate chelator and has up to 3 dissociable protons. Fe^{III} prefers a six-coordinate environment, thus various Fe(GA) complexes are possible. Equilibrium constants relevant to the complex speciation of Fe(GA) were obtained from the literature and are described in Table 5.1 (21, 22).

Table 5.1 Relevant equilibria for Fe-GA complexation.

Associative equilibrium	Association constant (expressed as K_{MLH} and β_{MLH})	
	K_{011} 13.80	β_{011} 13.80
	K_{012} 10.20	β_{012} 24.00
	K_{013} 2.99	β_{013} 26.99
	K_{110} 13.5	β_{110} 13.5
	K_{120} 11.6	β_{120} 25.1
	K_{130} 7.6	β_{130} 32.7

The equilibria are expressed as associative processes with both stepwise (K_{MLH}) and cumulative (β_{MLH}) association constants, where the subscripted MLH refers to the molar equivalents of metal, ligand and protons (Eq. 5.1 and Eq. 5.2).



$$\beta_{mlh} = \frac{[M_m L_l H_h]}{[M]^m [L]^l [H]^h} \quad \text{Eq. 5.2}$$

Ligand protonation constants, metal-complexation constants as well as iron-hydrolysis constants were used to calculate the distribution of various iron species in aqueous solution, otherwise known as a speciation diagram. Speciation diagrams were generated using the program HySS (Hyperquad Simulation and Speciation) (23). The distribution of metal species are calculated across a range of pH at designated concentrations of ligand and metal.

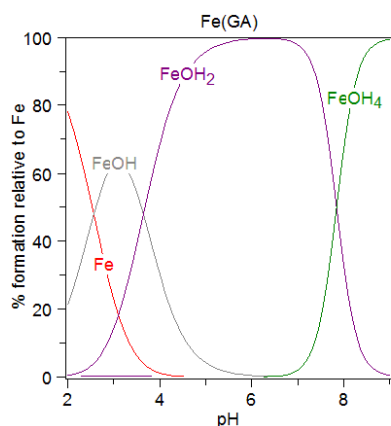
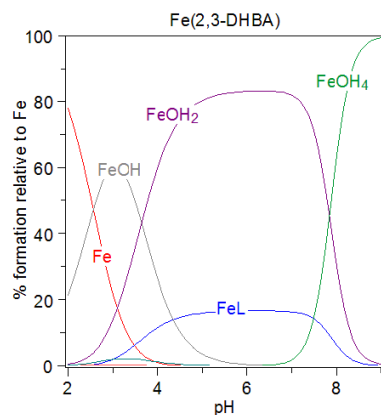


Figure 5.2. Speciation diagram for Fe(GA), where $[Fe] = 20 \mu M$ and $[GA] = 60 \mu M$.

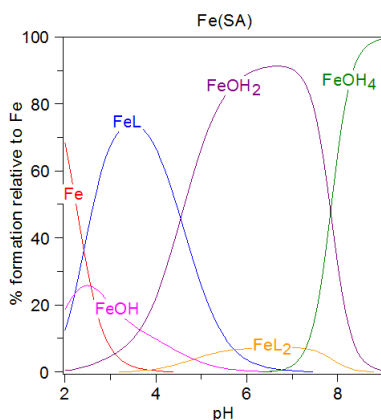
The speciation diagram for Fe-GA was generated using the concentrations $Fe = 20 \mu M$ and $GA = 60 \mu M$. Iron hydroxo species dominate the diagram, especially at $pH = 7.4$. Variation of Fe and GA concentrations and molar equivalents do not favor a significant formation of Fe(GA) species.

Speciation diagrams for two other bidentate ligands, 2,3-dihydroxybenzoic acid (23DHB, Fig. 5.1) and salicylic acid (SA) were generated for comparison to GA. Relevant equilibria for each bidentate ligand and iron complexes are listed as either K_{MLH} or β_{MLH} . Both diagrams were generated using concentrations of $Fe = 20 \mu M$ and bidentate chelator = $60 \mu M$.

The speciation calculation for 23DHB shows that the 1:1 Fe:23DHB complex forms about 18% of all iron species in solution from $pH = 4.5$ - 7.5 (Fig. 5.3). Note that the K_{110} constant for Fe(23DHB) is 20.51, compared to K_{110} for Fe(GA) which is 13.5 (Table 5.1). Salicylic acid, or SA, has only 2 dissociable protons and thus only two ligand protonation constants. The K_{110} for Fe(SA) is 15.81 and two different Fe(SA) complexes form near $pH = 7$. Fe(SA)₂ constitutes about 9% of all iron species in solution at $pH = 7.4$ whereas Fe(SA) is present in about 1% of the total composition (Fig 5.3).



$$\begin{aligned}
 K_{011} &= 13.12 & \beta_{011} &= 13.12 \\
 K_{012} &= 10.06 & \beta_{012} &= 23.18 \\
 K_{013} &= 2.70 & \beta_{013} &= 25.88 \\
 K_{110} &= 20.51 & \beta_{110} &= 20.51 \\
 K_{120} &= 7.39 & \beta_{120} &= 27.81 \\
 K_{130} &= 4.31 & \beta_{130} &= 32.12
 \end{aligned}$$



$$\begin{aligned}
 K_{011} &= 13.15 & \beta_{011} &= 13.15 \\
 K_{012} &= 3.13 & \beta_{012} &= 16.28 \\
 K_{110} &= 15.81 & \beta_{110} &= 15.81 \\
 K_{120} &= 11.69 & \beta_{120} &= 27.50 \\
 K_{130} &= 7.81 & \beta_{130} &= 35.31
 \end{aligned}$$

Figure 5.3. Top: Speciation diagram for Fe(2,3-DHBA), where $[\text{Fe}] = 20 \mu\text{M}$ and $[\text{2,3-DHBA}] = 60 \mu\text{M}$ (left) and relevant stepwise and cumulative association constants (right). Bottom: Speciation diagram for Fe(SA) for $[\text{Fe}] = 20 \mu\text{M}$ and $[\text{SA}] = 60 \mu\text{M}$ (left) and relevant stepwise and cumulative association constants (right).

Speciation calculations show that no appreciable amount of $\text{Fe}(\text{GA})_x$ forms at $\text{pH} = 7.4$. UV-visible spectra was used to confirm this theoretical result. UV-visible spectra of $\text{Fe}(\text{GA})$ solutions were collected where the molar ratios of $\text{Fe}:\text{GA}$ were varied (Fig. 5.4). Maximum absorbance peaks at $\lambda = 320 \text{ nm}$ correspond to ligand transitions within GA. Furthermore, siderocalin was added to these solutions and subsequent UV-visible spectra are shown in Figure 5.4. Siderocalin alone has a $\lambda_{\text{max}} = 280 \text{ nm}$. The addition of siderocalin does not affect the spectrum of $\text{Fe}(\text{GA})$ solutions.

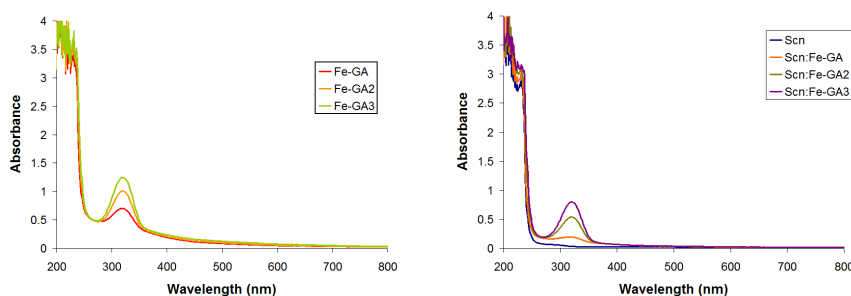


Figure 5.4. UV-visible spectra of Fe(GA) solutions at pH = 7.4 for 1, 2, and 3 molar equivalents of GA (left). UV-visible spectra of Fe(GA) solutions with added siderocalin (right) at pH = 7.4.

Attempts to synthesize the Fe(GA)₃ complex in the presence of base resulted in clear colorless crystals amidst a green solution. These crystals were examined by X-ray diffraction and were identified as the commercially available 2,5-DHB ligand.

Measuring the siderocalin affinity for Fe(GA)_x

Siderocalin fluorescence binding assays were performed to investigate whether the protein could facilitate formation of Fe complexes in the calyx. The bidentate ligands GA, 23DHB and SA were used to form iron complexes *in situ*, which would then be

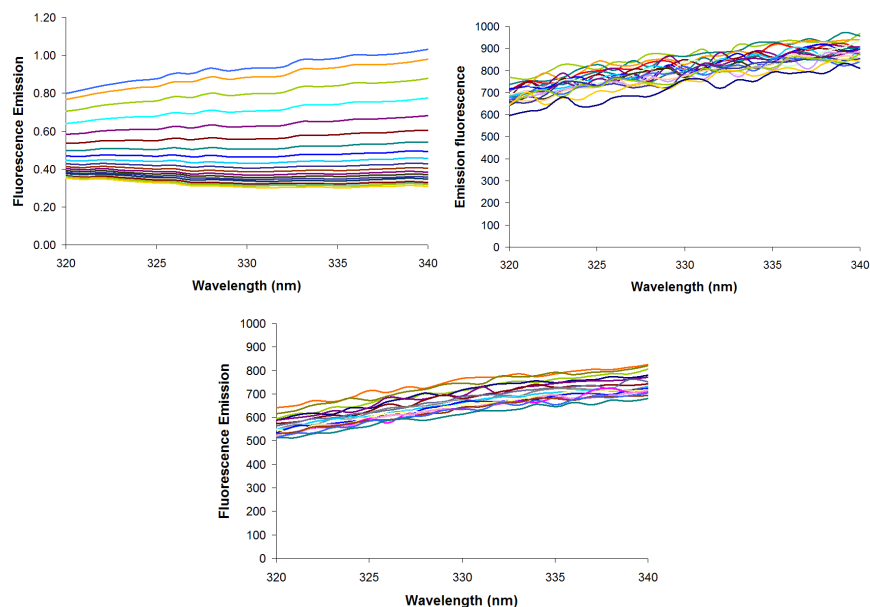
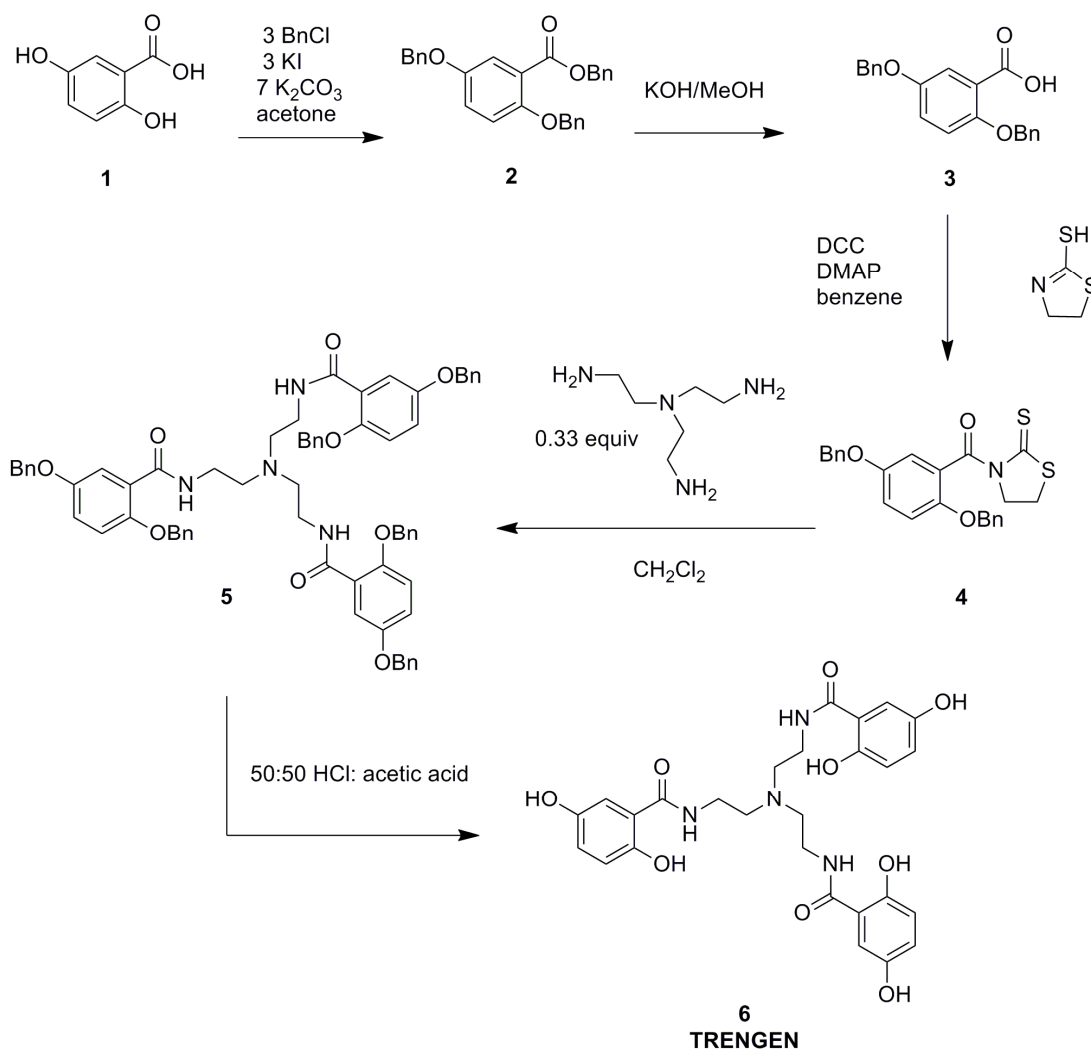


Figure 5.5. Raw data from siderocalin fluorescence binding assays with Fe(23DHB) (top left), Fe(SA) (top right) and Fe(GA) (bottom) used as substrates.

added to solutions of siderocalin. The ligand 23DHB was used as a positive control since it is the monomeric version of enterobactin, a siderophore known to bind siderocalin tightly, whereas SA was used as a negative control since salicylate siderophores do not typically bind siderocalin. In these assays, 100 μ M siderocalin was titrated with aliquots of Fe-bidentate ligand complexes and the fluorescence emission intensities of siderocalin were recorded (Fig. 5.5). The addition of Fe(23DHB) solution to siderocalin results in a 50% decrease in siderocalin fluorescence, suggesting that the iron complex is tightly bound by siderocalin. In the case of the negative control, Fe(SA) solutions do not decrease siderocalin fluorescence more than 18%, which is not a significant change compared to background siderocalin fluorescence decreases observed due to effects such as photobleaching. The addition of Fe(GA) solutions to siderocalin results in similar effects, where the decrease in siderocalin fluorescence does not exceed 15%.



Scheme 5.2. Synthesis of the salicylate-mode binding synthetic siderophore TRENGEN.

Synthesis of a hexadentate iron chelator based on GA

Efforts to form an iron complex bound by GA were pursued by synthesizing a hexadentate siderophore based on GA binding units. The salicylate-based hexadentate siderophore TRENGEN was synthesized according to Scheme 5.2. Gentisic acid, or 2,5-dihydroxybenzoic acid (**1**), was triply benzyl protected under Finkelstein reaction conditions to form **2**, which was saponified to give **3**. Coupling of **3** with 2-mercaptothiazoline with DCC and a catalytic amount of DMAP in benzene afforded **4**.

Three equivalents of **4** were added to TREN under slightly basic conditions in methylene chloride to give the hexa-benzyl-protected TRENGEN, **5**. Deprotection of **5** under acidic conditions yielded TRENGEN (**6**).

TRENGEN was also tested for siderocalin binding by the fluorescence quenching assay. The raw data are shown in Figure 5.6. Note that maximum quenching obtained by either apo- or ferric- TRENGEN was less than 20%.

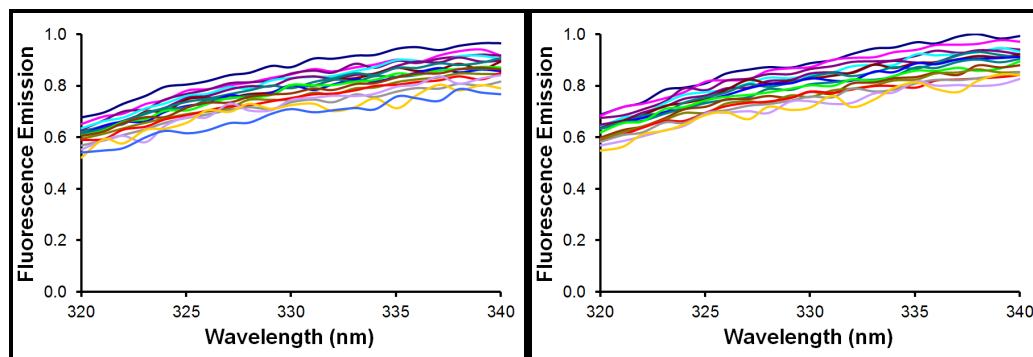


Figure 5.6. Raw siderocalin fluorescence quenching results from the addition of apo- (left) and ferric- (right) TRENGEN.

Discussion

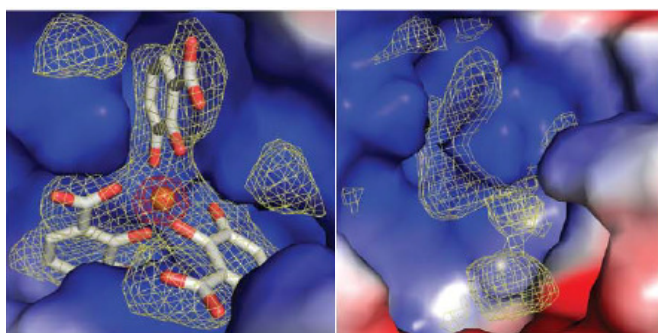


Figure 5.7. Siderocalin calyx (modeled as a molecular surface) with contrasting iron complexes. Iron atoms are orange spheres. (Left) crystal structure of Fe(23DHB)_3 in calyx of siderocalin and residual electron density of Fe(GA)_3 (right).

Solution thermodynamics analyses show that GA does not bind iron

Speciation calculations gave theoretical evidence that Fe(GA)_x complexes do not form across a wide range in pH, contrary to speciation calculations generated for Fe(23DHB) and Fe(SA) systems. Furthermore, UV-visible spectra of varying Fe:GA molar ratios do not have a metal to ligand charge transfer band ($\lambda_{\text{max}} = 500\text{--}750$ nm) that is typical of an Fe^{3+} complex. The absorption band

at $\lambda_{\text{max}} = 320 \text{ nm}$ corresponds to ligand transitions within GA, a result that is confirmed with UV-visible spectra of GA alone (data not shown).

The addition of siderocalin to $\text{Fe}(\text{GA})$ solutions does not result in a shift of λ_{max} , suggesting that siderocalin does not form a ternary complex with $\text{Fe}(\text{GA})_x$. In some cases, the addition of a protein may facilitate the formation of a *tris*-bidentate Fe^{3+} complex, but this process is usually identifiable by UV-vis spectrophotometry.

$\text{Fe}(\text{GA})_x$ complexes were not isolable by traditional iron complexation techniques. Even under basic conditions in which the conjugate base of GA was generated, no $\text{Fe}(\text{GA})$ complex crystallized out of solution. Instead, the clear crystals were resolved as GA without any iron in the crystal data. Attempts to form $\text{Fe}(\text{GA})$ complexes in the presence of siderocalin was attempted and monitored by protein crystallography experts at the Fred Hutchinson Cancer Research Center in Seattle, WA, USA. However, only siderocalin crystals were obtained without a bound iron complex, contrary to the Scn:Fe(23DHB) system in which a crystal structure was obtained (Fig. 5.7). A model of $\text{Fe}(\text{GA})$ in the binding pocket of siderocalin is shown in Figure 5.8, which shows a steric clash of the 5-hydroxyl group with the siderocalin walls of pocket #1.

Siderocalin fluorescence is not quenched by salicylate siderophores

The speciation distribution diagrams determined the main iron complexes in solution at $\text{pH} = 7.4$. This information was used to generate possible binding mechanisms for binding of the complex to siderocalin. Attempts to calculate K_D values for the interaction of each iron complex with siderocalin were made. The results are listed in Table 5.2. However, only the fluorescence change for Scn:Fe(23DHB) was significant enough to refine a protein-substrate dissociation constant by nonlinear regression analyses (Hyperquad) (24). The speciation plot for Fe(23DHB) indicates that the main species in solution at $\text{pH} = 7.4$ is the 1:1 Fe(23DHB) complex. Thus, this complex was proposed to be the species initially binding to siderocalin in the fluorescence binding assays. In effect, the dissociation constant calculated for Scn:Fe(23DHB) is representative of the affinity of siderocalin for the 1:1 Fe(23DHB) complex.

For both $\text{Fe}(\text{SA})$ and $\text{Fe}(\text{GA})$, the change in fluorescence quenching was not large enough for a binding curve to be generated, and a dissociation constant could not be calculated without significant error.

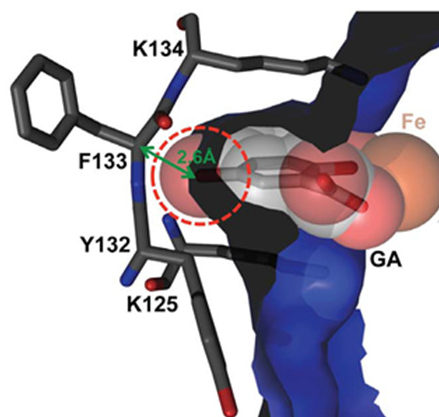


Figure 5.8. Modeling of $\text{Fe}(\text{GA})$ inside siderocalin pocket 1.

Table 5.2 Proposed binding mechanisms to siderocalin by various iron-bidentate ligand complexes and corresponding dissociation constants.

Bidentate ligand	Equilibria*	K_d (nM)
2,3-DHBA	$\text{Scn} + \text{Fe}(2,3\text{-DHBA}) \rightleftharpoons \text{Scn:Fe}(2,3\text{-DHBA})$ $K_d = [\text{Scn:Fe}(2,3\text{-DHBA})] / [\text{Scn}] [\text{Fe}(2,3\text{-DHBA})]$	0.101 ± 0.002
SA	$\text{Scn} + \text{Fe}(\text{SA}) \rightleftharpoons \text{Scn:Fe}(\text{SA})$ $K_{d1} = [\text{Scn:Fe}(\text{SA})] / [\text{Scn}] [\text{Fe}(\text{SA})]$ $\text{Scn:Fe}(\text{SA}) + \text{SA} \rightleftharpoons \text{Scn:Fe}(\text{SA})_2$ $K_{d2} = [\text{Scn:Fe}(\text{SA})_2] / [\text{Scn:Fe}(\text{SA})] [\text{SA}]$	No binding
GA	$\text{Scn} + \text{Fe}(\text{GA}) \rightleftharpoons \text{Scn:Fe}(\text{GA})$ $K_d = [\text{Scn:Fe}(\text{GA})] / [\text{Scn}] [\text{Fe}(\text{GA})]$	No binding

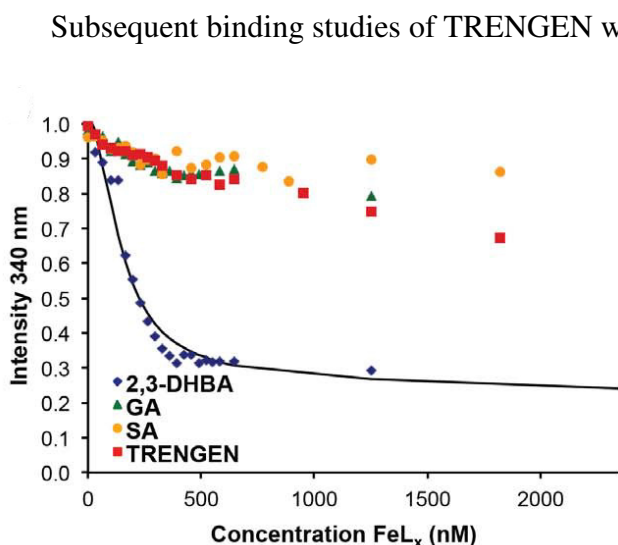


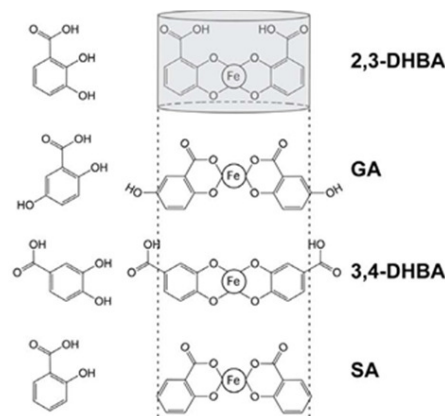
Figure 5.9. Siderocalin fluorescence quenching plot of fluorescence emission versus volume of substrate added.

Subsequent binding studies of TRENGEN with Scn via fluorescence quenching assay showed that both the apo- and ferric- TRENGEN substrates did not quench Scn fluorescence by more than 20% (Fig. 5.6). This percentage of quenching is not much different from the percentage of quenching seen from dilution with buffer (about 5-10%) and is considered insignificant, at most indicating some sort of nonspecific binding to the Scn calyx.

The plot in Figure 5.9 summarizes the binding

affinities of siderocalin for the iron complexes discussed, namely, Fe(23DHB), Fe(SA), Fe(GA), Fe(TRENGEN). Significant siderocalin quenching is observed with a small aliquot of Fe(23DHB), and the quenching levels off as soon as the system reaches an equilibrium.

The iron complexes of GA, SA and TRENGEN, on the contrary, do not quench siderocalin fluorescence as dramatically as Fe(23DHB). At most, 30% quenching is observed from the addition of TRENGEN but only after several (>15) molar equivalents of TRENGEN are added (Figure 5.9). Fe(TRENGEN) exhibits similar affinities for siderocalin compared with Fe(SA) and Fe(GA). What these three ligands have in common is that they all bind iron in a salicylate coordination mode (as in Scheme 5.1), which is generally a weaker mode of binding iron compared with catecholate coordination mode. Furthermore, the formation of iron-salicylate complexes is not optimized within the siderocalin calyx, since the addition of many equivalents of substrate does not change the binding outcome. Thus, even with a hexadentate version of GA, which is expected to have a greater binding affinity for iron due to fewer entropic barriers (compared to three bidentate ligands), no salicylate iron-binding ligand is bound by siderocalin. Furthermore, ferric-TRENGEN does not form a ternary complex with siderocalin, which is consistent with previous hexadentate iron-salicylate siderocalin binding studies (15, 16). While Fe(TRENGEN) has aromatic rings available for cation- π interactions with the basic residues of siderocalin, the complex is not highly charged, and the 5-hydroxyl on each of the aromatic rings imparts a steric clash with the siderocalin calyx walls.



Scheme 5.3. Diagram of schematic iron complex diameters for the bidentate ligands 23DHB, GA, 3,4-dihydroxybenzoic acid (34DHBA) and SA. The dotted lines represent the steric requirement by siderocalin binding pockets.

Purported siderocalin-iron-salicylate complexes do not induce apoptosis

Collaborators at the Iron Metabolism and Chelation Program at the University of Sydney in Australia have investigated the activity of mammalian siderophores and siderocalin *in vivo* to clarify the role of siderocalin-induced apoptosis. To evaluate the claim that siderocalin induces apoptosis through binding iron, as proposed by Devireddy et al., our collaborators conducted apoptosis assays in which iron chelators and siderocalin were added to FL5.12 cells. Apoptosis was measured by Annexin V-FITC/DAPI staining indicated by the manufacturer's kit (BD). While more extensive apoptosis assays were also performed (14), a brief description of the main results are shown in Figure 5.10. Apoptotic cells stain in the black boxes highlighted in Figure 5.10, and a higher density of apoptotic cells is represented by more data points contained in the black boxes. In this

experiment, the iron chelators that were able to sequester iron in the presence of siderocalin then withheld iron necessary for cell growth and induced apoptosis. As seen in Figure 5.10, apo-enterobactin and desferrioxamine are the only two siderophores that induce apoptosis with siderocalin present. This study suggests that the other chelators, 23DHB, 25DHB and TRENGEN, do not have significant affinity for iron with siderocalin and thus cannot withhold iron from FL5.12 cells.

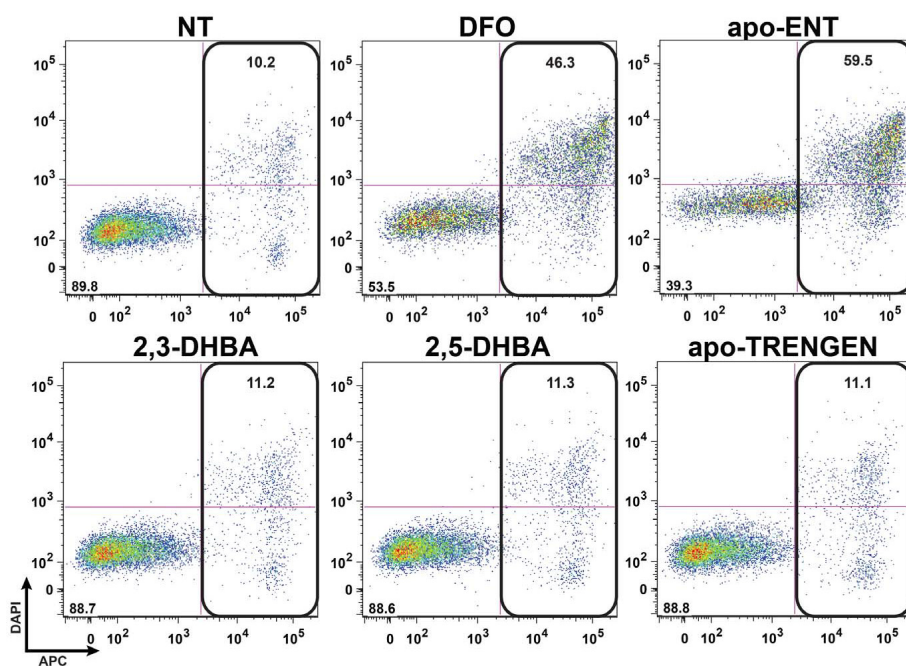


Figure 5.10. Results showing that siderocalin does not induce apoptosis in FL5.12 cells. Apoptosis was assessed by annexin V-FITC staining and DAPI was used as a vital stain. NT = no treatment, DFO = desferrioxamine B, apo-ENT = iron-free enterobactin.

Conclusion

The potential for siderocalin to be an iron delivery protein has significance in clinical studies and in human health. It is well understood that siderocalin cannot bind iron alone, as transferrin can, but requires an endogenous organic cofactor such as a mammalian siderophore to bind iron within the siderocalin calyx. To clarify whether the bidentate ligand GA is a mammalian siderophore, both *in vitro* and *in vivo* strategies were pursued in parallel. Speciation diagrams and UV-visible spectrophotometry showed that GA lacked an appreciable affinity for Fe^{3+} . Attempts to grow crystals of $\text{Fe}(\text{GA})$ complexes under favorable conditions were made, only to result in clear crystals of GA. Furthermore, a hexadentate version of GA was synthesized, called TRENGEN, for use in siderocalin binding assays. The ferric complexes of GA, SA, 23DHB and TRENGEN were tested for siderocalin binding by a fluorescence quenching assay. Of

these substrates, only Fe(23DHB) had significant affinity for siderocalin. A dissociation constant was calculated to describe this affinity, and a mechanism of binding to siderocalin was proposed based on the main species in solution determined by speciation calculations. The salicylate siderophores GA, SA and TRENGEN and corresponding iron complexes did not quench siderocalin fluorescence beyond background noise, thus indicating that salicylate siderophores do not form ternary complexes with iron and siderocalin. From these *in vitro* experiments, it is determined that salicylate siderophores cannot be mammalian siderophore candidates.

Further evidence collected by collaborators provided other lines of evidence that salicylate siderophores such as GA could not be mammalian siderophores. Crystal structures of siderocalin with Fe(GA) and Fe(TRENGEN) were unobtainable. A model of Fe(GA) in the siderocalin calyx demonstrates the steric clash between the 5-hydroxyl of GA and the rigid siderocalin calyx. Furthermore, *in vivo* studies that measured siderocalin-induced apoptosis in FL5.12 cells were conducted with various siderophores. Only those siderophores which had a significant affinity for iron (desferrioxamine B) or iron and siderocalin (enterobactin) induced apoptosis by withholding iron from growing cells. Salicylate siderophores and even the bidentate siderophore 23DHB did not have affinity for iron or iron and siderocalin that was significant enough to induce apoptosis.

The collective evidence reported in this chapter (and more in reference (14)) demonstrate that GA cannot be a mammalian siderophore since its affinity for iron alone is nearly nonexistent. Furthermore, Fe(GA) does not form within the siderocalin calyx and thus GA cannot be categorized as a mammalian siderophore. These results have important implications for clinical research centered around siderocalin as an iron transport protein.

Experimental

General. All chemicals were obtained from commercial suppliers and used without further purification unless otherwise noted. Chemical analyses were performed by the Microanalytical Services Laboratory, College of Chemistry, University of California, Berkeley, Berkeley, CA 94720. Ultraviolet-visible spectra were measured with a Cary Model 300 Scan spectrophotometer. All ^1H NMR and ^{13}C NMR spectra were recorded at room temperature in deuterated solvents on an AMX-400 Bruker FT spectrometer unless otherwise noted. Mass spectrometry experiments were performed by the QB3/Chemistry Mass Spectrometry Facility in B207 Stanley Hall, UC Berkeley. Gentisic acid (GA), or 2,5-dihydroxybenzoic acid (2,5-DHB), was obtained from TCI America (min. 98% purity). Iron chloride stock solutions in 1 M HCl were standardized by EDTA titration. Tris(hydroxymethyl)aminomethane (Tris) buffered saline solutions were made according to the *Preparation of Reagents and Buffers used in Molecular Cloning*, except the pH was adjusted to 7.2.

Speciation diagrams. Speciation distribution diagrams were generated with HySS (Hyperquad Simulation and Speciation) software (23) using ligand protonation constants

and iron-ligand formation constants found in the literature (for ligands GA, SA, 2,3-DHBA) (21, 22) Iron hydrolysis constants were also taken into account, and were obtained from the supplementary help files in Hyperquad and HySS. The concentration of ligands and iron used to generate the diagrams were those identical to conditions used in the fluorescence quenching assays ($[L] = 6 \text{ mM}$, $[\text{Fe}] = 2 \text{ mM}$).

Dissociation Constant Data Refinement for Fe:GA, Fe:SA, Fe:2,3DHBA systems

Hyperquad 2003 was used to fit fluorescence quenching data and to refine dissociation constants for each of the Scn:Fe-L interactions. ligand protonation constants and iron-ligand formation constants found in the literature (for ligands GA, SA, 2,3-DHBA). Iron hydrolysis constants were also taken into account, and were obtained from the supplementary help files in Hyperquad and HySS. The concentration of ligands and iron used to generate the diagrams were those identical to conditions used in the fluorescence quenching assays ($[L] = 6 \text{ mM}$, $[\text{Fe}] = 2 \text{ mM}$, $\text{pH} = 7.4$). Fits with excessive error were considered unreliable. Maximum number of iterations was set to 100. A different binding model input was used for each bidentate ligand, since each bidentate ligand complexes iron differently under physiological conditions. The main Fe-L species (as obtained from HYSS) was used as the active binding compound to Scn. The following explicit models were used:

For $L = 2,3\text{-DHBA}$

$\text{Scn} + 2,3\text{-DHBA} \rightleftharpoons \text{Scn:2,3-DHBA}$

For $L = \text{SA}$

$\text{Scn} + \text{Fe}(\text{SA}) \rightleftharpoons \text{Scn:Fe}(\text{SA})$

$\text{Scn:Fe}(\text{SA}) + \text{SA} \rightleftharpoons \text{Scn:Fe}(\text{SA})_2$

For $L = \text{GA}$

$\text{Scn} + \text{Fe}(\text{GA}) \rightleftharpoons \text{Scn:Fe}(\text{GA})$

UV-vis solutions of $\text{Fe}(\text{GA})_x$ and $\text{Scn:Fe}(\text{GA})_x$ Using a standardized solution of FeCl_3 (27.1 mM, 1 equiv = 3.7 μL), one, two, and three equivalents of GA were added (1 equiv = 8.33 μL of 12 mM GA) and spectra were recorded for each sample ($\lambda_{\text{max}} = 319 \text{ nm}$). All solutions were made in TBS buffer at pH range 7.2-7.4. UV-vis spectra of Scn:FeCl₃:GA with FeCl₃:GA in varying ratios: A solution of 1 mL 100 nM Scn and 0.300 mL of 100 μM Fe(GA) was equilibrated for 1 hour, and a UV-vis spectrum was recorded ($\lambda_{\text{max}} = 319 \text{ nm}$). One equivalent (8.33 μM of 12 mM solution) GA was added to the solution of Scn:Fe:GA to make Scn:Fe:GA₂ and a spectrum was recorded ($\lambda_{\text{max}} = 319 \text{ nm}$). Another one equivalent addition was added to form Scn:Fe:GA₃ and a spectrum was recorded ($\lambda_{\text{max}} = 319 \text{ nm}$). All solutions were made in TBS buffer at pH range 7.2-7.4.

Ligand solutions preparation. All metal complex solutions were used immediately after preparation. An aliquot of a DMSO stock solution of the free ligand (12 mM, 25 μL) and FeCl_3 salt (27 mM, 3.7 μL , 0.33 equiv) were combined, vigorously shaken, and diluted with TBS buffer (pH 7.2) to form the metal complexes at a concentration of 0.1 mM. The solutions were equilibrated for 1.5 hr and diluted to a final concentration of 20 μM in 5% DMSO/TBS buffer. Apo ligand solutions were prepared analogously without the addition of the metal salt.

Fluorescence Quenching Binding Assay. Fluorescence quenching of human Siderocalin (Scn) was measured on a Cary Eclipse fluorescence spectrophotometer with a 20 nm slit band pass for excitation and a 2.5 nm slit band pass for emission using the characteristic excitation and emission wavelengths $\lambda_{\text{exc}} = 281$ nm and $\lambda_{\text{em}} = 340$ nm, respectively. Excitation and emission cut-off filters were both set to automatic. The PMT detector voltage was manually selected to be 1000 volts. The intrinsic fluorescence in Scn is generally attributed to two tryptophan residues, W31 and W79, found in the proximity of the Scn binding site. Measurements were made at a protein concentration of 100 nM in buffered aqueous solution (pH 7.2), 5% DMSO, plus 32 $\mu\text{g/mL}$ ubiquitin. Fluorescence intensities were corrected for dilution due to addition of ligand. Fluorescence data were analyzed by a nonlinear regression analysis of the normalized fluorescence response versus ligand concentration using Hyperquad, which allows for a multiwavelength treatment of the data and simultaneously refines all titrations. The model for determination of the species stoichiometry and dissociation constants (K_d) takes into account ferric ion hydrolysis constants, 2,5-DHB protonation constants and Fe-2,5-DHB formation constants. Dissociation constants were determined from at least three independent titrations.

Synthesis

2,5-Bis-benzyloxy-benzoic acid benzyl ester (2). Gentisic acid, or 2,5-dihydroxybenzoic acid (**1**) (64.8 mmol) was dissolved in 500 mL acetone. Under Finkelstein reaction conditions, 3 equivalents of KI (195 mmol) and 7 equivalents of K_2CO_3 (454 mmol) were added to the reaction mixture. The reaction mixture was clear yellow with white, insoluble salts. Upon addition of benzyl chloride (195 mmol), the solution turned clear brown. The reaction mixture was refluxed in a mineral oil bath under a nitrogen atmosphere. After 72 hours, the reaction was cooled to room temperature and the salts were filtered off. The filtrate was evaporated to be a white solid, after which it was redissolved in 200 mL methylene chloride and washed (2x with 150 mL) deionized water. The clear yellow solution was concentrated and loaded onto a silica column that was packed in 100% hexanes. The product was eluted with 100% methylene chloride. The fractions containing the product were collected and evaporated. The product was a white solid that was obtained in 87% yield. ^1H NMR (500 MHz, CDCl_3): δ 7.53 (s, 1H, ArH), 7.46 (m, 10H, ArH), 7.10 (d, 1H, ArH, $J = 10$ Hz), 6.98 (d, 1H, ArH, $J = 10$ Hz), 5.25 (s, 2H, PhCH_2) 5.06 (s, 2H, PhCH_2). ^{13}C NMR (75 MHz, CDCl_3): δ 166.04, 152.73, 152.54, 136.92, 136.77, 136.03, 128.65, 128.56, 128.53, 128.28, 128.13, 128.10, 127.82, 127.60, 127.26, 127.26, 121.49, 120.40, 117.49, 116.03, 71.75, 70.73, 66.88. Elemental analysis: % C, H: estimated 79.22, 5.70, found 79.21, 5.73.

2,5-Bis-benzyloxy-benzoic acid (3). To a 500 mL roundbottom flask, **2** (56.2 mmol) was dissolved in 275 mL of methylene chloride. The solution was clear and colorless. A methanolic solution of KOH (1M, 100 mL MeOH) was added via addition funnel over the course of 20 minutes over air. Upon addition, the solution began to turn clear and yellow. The reaction stirred overnight and was monitored by TLC. KOH pellets were added to drive the reaction to completion as monitored by disappearance of the starting

material spot in TLC. The solvent was evaporated, and the resulting mixture (light orange slurry) was dissolved in 200 mL deionized water. The reaction flask was cooled in an ice-water bath, and concentrated HCl (12M) was added slowly and dropwise to the stirring reaction mixture (clear, colorless solution) over air until the solution turned opaque and white. The white solid was filtered and dried *in vacuo* for 10 hours (97% yield). ¹H NMR (500 MHz, CDCl₃): δ 7.84 (d, 1H, ArH, J = 5 Hz), 7.37 (m, 15H, ArH), 7.10 (dd, 1H, ArH, J = 5 Hz, J = 10 Hz), 7.00 (d, 1H, ArH, J = 10 Hz), 5.39 (s, 2H, PhCH₂), 5.14 (s, 2H, PhCH₂), 5.07 (s, 2H, PhCH₂). ¹³C NMR (75 MHz, CDCl₃): δ 165.22, 153.75, 151.63, 136.55, 129.25, 129.19, 128.68, 128.21, 128.03, 127.63, 122.86, 117.58, 114.88, 72.98, 70.69. (+)FABMS: m/z calc. 355, obs. 355 (MH⁺).

(2,5-Bis-benzyloxy-phenyl)-(2-thioxo-thiazolidin-3-yl)-methanone (4). The white solid **3** (55.3 mmol) was dried *in vacuo* until powdery, then was dissolved in 175 mL benzene to give a clear, colorless solution. *N,N'*-dicyclohexylcarbodiimide (DCC) (60.9 mmol) was added to the solution, resulting in a translucent yellow solution. The addition of 2-mercaptothiazoline (55.3 mmol) over air and a catalytic amount of dimethylaminopyridine (0.17 mmol) resulted in an opaque, bold yellow solution. The reaction was stirred under a nitrogen atmosphere overnight, after which the excess DCC was filtered. The benzene was evaporated by rotary evaporation and the reaction mixture was a clear, orange oil that was soluble in methylene chloride. Recrystallization with minimal methylene chloride and isopropyl alcohol was unsuccessful, so the mixture was loaded onto a silica column packed with 70:30 hexanes:methylene chloride. The product was eluted to 100% methylene chloride (R_f = 0.731 in 100% methylene chloride). The product was a sticky yellow solid that was difficult to work with. Recrystallization with minimal ethyl acetate and hexanes was unsuccessful, so the product was used as a solution in methylene chloride in further synthetic steps. ¹H NMR (400 MHz, CDCl₃): δ 7.44 (m, 10H, ArH), 7.10 (m, 2H, ArH), 6.88 (d, 1H, ArH, J = 10 Hz), 5.09 (s, 1H, PhCH₂), 4.98 (s, 2H, PhCH₂), 4.48 (t, 2H, RNCH₂, J = 10 Hz), 2.90 (t, 2H, RNCH₂, J = 5 Hz). (+)FABMS: m/z calc. 436, obs. 436 (MH⁺). Elemental analysis: % C, H, N: estimated 66.18, 4.86, 3.22, found 66.34, 5.06, 3.52.

TRENGEN-Bn₆ (5). A 200 mL (18.08 g, 41.5 mmol) solution of **4** in methylene chloride (clear, yellow) was added to a 5 mL solution of triethylamine (2.07 mL, 13.8 mmol) dissolved in methylene chloride under a nitrogen atmosphere over the course of 5 minutes. The reaction was stirred overnight. A mixture of *mono*-, *bis*- and *tris*-substituted TREN compounds were obtained (In 4% MeOH: 96% methylene chloride TLC solution (R_f *mono*-TREN = 0.27, R_f *bis*- = 0.38, R_f *tris*- = 0.54; *tris*-substituted compound is visible by long-wavelength UV light). A silica column was packed in 100% methylene chloride and the product was loaded and eluted to 4% methanol to elute the *tris*- and *bis*-substituted compounds. The *mono*-substituted compound was eluted with 10% methanol and 1% triethylamine. The collected fractions were washed with 0.5M NaOH (4x50 mL) to eliminate any residual 2-mercaptothiazoline by-product. Fractions containing the *tris*-substituted compound were collected and concentrated *via* rotary evaporation. ¹H NMR (500 MHz, CDCl₃): δ 7.98 (m, 3H, ArCONH), 7.85 (d, 3H, ArH, J = 3 Hz), 7.34 (m, 30H, ArH), 6.96 (dd, 3H, ArH, J₁ = 3.5 Hz, J₂ = 5.5), 6.69 (d, 3H, ArH, J = 9 Hz), 5.11 (s,

6H, PhCH₂), 4.87 (s, 6H, PhCH₂), 3.25 (m, 6H, R₂NCH₂CH₂NHCOAr), 2.30 (m, 6H, R₂NCH₂CH₂NHCOAr). ¹³C NMR (75 MHz, CDCl₃): δ 164.81, 153.01, 151.10, 137.01, 135.91, 128.81, 128.62, 128.03, 127.92, 127.63, 122.72, 119.93, 116.59, 114.65, 71.86, 70.50, 53.48, 51.91, 36.98.

TRENGEN (6). TRENGEN-Bn₆, was placed in an EDTA-soaked and EDTA-washed Schlenk flask. The flask was immersed in an ice-water bath and a 25 mL acid solution of 50:50 acetic acid:HCl was added dropwise. The reaction mixture was stirred for 48 hours, or until the reaction was completed as assayed by thin layer chromatography. After the deprotection was completed, the acid was evaporated and subsequently coevaporated with methanol washes (5x 10 mL MeOH) in vacuo until an off-white powder was obtained. R_f = 0.20 in 96:4 CH₂Cl₂:MeOH TLC solvent system. ¹H NMR (500 MHz, CD₃OD): δ 3.66 (t, 6H, NCH₂CH₂NCO, J₁ = 42 Hz, J₂ = 11 Hz), 3.87 (t, 6H, NCH₂CH₂NCO, J₁ = 11 Hz, J₂ = 42 Hz), 6.76 (d, 3H, ArH, J = 8.2 Hz), 6.87 (d, 3H, ArH, J = 2.5 Hz), 7.21 (s, 3H, ArH). ESI (+) 555.21 m/z (M+H). IR (ZnSe crystal, neat): ν 1488, 1557, 1646, 2360, 3277 cm⁻¹. Anal. Calcd for TRENGEN •3H₂O : C, 66.51%; H, 6.57%; N, 6.08%. Found: C, 66.92%; H, 6.20%; N, 6.08%.

Fe-TRENGEN. TRENGEN (93 mg, 0.168 mmol) was dissolved in 4.5 mL MeOH, forming a clear, yellow solution. Pyridine (0.15 mL) was added, forming a clear red-brown solution upon addition. Addition of ferric chloride hexahydrate (0.045 g, 0.168 mmol) afforded a dark opaque purple solution. The reaction was stirred for 30 minutes, and various crystallizations were set up using methanol with pentane as the diffusing solvent. ESI (+) 608.12 m/z (M+H). IR (ZnSe crystal, neat): ν 1023.7, 1534, 1593, 2831, 2945, 3326 cm⁻¹.

References

1. Goetz DH et al. (2002) The Neutrophil Lipocalin NGAL Is a Bacteriostatic Agent that Interferes with Siderophore-Mediated Iron Acquisition. *Mol Cell* 10:1033–1043.
2. Abergel RJ et al. (2006) Anthrax pathogen evades the mammalian immune system through stealth siderophore production. *Proc Natl Acad Sci* 103:18499–18503.
3. Sia AK, Allred BE, Raymond KN Siderocalins: Siderophore binding proteins evolved for primary pathogen host defense. *Curr Opin Chem Biol*. Available at: <http://www.sciencedirect.com/science/article/pii/S1367593112001482> [Accessed March 29, 2013].
4. Flo TH et al. (2004) Lipocalin 2 mediates an innate immune response to bacterial infection by sequestering iron. *Nature* 432:917–921.
5. Hoette TM, Abergel RJ, Xu J, Strong RK, Raymond KN (2008) The Role of Electrostatics in Siderophore Recognition by the Immunoprotein Siderocalin¹. *J Am Chem Soc* 130:17584–17592.
6. Mishra J et al. (2004) Amelioration of Ischemic Acute Renal Injury by Neutrophil Gelatinase-Associated Lipocalin. *J Am Soc Nephrol* 15:3073–3082.
7. Mallbris L et al. (2002) Neutrophil gelatinase-associated lipocalin is a marker for dysregulated keratinocyte differentiation in human skin. *Exp Dermatol* 11:584–591.
8. Cho H, Kim J-H (2009) Lipocalin2 Expressions Correlate Significantly With Tumor Differentiation in Epithelial Ovarian Cancer. *J Histochem Cytochem* 57:513–521.
9. Chakraborty S, Kaur S, Guha S, Batra SK (2012) The multifaceted roles of neutrophil gelatinase associated lipocalin (NGAL) in inflammation and cancer. *Biochim Biophys Acta Bba - Rev Cancer* 1826:129–169.
10. Troadec M-B, Ward DM, Kaplan J (2009) A Tf-independent iron transport system required for organogenesis. *Dev Cell* 16:3–4.
11. Li JY et al. (2009) Scara5 is a ferritin receptor mediating non-transferrin iron delivery. *Dev Cell* 16:35–46.
12. Bao G et al. (2010) Iron traffics in circulation bound to a siderocalin (Ngal)–catechol complex. *Nat Chem Biol* 6:602–609.
13. Devireddy LR, Hart DO, Goetz DH, Green MR (2010) A Mammalian Siderophore Synthesized by an Enzyme with a Bacterial Homolog Involved in Enterobactin Production. *Cell* 141:1006–1017.

14. Correnti C et al. (2012) Siderocalin/Lcn2/NGAL/24p3 Does Not Drive Apoptosis Through Gentisic Acid Mediated Iron Withdrawal in Hematopoietic Cell Lines. *Plos One* 7:e43696.
15. Abergel RJ, Moore EG, Strong RK, Raymond KN (2006) Microbial Evasion of the Immune System: Structural Modifications of Enterobactin Impair Siderocalin Recognition¹. *J Am Chem Soc* 128:10998–10999.
16. Abergel RJ et al. (2008) The Siderocalin/Enterobactin Interaction: A Link between Mammalian Immunity and Bacterial Iron Transport¹. *J Am Chem Soc* 130:11524–11534.
17. Abergel RJ, Zawadzka AM, Hoette TM, Raymond KN (2009) Enzymatic Hydrolysis of Trilactone Siderophores: Where Chiral Recognition Occurs in Enterobactin and Bacillibactin Iron Transport. *J Am Chem Soc* 131:12682–12692.
18. Lee CW, Ecker DJ, Raymond KN (1985) Coordination chemistry of microbial iron transport compounds. 34. The pH-dependent reduction of ferric enterobactin probed by electrochemical methods and its implications for microbial iron transport. *J Am Chem Soc* 107:6920–6923.
19. Cass ME, Garrett TM, Raymond KN (1989) The salicylate mode of bonding in protonated ferric enterobactin analogs. *J Am Chem Soc* 111:1677–1682.
20. Cohen SM, Meyer M, Raymond KN (1998) Enterobactin Protonation and Iron Release: Hexadentate Tris-Salicylate Ligands as Models for Triprotonated Ferric Enterobactin¹. *J Am Chem Soc* 120:6277–6286.
21. Martell, A.E., Smith, A.R. (1977) *Critical Stability Constants* (Plenum, New York and London).
22. Khanolkar, V.D., Jahagirdar, D.V., Khanolkar, D.D. (1973) Studies in Fe(III)-5-hydroxysalicylic Acid System. *Indian J Chem* 11:286–287.
23. Alderighi L. et al. (1999) Hyperquad simulation and speciation (HySS): a utility program for the investigation of equilibria involving soluble and partially soluble species. *Coord Chem Rev* 184:311–318.
24. Gans, Peter, Sabatini, Antonio, Vacca, Alberto (1996) Investigation of equilibria in solution. Determination of equilibrium constants with the HYPERQUAD suite of programs. *Talanta* 43:1739–1753.